

Chirped pulse microwave and single-shot terahertz spectroscopy studies of intermolecular interactions

Thesis by
Griffin John Mead

In Partial Fulfillment of the Requirements for the
degree of
Doctor of Philosophy

CALIFORNIA INSTITUTE OF TECHNOLOGY
Pasadena, California

2021
Defended Nov. 30, 2020

© 2021

Griffin John Mead
ORCID: 0000-0003-0067-4219

All rights reserved

ACKNOWLEDGEMENTS

Progress through graduate school requires a supportive group of colleagues, friends, and family. They create the environment and context which brighten the summits and cushion the valleys. To this end, there are many people whose contributions bear acknowledgement.

First, I would like to thank my research advisor, Geoff Blake. Geoff embodies the refrain that the smartest individuals are often also the kindest. I have learned a tremendous amount under his guidance. He has provided the freedom to explore the potentials of our experimental techniques, and a sympathetic and encouraging ear during difficulties. I will miss the lively impromptu office conversations, which ranged from spectroscopy to the geographical peculiarities of Ojai vineyards and back again in just minutes.

Second, the other members of my thesis committee, Professors Tom Miller, Nate Lewis, and Scott Cushing, deserve many thanks. Their helpful critiques and suggestions have contributed greatly to my ability to articulate and defend ideas.

Caltech transportation has also played an integral role during my graduate research. With the flooding of the Linde-Robinson laboratory in 2018, Transportation was instrumental in the moving our lab into the South Mudd building. Thanks to their efforts, the new lab space is a spacious and functional environment for research.

No graduate student exists without the efforts of excellent under-graduate mentors. Professor Andrew Udit introduced me to the realm of scientific research, and it is as a result of his support that I have kept pursuing research as a passion and a career. Professors Michael Hill, Aram Nersissian, and Don Deardorff, along with the rest of the Occidental College Chemistry Department, also deserve great thanks for their teaching and help over the years.

I need to thank my colleagues and friends at Caltech. Ian Finneran, Jacob Good, Brandon Carroll, and Brett McGuire were the elder experimental graduate students when I joined the Blake group. They were unfailingly helpful to me as I learned the basics of spectroscopy. I also enjoyed the moments when I got to chat with the astronomers: Danielle Piskorz, Dana Anderson, and Masha Kleshcheva.

As they graduated, I got to work with and know new faces: Kyle Virgil, Olivia Wilkins, Cam Buzard, Alex Froebel, Haw-Wei Lin, Sadie Dutton, and Maria Camarca. They have each contributed immensely to the fun and excitement of working

in a lab, and I am daily impressed by their drive, intelligence, and determination. Haw-Wei has been instrumental in developing the multi-dimensional single-shot spectroscopy in this thesis. Kyle somehow found time to build an entire lab with me while also tackling ambitious and exciting work on photovoltaic materials. Alex and Sadie were similarly critical to building the lab and are making great strides with their work on gas phase clusters. Olivia, Cam, and Maria are all busy disentangling the origins of molecules throughout the universe. I look forward to seeing all that these talented scientists will accomplish in the coming years.

Ioan Bogdan Magdău has been a wonderful collaborator over the past few years. His understanding of the physical world is shaped by a deep knowledge of it's fundamental theoretical underpinnings. Our conversations trying to reconcile the languages of theory and experiment have been illuminating.

I have been fortunate to work with several groups outside of the United States. Professors Ikufumi Katayama and Jun Takeda were critical for helping us develop our nonlinear single-shot spectrometer. I enjoyed learning nuances of microwave spectroscopy from Professor Walther Caminati's group, and working with Elena Alonso on the n-propanol-water dimer. I am also deeply appreciative of the hospitality and resources that Professors Osman Bakr and Omar Mohammed provided during a month-long visit to KAUST.

Time spent with Scott Cushing's research group — Bryce Hickam, Isabel Klein, Jonathan Michelsen, Danika Nimlos, Manni He, Hanzhe Liu, and Szilard Szoke — has been time well spent. I have rarely laughed harder during graduate school than in our conversations. I appreciate our outings through California, from bizarrely steep hikes up Mount Baldy to long days spent in the desert.

Adventures with Sebastian Lee and Bradley Gorsline have also been formative. I began graduate school woefully un-educated in the joys of hiking and climbing. I have learned a great deal thanks to Brad's tutelage, and deeply enjoyed our trips to Nevada and throughout California. The many trips into the mountains with Sebastian, hiking in the dark at a far too early hour or running along fire roads, are some of my fondest memories from graduate school.

I have been very fortunate to know Michael Patton and Peter Beer. Mike's friendliness, deep dedication to research, and moral clarity were apparent to me the first day we met in college. During his work across the country and around the world, he has never failed to share his infectious enthusiasm for science with me. Pete is

cut from the same cloth. Our dinner table conversations on government, religion, and obscure trails tucked deep in the San Gabriels have been refreshing.

Other friends reach even further back in time. Kyle Abbott, Philip Schaeffer, and Jarratt Pott have been part of my life for many, many years. There is too much to say here, so to keep it simple: thank you.

My parents, Betsi and Paul, have always exceeded what could be hoped for from any parent. Their undivided love, kindness, and support are the only reason I am able to write these words. I want to thank them for their encouragement, freedom to explore, and for instilling a love of science and debate in me from a very young age.

My siblings, Patrick and Emma, are indispensable. They grasp the world in ways I cannot, and I deeply appreciate every moment I have gotten to spend with them. I know they are growing up to be hard-working, smart, and generous individuals, and I look forward to all the years we will get to spend together.

Finally, I want to thank Kristina Geiger for her unending support and love over the past seven years. Kristi, you have always been the one to whom I can turn. I am deeply looking forward to our future.

ABSTRACT

While the glow of a sodium vapor lamp or the crisp reds in autumn leaves are eye-catching examples of transitions between atomic and molecular energy levels ($h\nu \sim 2\text{-}3\text{ eV}$), it is arguably the much lower energy, thermally populated intermolecular “bath” states ($h\nu \sim 10^{-5}\text{-}10^{-2}\text{ eV}$) that contribute most directly to the physical properties of matter. Although invisible to the human eye, in this thesis we study fundamentals of these low-energy interactions with two complementary techniques: chirped pulse microwave spectroscopy and nonlinear single-shot terahertz (THz) Kerr effect spectroscopy.

In the first section, we apply chirped pulse-Fourier transform microwave (CP-FTMW) spectroscopy from 8-16 GHz to study fundamental hydrogen bonding motifs in gas phase alcohol water dimers. Hydrogen bonding is ubiquitous in nature and directly contributes to a range of phenomena from phase transitions in water to solvation of ions to enzymatic activity. Our focus on gas phase dimers reduces the spectral ambiguity arising in condensed phase samples, where inhomogeneous and homogeneous broadening can hamper observation of conserved intermolecular interaction motifs. The hydrogen bonding conformation of two alcohol-water dimers, n-propanol-water and isopropanol-water, were characterized. Both were found to adopt a shared water donor-alcohol acceptor conformation.

The following sections use nonlinear THz spectroscopy from 0.1-10 THz to investigate molecular dynamics in the condensed phase. We focus on halogenated methane liquids, whose intense intramolecular vibrational modes are commensurate in energy to the intermolecular bath states. One central goal of this section was developing a technique to more rapidly collect nonlinear, multi-dimensional data from liquid systems. To that end, we developed a single-shot measurement approach using a reflective nickel echelon mirror and a high frame rate camera. With this new device we achieved an order of magnitude reduction in experimental integration times. High resolution, nonlinear multi-dimensional THz studies of several halogenated methane liquids and materials were produced as a result. From these data, we identified important spectral contributions from the experimental instrument response function.

PUBLISHED CONTENT AND CONTRIBUTIONS

1. L. Evangelisti *et al.*, Conformational equilibrium and internal dynamics in the iso-propanol–water dimer. en, *Phys. Chem. Chem. Phys.* **19**, 568–573, DOI 10.1039/C6CP06315B (2017),
G.J.M. re-built the experimental apparatus, collected and analyzed data, and helped prepare the manuscript.
2. G. J. Mead, E. R. Alonso, I. A. Finneran, P. B. Carroll, G. A. Blake, Identification of two conformationally trapped n -propanol-water dimers in a supersonic expansion. en, *Journal of Molecular Spectroscopy* **335**, 68–73, DOI 10.1016/j.jms.2017.03.008 (May 2017),
G.J.M. collected and analyzed data, performed ab initio calculations, and wrote the manuscript.
3. G. J. Mead, I. Katayama, J. Takeda, G. A. Blake, An echelon-based single shot optical and terahertz Kerr effect spectrometer. *Review of Scientific Instruments* **90**, 053107, DOI 10.1063/1.5088377 (May 2019),
G.J.M. designed and constructed the experimental apparatus, collected and analyzed data, and wrote the manuscript.
4. I. B. Magdău, G. J. Mead, G. A. Blake, T. F. Miller, Interpretation of the THz-THz-Raman Spectrum of Bromoform. en, *J. Phys. Chem. A* **123**, 7278–7287, DOI 10.1021/acs.jpca.9b05165 (Aug. 2019),
G.J.M. assisted with methodology and data analysis, and helped write the manuscript.
5. G. J. Mead, H.-W. Lin, I.-B. Magdau, T. F. Miller, G. A. Blake, Sum-Frequency Signals in 2D-Terahertz-Terahertz-Raman Spectroscopy. en, *J. Phys. Chem. B*, acs.jp cb.0c07935, DOI 10.1021/acs.jp cb.0c07935 (Sept. 2020),
G.J.M. helped design and construct the experimental apparatus, collected and analyzed data, and wrote the manuscript.

TABLE OF CONTENTS

Acknowledgements	iii
Abstract	vi
Published Content and Contributions	vii
Table of Contents	vii
List of Illustrations	x
List of Tables	xii

I Introduction 1

Chapter I: Introduction	2
1.1 Microwave spectroscopy of gas phase molecular dimers	3
1.2 Nonlinear terahertz spectroscopy of liquids	4

II Microwave Spectroscopy 14

Chapter II: Conformational equilibrium and internal dynamics in the iso- propanol–water dimer	15
2.1 Introduction	16
2.2 Experimental approach	17
2.3 Ab initio calculations	18
2.4 Results: GAI (Inner) conformer	20
2.5 Results: GAO (Outer) isomer	24
2.6 Results: Conformational equilibrium	26
2.7 Conclusion	27
Chapter III: Identification of two conformationally trapped n-propanol-water dimers in a supersonic expansion	32
3.1 Introduction	33
3.2 Experimental approach	34
3.3 Ab initio calculations	34
3.4 Results: Ab initio structures	35
3.5 Results: Observation of <i>Gg'-wl</i> and <i>Tg-wl</i> conformers	37
3.6 Conclusion	42

III Terahertz Spectroscopy 45

Chapter IV: Fundamentals of nonlinear terahertz Kerr effect spectroscopy . . .	46
4.1 Theory	46
4.2 Experimental technique	51
4.3 Data analysis	58

4.4 The sample cuvette	58
Chapter V: Fundamentals of single-shot spectroscopy	62
5.1 Overview	62
5.2 Probe transport pathway	64
5.3 Echelon imaging pathway	65
5.4 Echelon constraints	68
5.5 Data acquisition	71
5.6 Single-shot data processing	72
5.7 Diagnostic imaging using the Andor camera	75
Chapter VI: An echelon-based single-shot optical and terahertz Kerr effect spectrometer	80
6.1 Introduction	81
6.2 Experimental approach	82
6.3 Results: Kerr effect measurements	85
6.4 Results: Sensitivity and noise performance	89
6.5 Results: Stage-scan vs. echelon 1D-OKE responses	91
6.6 Results: Heterodyne and homodyne components of the Kerr effect signal	91
6.7 Conclusions	95
Chapter VII: Sum-frequency signals in 2D-terahertz-terahertz-Raman spec- troscopy of halogenated methane liquids	99
7.1 Introduction	100
7.2 Experimental approach	101
7.3 Results: Instrument response function modelling	106
7.4 Results: Sum-frequency reduced density matrix modeling	107
7.5 Conclusion	109
Chapter VIII: Gas-phase nonlinear terahertz phenomena	114
8.1 Terahertz excitation of coherent rotational wavepackets in N ₂	114
8.2 Water vapor emission as a secondary source of intense THz radiation	116
Chapter IX: 2D-TTR spectroscopy of materials	122
9.1 Diamond	122
9.2 Gallium phosphide	124
9.3 Lithium niobate	125
IV Conclusion and Future Directions	141
Chapter X: Conclusions and future directions	142
10.1 2D-TTR spectroscopy of water and aqueous solutions	142
10.2 Time-resolved dynamics in hybrid perovskites	144
10.3 Single-shot applications to coherent control experiments	145
Chapter A: Python data processing script for 1D Kerr effect data	148
Appendix B: 2D-TTR bromoform data under two OPA conditions	150

LIST OF ILLUSTRATIONS

<i>Number</i>	<i>Page</i>
1.1 Spectral regions studied in this thesis	3
1.2 2D-TTR pulse sequence	5
1.3 Strategies for performing multi-dimensional THz spectroscopy	6
1.4 2D-TTR instrument response function	9
2.1 Chirped pulse-Fourier transform microwave spectrometer circuit	18
2.2 Calculated isopropanol-water dimer structures	19
2.3 Transition splittings from tunneling	21
2.4 Atom labels for the isopropanol-water conformer structures	23
3.1 Calculated dipole and rotational constants for ten n-propanol-water dimer structures	35
3.2 Rotational spectra of n-propanol-water dimers.	38
3.3 Kraitchman substitutions of the n-propanol-water dimers	39
4.1 1D-TKE pulse sequence	48
4.2 2D-TTR pulse sequence	49
4.3 1D-TKE polarization selectivity	50
4.4 2D-TTR polarization selectivity	51
4.5 Diagram of the single shot Kerr effect experimental apparatus	53
4.6 Ray transfer calculations of THz pump beam pathway	55
4.7 2D-TTR response of carbon disulfide	57
4.8 1D-TKE response of the silicon nitride cuvette window	59
5.1 Three approaches to single-shot encoding	63
5.2 Reflective nickel echelon mirror	63
5.3 Probe ray transfer pathway	65
5.4 Echelon image formation	66
5.5 Image of echelon surface	67
5.6 Correspondence between the experimental MTF and IRF	67
5.7 MTF of single-shot system	68
5.8 Echelon angular separation model	70
5.9 Bromoform z scan vignetting	71
5.10 Single-shot experimental phase information	73
5.11 Phase processing steps in 2D-TTR experiment	75

5.12	THz focal region imaging	76
5.13	30 ps and 6 ps echelon probe focal spots	78
5.14	Imaging the pump-probe focal spot overlap	78
6.1	1D-OKE response of DMSO and quartz	86
6.2	1D-OKE and 1D-TKE of CS ₂	88
6.3	1D-OKE of bromoform	89
6.4	Signal-to-noise performance of the single-shot spectrometer	92
6.5	Comparison of single-shot and stage scan 1D-OKE data	93
6.6	Heterodyne and homodyne components of the single-shot signal	94
7.1	1D-TKE spectra of CHBr ₃ and CHCl ₃	102
7.2	Res-TKE, SF-TKE, and SF-OKE ladder diagrams	103
7.3	2D-TTR time domain responses of CHBr ₃ and CHCl ₃	104
7.4	2D-TTR frequency domain responses of CHBr ₃ and CHCl ₃	108
7.5	Comparison between 2D-TTR data and IRF/SF-RDM models	109
7.6	Comparison between experimental and IRF/SF-RDM model THz pulse shapes	110
8.1	TKE response of N ₂	115
8.2	2D-TTR response of CS ₂	117
8.3	Water vapor oscillations around $t_1 = 0$	118
8.4	Water vapor oscillations at large t_1 times	118
9.1	2D-TTR response of diamond	123
9.2	2D-TTR experimental response of gallium phosphide	126
9.3	Comparison of 1D-TKE and 2D-TTR t_2 signals in lithium niobate	127
9.4	Model of sum-frequency THz excitation of <i>E</i> -symmetry TO phonon mode in LiNbO ₃	128
9.5	THz-THz lithium niobate IRF model	129
9.6	Phonon-THz lithium niobate IRF model	130
9.7	Polarizability and dipole anharmonicity models of the LiNbO ₃ phonon mode 2D-TTR spectrum	131
9.8	Optical rectification model of LiNbO ₃ 2D-TTR response	136
9.9	Optical rectification model responses along t_1, t_2	136
10.1	The 1D-TKE response of neat water	143
B.1	2D-TTR time domain responses of CHBr ₃ under different OPA conditions	151
B.2	2D-TTR frequency domain responses of CHBr ₃ under different OPA conditions	152

LIST OF TABLES

<i>Number</i>	<i>Page</i>
2.1 Ab initio rotational constants and dipole moments of five isopropanol-water dimers	20
2.2 Experimental spectroscopic constants of IP-W-GAI	21
2.3 Experimental spectroscopic constants of IP-W-GAO isotopologues . .	25
2.4 Experimental and ab initio spectroscopic constants of IP-W-GAI . . .	26
2.5 Hydrogen bond lengths in IP-W GAO conformer	26
3.1 Ab initio parameters of the ten n-propanol-water dimer conformers .	36
3.2 Fitted parameters of the two detected n-propanol-water dimers	40
3.3 MP2/aug-cc-pVTZ principle axis coordinates	41
3.4 Ab initio hydrogen bond distances and angles for n-propanol-water dimers	41
6.1 Liquids with varying $\chi^{(3)}$ magnitudes screened with 1D Kerr effect spectrometer	90
9.1 C_{3v} character table	132
9.2 C_{3v} direct product table	132
9.3 $\chi^{(2)}$ parameters of DAST, GaP, and LiNbO ₃	137

Part I

Introduction

Chapter 1

INTRODUCTION

Intermolecular interactions within solids, liquids, and gases are critical for understanding much of biology, chemistry, and physics. Intrinsic energies of these interactions range from $0.1\text{-}300\text{ cm}^{-1}$ ($h\nu \sim 10^{-5}\text{-}10^{-2}\text{ eV}$), which leads to a complex set of thermally populated bath states at room temperature ($k_B T \sim 203\text{ cm}^{-1}$). Small perturbations to these states can have profound effects. Consider, for example, how the dynamics of water molecules change as a sample is cooled from room temperature to 0 degrees Celsius. With this slight decrease in thermal energy ($\Delta E = 24\text{ cm}^{-1}$), changes in hydrogen bonding interactions between adjacent molecules lead to an abrupt phase transition that transforms liquid water into a lower density solid. The substantial consequences of small changes in intermolecular interactions, as exemplified by water, has driven investments in theoretical and experimental studies of condensed phase phenomena.

Water, perhaps predictably given its importance in the natural world, remains a favorite subject of study; tens of water models have been developed [1, 2, 3, 4], and new computational efforts appear frequently in the literature [5, 6, 7]. Experimental efforts have similarly ballooned over time, ranging from studies of fundamental interactions in neat water [8, 9, 10, 11, 12, 13], to dynamics in aqueous solutions [14], to the solvation of bio-molecules [15, 16], and even to probing the mechanism underlying anti-freeze proteins which preserve psychrophiles in arctic temperatures [17, 18].

While a wide range of spectroscopic techniques can be used to observe intermolecular interactions, all must contend with a characteristic lack of clear, bright chromophores. Furthermore, signals associated with many body dynamics are inherently amorphous due to homogeneous and in-homogeneous broadening and the large density of states within the system. These factors can create ambiguity and uncertainty in interpreting data.

In this thesis, we resolve some of these challenges by studying intermolecular interactions and dynamics using two complementary techniques (Fig. 1.1). Using a chirped pulse-Fourier transform microwave spectrometer in the 8-16 GHz region ($0.25\text{-}0.5\text{ cm}^{-1}$), we examined alcohol-water dimers in the gas phase to understand

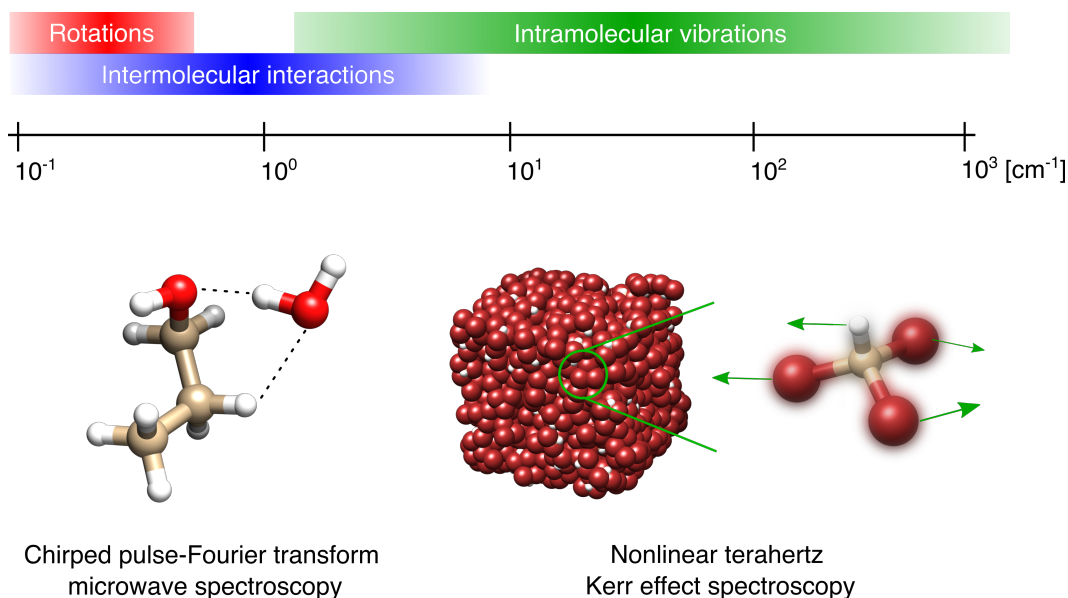


Figure 1.1: This thesis focuses on the low-energy microwave and terahertz regions of the electromagnetic spectrum. Overlapping contributions from rotations, inter- and intramolecular effects make spectra from this region congested and difficult to interpret compared to higher frequency vibrational or electronic spectroscopy. We will use two approaches, chirped pulse-Fourier transform microwave spectroscopy and nonlinear terahertz Kerr effect spectroscopy, to observe intermolecular interactions in the gas and condensed phases respectively.

ground-state hydrogen bonding interactions. Next, we performed nonlinear terahertz (THz) spectroscopy studies of room temperature liquids from 0.1-10 THz (3-333 cm^{-1}) using a first-of-its-kind single-shot multi-dimensional terahertz spectrometer. In the following sections, we discuss in more detail the particulars of each approach and key findings.

1.1 Microwave spectroscopy of gas phase molecular dimers

First, the issue of spectral ambiguity can be addressed by reducing the complexity of a system's intermolecular interactions as much as possible. This allows observation of fundamental interaction motifs, as we demonstrate in this thesis by using gas phase microwave spectroscopy to study hydrogen bonding in alcohol-water dimers. Molecular dimers can be formed with high efficiency in a vacuum chamber through collisional cooling of molecules within an argon-backed supersonic expansion. Thermal motion is converted to directed translational motion, reducing temperatures in the moving molecule frame to a few Kelvin. Clustering during this cooling process produces complexes trapped in the vibrational ground state. Next,

the rotational spectrum of the dimer is interrogated using chirped pulse-Fourier transform microwave spectroscopy. From these data, the rotational constants of the dimer can be determined, which can then help uniquely identify the dimer's structure, torsional and vibrational dynamics, and hydrogen bonding interactions between the alcohol and water molecules.

To this end, in Chap. 2 we report structural characterizations of two isopropanol-water dimers [19]. This work was performed in collaboration with Prof. Walther Caminati's group at University of Bologna. A subsequent collaboration with Elena Alonso, a visiting Ph.D. student from the University of Valladolid, resulted in characterization of two n-propanol-water dimers [20], as discussed in Chap. 3. Large degrees of conformational freedom in the n-propanol monomer required intensive ab initio searches of conformational phase space to identify all the possible stable hydrogen-bonded dimer structures. Isotopic substitution studies allowed unambiguous verification of the assigned structures through Kraitchman analysis. In both dimers studied, the water molecule was found to play a key hydrogen bonding donor role. (One of the two experimentally observed ground state structures is seen in Fig. 1.1, with hydrogen bonding interactions shown as dashed lines.)

1.2 Nonlinear terahertz spectroscopy of liquids

While microwave spectroscopy is useful for studying isolated hydrogen bonding motifs in the gas phase, a liquid's more numerous degrees of freedom, thermal energy, and continuum of bath states require a different set of tools. Terahertz spectroscopy is a natural choice since the THz photons have commensurate energies to such thermally excited bath states. We can simplify analysis of typically congested condensed phase THz spectra by studying model systems with clear chromophores. For example, halogenated methanes such as bromoform (CHBr_3 , Fig 1.1) and chloroform (CHCl_3), possess bright, easily distinguishable intramolecular vibrational modes which are close in energy to the intermolecular bath modes. As such, these liquids are useful systems for developing nonlinear THz techniques (discussed in more detail in Chap. 4).

In this thesis, we are particularly concerned with studying liquid systems using two-dimensional THz-THz-Raman (2D-TTR) spectroscopy [21]. A diagram of the 2D-TTR input fields is seen in Fig. 1.2. Briefly, this technique uses two THz fields, separated by a time t_1 , to generate a nonlinear polarization in a sample. Interrogating the sample with a Raman field at later times t_2 records the molecular

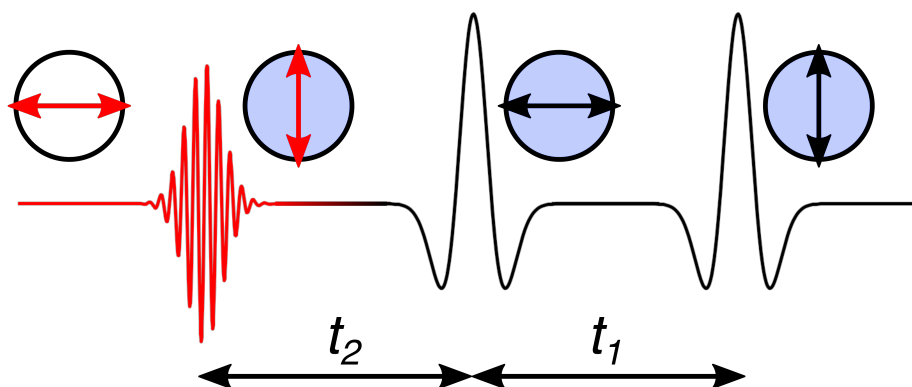


Figure 1.2: The two-dimensional terahertz-terahertz-Raman (2D-TTR) pulse sequence, time definitions, and polarization states which are used extensively in the terahertz spectroscopy section of this thesis.

response of the system, which will reflect intra- and intermolecular contributions. By adopting multi-dimensional spectroscopy techniques, molecular dynamics can be distributed along several independent axes, and in-homogeneous broadening is reduced. From the improved spectral resolution and clarity provided by 2D-TTR spectroscopy, Ioan Bogdan-Magdău, a post-doc in Prof. Thomas Miller's group, led a study of intramolecular vibrational modes in bromoform that successfully modelled electronic anharmonicities in the molecular potential energy surface [22].

Development of a single-shot THz Kerr effect spectrometer

A common characteristic of nonlinear THz spectroscopies (as well as linear THz absorption spectroscopy) is the time-domain nature of the measurements. Retro-reflector mirrors mounted on motorized delay stages precisely control the $\{t_1, t_2\}$ timings of the multiple light pulse interactions with a sample. Heterodyne detection [23] with a square-law detector directly captures the complex emitted signal field $E_{\text{Sig}}(t_1, t_2)$ while substantially enhancing the experimental signal-to-noise (Fig. 1.3 A). The main cost incurred in this approach is the unfavorable scaling of integration times with the number of independent temporal axes. While it may take only N points to sample a response along t_2 , the additional t_1 axis in 2D-TTR experiments requires integration times proportional to N^2 (Fig. 1.3 B). Time costs become particularly prohibitive with samples such as water that have very weak nonlinear responses.

Can we devise an improved measurement technique that will produce higher reso-

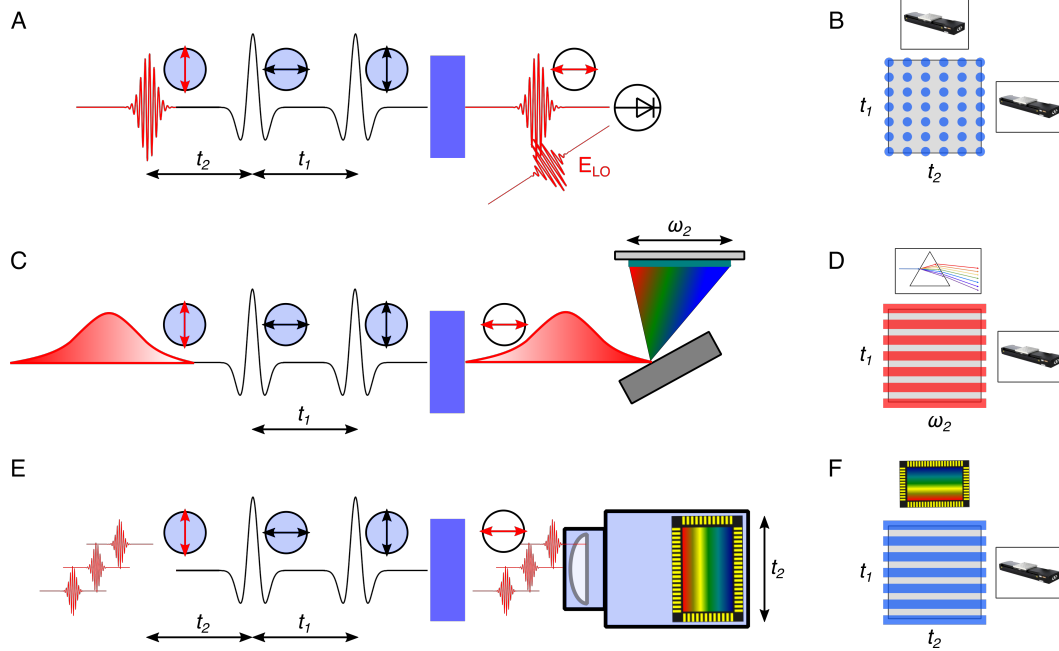


Figure 1.3: A comparison between time-domain and frequency-domain strategies for performing multi-dimensional THz spectroscopy. Traditional 2D-TTR (A) uses mechanical delay stages on both axes, resulting in squarely sampled data (B). To reduce experimental integration times, two approaches to multiplexing the t_2 measurement axis are shown. In (C), a frequency domain approach measures the Raman probe spectrum. The collected data (D) now consist of one temporal axis, t_1 , and one spectral axis, ω_2 , which is fully captured with each laser shot due to the multiplex advantage offered by the grating element. Single-shot time-domain spectroscopy (E) uses a probe pulse with a temporal wave-front. (F) Single-shot data retain both time axes, but the t_2 axis is sampled over a wide range with each laser shot.

lution data in less time? The primary inefficiency associated with the time-domain approach is a lack of multiplexing; each data point is collected by physically moving mirrors and then integrating for a period of time. In contrast, spectrometers enjoy a multiplex advantage thanks to dispersive grating elements. Thus, one potential way to speed up nonlinear THz measurements could be to build a grating spectrometer which measures Raman shifts in the probe spectrum after interactions with a sample (Fig. 1.3 C). Such an approach, however, would require very delicate spectrometer alignment, careful calibration, and expensive Raman edge filters to isolate signals. On the other hand, a full Raman spectrum of the molecular response could be captured with every laser shot, potentially offering extremely short experimental integration times (Fig. 1.3 D).

A second solution borrows the dispersive element at the heart of grating spec-

trometers, while performing the measurement in the time-domain (Fig. 1.3 E). By encoding a smoothly varying temporal wave-front across the diameter of a probe beam, a large range of dynamics along t_2 can be recorded onto a detector array (Fig. 1.3 F). The majority of this thesis work details the development and performance of such a single-shot multidimensional terahertz time-domain spectrometer. (“Spectrometer” is somewhat of a misnomer; the single-shot device averages time-domain molecular responses which may then be transformed into the frequency domain using a Fourier transform algorithm.) At the heart of the spectrometer are two components. The first is a $30 \times 30 \text{ mm}^2$ nickel block with micron-scale stair step grooves machined across its surface. These stair steps impart a temporal wave-front to a Raman probe beam, allowing tens of picoseconds of molecular dynamics to be captured on a high frame-rate Andor Zyla sCMOS camera with each laser shot.

Several hurdles were overcome during this project, including designing the optical imaging system, incorporating two nonlinear terahertz excitation fields, data capture, processing, and analysis, and incorporating phase-sensitive detection. These challenges are discussed in detail in Chap. 5. In building up to the full two-dimensional nonlinear spectrometer, we first constructed a one-dimensional single-shot spectrometer to perform optical and terahertz Kerr effect (1D-OKE, 1D-TKE) studies of liquids at room temperature. The 1D-TKE spectrometer’s construction and performance are summarized in Chap. 6 [24]. Working in collaboration with fellow graduate student Haw-Wei Lin, the second iteration of the device was constructed to capture the full 2D-TTR response of liquids. The resulting apparatus can measure orders of magnitude larger temporal ranges at a fraction of the time required for the original dual stage-scan 2D-TTR studies.

The nonlinear instrument response function

With reduced integration times and improved sensitivity, we have studied a large range of liquids and materials ranging from halogenated methanes and water, to diamond and lithium niobate. As our range of samples has increased, so too has our understanding of the nuances of 2D-TTR spectroscopy. Alongside common day-to-day fluctuations in signals due to changes in experimental alignment, we began noticing substantial inconsistencies between 2D-TTR data gathered under apparently minor changes in experimental setup. For example, small modifications in THz generation produced dramatic changes in the 2D-TTR spectrum of bromoform. These observations, on their own, were curious but did not definitively point to a particular mechanism responsible for these changes.

With data on halogenated methane liquid collected across larger temporal extents and at higher resolution, we also observed a lack of any prolonged intramolecular response along the 2D-TTR t_1 axis. While the intramolecular vibrational signal extended along t_2 for nearly 10 picoseconds, the t_1 response lasted for less than a picosecond. This behavior was not consistent with a series of discrete, temporally separated resonant interactions with a intramolecular vibrational mode. Instead, these data appeared more consistent with an instantaneous sum-frequency (SF) process, which can be viewed as the low frequency analog to Raman scattering. Since the SF pathway is linear in the polarizability operator, such signals might easily overwhelm contributions from the resonant, nonlinear pathways that had been previously considered.

As discussed in Chap. 7, additional questions were raised by the hypothesis that a strong SF pathway contributed to the intramolecular 2D-TTR response of halogenated methanes. First, how could an instantaneous excitation mechanism with no t_1 dependence still produce a response which varied along t_1 ? To address this question, we investigated the role of the instrument response function (IRF) in 2D-TTR spectroscopy. A model IRF is shown in Fig. 1.4. In the time domain, convolution of the three input electric field with the time-dependent molecular response function $R^{(3)}(t_1, t_2)$ produces a distorted signal. In the frequency domain, the IRF acts as a multiplicative window on the molecular third order nonlinear susceptibility $\chi^{(3)}(\omega_1, \omega_2)$. For bromoform and other halogenated methanes, the t_1 -independent SF $\chi^{(3)}(\omega_1, \omega_2)$ component effectively has uniform intensity along ω_1 , while the IRF power is highly featured and sensitive to minor changes in the shape of the THz electric field. Consequently, multiplication of these two terms results in complex 2D-TTR spectra which change appearance with small modifications in the THz generation process. Through two complementary modelling approaches, we have demonstrated that the spectra of bromoform and chloroform can be accurately reproduced by slicing a common IRF along ω_1 at $\omega_2 = \nu$, where ν is the frequency of each molecule's intramolecular vibrational mode [25].

2D-TTR spectroscopy of gases and materials

Apart from identifying the important role of SF pathways in 2D-TTR spectra of halogenated methanes, and clarifying the role of the IRF in 2D-TTR spectroscopy, the single-shot spectrometer has produced several other interesting observations which may be relevant to consider in future 2D-TTR experiments. First is the small, but detectable, emission from residual water vapor in the 2D-TTR experimental

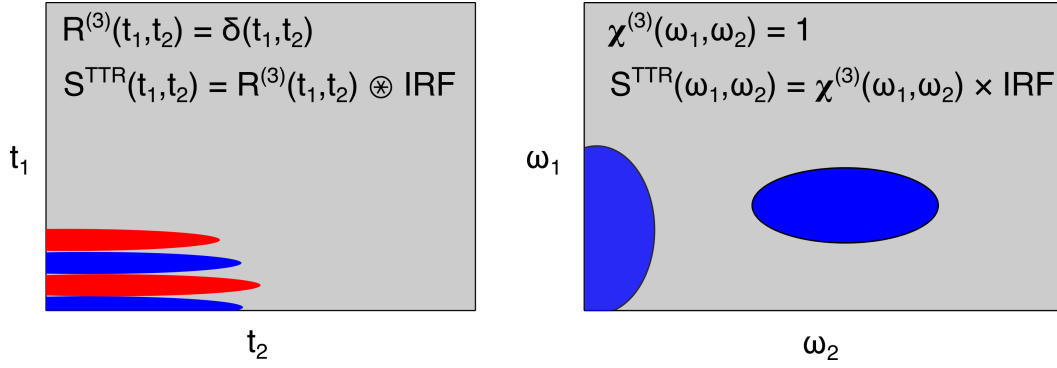


Figure 1.4: A diagram of the time and frequency domain manifestations of the 2D-TTR instrument response function (IRF). In this model, the sample's response $R^{(3)}(t_1, t_2)$ is a 2D Dirac delta function, $\delta(t_1, t_2)$, which should be sharply peaked only at $(0,0)$. Instead, time-domain convolution of this response with the IRF produces a distorted signal. In the frequency domain (right), the convolution of time-domain fields becomes a multiplication between the spectral content of the IRF and the sample's third-order susceptibility, $\chi^{(3)}(\omega_1, \omega_2)$. In the case of a 2D Dirac delta function, $\chi^{(3)}(\omega_1, \omega_2)$ is uniform across all frequency space, and the observed spectrum is determined by the distribution of the IRF's spectral power.

enclosure discussed in Chap. 8. In many liquids, such as carbon disulfide (CS_2), a long-lived oscillatory Kerr effect response is observed along t_1 . Intense THz emission from water vapor along the THz beam transport path has been identified as the origin of these secondary nonlinear signals. Future 2D-TTR measurements of liquid dynamics will need to develop methods that model and mitigate these contributions, which may hamper the observation of liquid orientational correlation functions.

Second, we present in Chap. 9 initial 2D-TTR results on a sample of lithium niobate (LiNbO_3). This ferroelectric material has an intense IR and Raman-active phonon mode at 3.9 THz that is readily excited by the experimental THz fields. Contributions from phonon excitation dominates the 2D-TTR response. Because of the non-zero $\chi^{(2)}$ susceptibility of the anisotropic sample, these results may be consistent with either a cascaded $\chi^{(2)} \cdot \chi^{(2)}$ process or with a $\chi^{(3)}$ 2D-TTR response.

A cascaded mechanism would involve optical rectification between an excited phonon mode and a THz field. The \sim DC polarization produced in the sample would alter the sample refractive index, which would be subsequently probed by the Raman field via a linear Pockels effect.

In contrast, the data are also consistent with a $\chi^{(3)}$ 2D-TTR response related to

anharmonicity of the polarizability operator in lithium niobate. In this interpretation, the oscillatory emission from phonon modes along t_1 may contribute, like water vapor in CS₂, to the overall IRF of the experiment. This observation is important for developing an interpretation of the 2D-TTR data which is consistent with lessons learned from the halogenated methane studies.

BIBLIOGRAPHY

1. E. S. Kryachko, O. E. Yanovitskii, The model of librational motion in liquid waters. en, *Journal of Molecular Structure: THEOCHEM* **227**, 131–145, DOI 10.1016/0166-1280(91)85279-G (Mar. 1991).
2. A. V. Onufriev, S. Izadi, Water models for biomolecular simulations: Water models for biomolecular simulations. en, *WIREs Comput Mol Sci* **8**, e1347, DOI 10.1002/wcms.1347 (Mar. 2018).
3. K. R. Hadley, C. McCabe, Coarse-grained molecular models of water: a review. en, *Molecular Simulation* **38**, 671–681, DOI 10.1080/08927022.2012.671942 (July 2012).
4. T. J. Dick, J. D. Madura, en, in *Annual Reports in Computational Chemistry* (Elsevier, 2005), vol. 1, pp. 59–74, DOI 10.1016/S1574-1400(05)01005-4.
5. S. Naserifar, W. A. Goddard, Liquid water is a dynamic polydisperse branched polymer. en, *Proc Natl Acad Sci USA* **116**, 1998–2003, DOI 10.1073/pnas.1817383116 (Feb. 2019).
6. S. Naserifar, W. A. Goddard, The quantum mechanics-based polarizable force field for water simulations. en, *J. Chem. Phys.* **149**, 174502, DOI 10.1063/1.5042658 (Nov. 2018).
7. A. K. Das *et al.*, Development of an Advanced Force Field for Water Using Variational Energy Decomposition Analysis. en, *J. Chem. Theory Comput.* **15**, 5001–5013, DOI 10.1021/acs.jctc.9b00478 (Sept. 2019).
8. M. Thämer, L. De Marco, K. Ramasesha, A. Mandal, A. Tokmakoff, Ultrafast 2D IR spectroscopy of the excess proton in liquid water. en, *Science* **350**, 78–82, DOI 10.1126/science.aab3908 (Oct. 2015).
9. M. W. Evans, G. C. Lie, E. Clementi, Molecular dynamics of liquid water in a circularly polarized external field. en, *The Journal of Chemical Physics* **87**, 6040–6045, DOI 10.1063/1.453476 (Nov. 1987).
10. P. S. Cremer, A. H. Flood, B. C. Gibb, D. L. Mobley, Collaborative routes to clarifying the murky waters of aqueous supramolecular chemistry. en, *Nature Chem* **10**, 8–16, DOI 10.1038/nchem.2894 (Jan. 2018).
11. D. Sidler, P. Hamm, Feynman diagram description of 2D-Raman-THz spectroscopy applied to water. en, *J. Chem. Phys.* **150**, 044202, DOI 10.1063/1.5079497 (Jan. 2019).
12. P. Hamm, Velocity echoes in water. en, *J. Chem. Phys.* **151**, 054505, DOI 10.1063/1.5112163 (Aug. 2019).

13. F. Novelli *et al.*, Strong Anisotropy in Liquid Water upon Librational Excitation Using Terahertz Laser Fields. en, *J. Phys. Chem. B* **124**, 4989–5001, DOI 10.1021/acs.jpcc.0c02448 (June 2020).
14. J. Savolainen, S. Ahmed, P. Hamm, Two-dimensional Raman-terahertz spectroscopy of water. en, *Proceedings of the National Academy of Sciences* **110**, 20402–20407, DOI 10.1073/pnas.1317459110 (Dec. 2013).
15. D. Laage, T. Elsaesser, J. T. Hynes, Water Dynamics in the Hydration Shells of Biomolecules. en, *Chem. Rev.* **117**, 10694–10725, DOI 10.1021/acs.chemrev.6b00765 (Aug. 2017).
16. A. Biela *et al.*, Dissecting the Hydrophobic Effect on the Molecular Level: The Role of Water, Enthalpy, and Entropy in Ligand Binding to Thermolysin. en, *Angew. Chem. Int. Ed.* **52**, 1822–1828, DOI 10.1002/anie.201208561 (Feb. 2013).
17. V. Conti Nibali, M. Havenith, New Insights into the Role of Water in Biological Function: Studying Solvated Biomolecules Using Terahertz Absorption Spectroscopy in Conjunction with Molecular Dynamics Simulations. en, *J. Am. Chem. Soc.* **136**, 12800–12807, DOI 10.1021/ja504441h (Sept. 2014).
18. C. C. M. Groot, K. Meister, A. L. DeVries, H. J. Bakker, Dynamics of the Hydration Water of Antifreeze Glycoproteins. en, *J. Phys. Chem. Lett.* **7**, 4836–4840, DOI 10.1021/acs.jpclett.6b02483 (Dec. 2016).
19. L. Evangelisti *et al.*, Conformational equilibrium and internal dynamics in the iso-propanol–water dimer. en, *Phys. Chem. Chem. Phys.* **19**, 568–573, DOI 10.1039/C6CP06315B (2017).
20. G. J. Mead, E. R. Alonso, I. A. Finneran, P. B. Carroll, G. A. Blake, Identification of two conformationally trapped n -propanol-water dimers in a supersonic expansion. en, *Journal of Molecular Spectroscopy* **335**, 68–73, DOI 10.1016/j.jms.2017.03.008 (May 2017),
21. I. A. Finneran, R. Welsch, M. A. Allodi, T. F. Miller, G. A. Blake, 2D THz-THz-Raman Photon-Echo Spectroscopy of Molecular Vibrations in Liquid Bromoform. en, *J. Phys. Chem. Lett.* **8**, 4640–4644, DOI 10.1021/acs.jpclett.7b02106 (Sept. 2017).
22. I. B. Magdău, G. J. Mead, G. A. Blake, T. F. Miller, Interpretation of the THz-THz-Raman Spectrum of Bromoform. en, *J. Phys. Chem. A* **123**, 7278–7287, DOI 10.1021/acs.jpca.9b05165 (Aug. 2019),
23. S. F. Jacobs, Optical heterodyne (coherent) detection. en, *American Journal of Physics* **56**, 235–245, DOI 10.1119/1.15655 (Mar. 1988).
24. G. J. Mead, I. Katayama, J. Takeda, G. A. Blake, An echelon-based single shot optical and terahertz Kerr effect spectrometer. *Review of Scientific Instruments* **90**, 053107, DOI 10.1063/1.5088377 (May 2019),

25. G. J. Mead, H.-W. Lin, I.-B. Magdau, T. F. Miller, G. A. Blake, Sum-Frequency Signals in 2D-Terahertz-Terahertz-Raman Spectroscopy. en, *J. Phys. Chem. B*, acs.jpcb.0c07935, DOI 10.1021/acs.jpcb.0c07935 (Sept. 2020),

Part II

Microwave Spectroscopy

Chapter 2

CONFORMATIONAL EQUILIBRIUM AND INTERNAL DYNAMICS IN THE ISOPROPANOL–WATER DIMER

We begin our investigation of hydrogen bonding in gas phase alcohol water dimers by using chirped-pulse Fourier transform microwave spectroscopy to characterize complexes of isopropanol and water. Two distinct rotational spectra have been assigned, corresponding to two different conformations of the dimer. Because of the sensitivity of rotational spectroscopy to molecular geometry, we can identify with precision the conformational structure of each dimer. In both cases, the water molecule donated a proton to the isopropanol hydroxyl group, whose free hydrogen was oriented in a *gauche* conformation. The isomer in which the water molecule is oriented along the symmetry plane of the isopropanol molecule (inner) is more stable than the second isomer, where the water is positioned outside the isopropanol symmetry plane (outer). The rotational transitions of the inner isomer display a doubling, due to the two equivalent minima related to the internal rotation of the hydroxyl group in concert with rearrangement of the water unit. The tunneling splitting has been determined to be 25.16(8) GHz, corresponding to a B₂ barrier of 440 cm⁻¹.

Most of this chapter has been reproduced with permission from the PCCP Owner Societies from:

L. Evangelisti *et al.*, Conformational equilibrium and internal dynamics in the iso-propanol–water dimer. *en, Phys. Chem. Chem. Phys.* **19**, 568–573, DOI 10.1039/C6CP06315B (2017)

2.1 Introduction

The small size of the water monomer and its double-donor/double-acceptor capacities give it great flexibility in forming a variety of hydrogen bonds. A recent paper presents a cataloguing of the interactions of water with organic molecules, as obtained by the rotational spectra of their molecular complexes isolated in supersonic expansions [2]. In such complexes, water can undergo internal motions, where the dynamics depend on water's proton donor or proton acceptor role. These dynamics are generally enhanced, generating features such as the doubling of rotational transitions when water acts as a proton acceptor [3, 4].

Adducts of water with alcohols are characterized by a relatively strong $\text{O}-\text{H}\cdots\text{O}$ hydrogen bond linking the two subunits. These alcohol–water structures may be further stabilized with weaker complementary hydrogen bonds between alkyl protons and the water oxygen [5]. Internal dynamics often complicate the rotational spectra, but allow a determination of the intermolecular potential energy surfaces along the motions of interest. Due to the amphoteric nature of the water and alcohol hydroxyl groups, each can act either as the proton donor or the proton acceptor.

In the pioneering rotational study of methanol–water it was shown that the observed species consisted of a water–donor, methanol–acceptor complex [6]. The spectrum was complicated by the internal rotation of the methyl group, such that the spectroscopic parameters were reported only for the internal rotation A-state. Similarly, water acts as proton donor in the adduct tert-butanol–water [2]. The tert-butanol hydroxyl group tunnels between two equivalent minima – involving also a considerable rearrangement of water – that generates splittings of the rotational transitions. From these splittings, the corresponding potential energy function has been estimated. The same hydrogen bonding motif (where water serves as the proton donor) has been recently found in the adduct of water with ethanol [7], and in glycidol–water, the water moiety acts both as a proton donor and a proton acceptor forming two strong $\text{O}-\text{H}\cdots\text{O}$ hydrogen bonds within a cyclic structure [8].

A different behavior has been encountered in phenol–water where water has the role of proton acceptor [9]. Here, water undergoes a two-dimensional (2D) motion (a combination of internal rotation and inversion) between four (2×2 equivalent) minima on the 2D intermolecular potential energy surface.

Additional studies of the rotational spectra of adducts of water with larger aliphatic alcohols, such as water–propanol, would help to understand the interplay between the hydrophobic and -philic interactions in such clusters. Here we are interested

in the adduct of water with isopropanol (IP–W), a dimer with a conformational equilibrium taking place between the *gauche* and *trans* forms of isopropanol [10]. In a related complex, hexafluoroisopropanol–water [11], only one conformer was observed, wherein *trans*-hexafluoroisopropanol acts as a proton donor to the water, a motif similar to phenol–water. Most likely, it is the high degree of fluorination that inverts the usual conformational behavior observed for the aliphatic alcohol–water complexes.

2.2 Experimental approach

The rotational spectra of IP–W isotopologues have been measured in two different laboratories:

(a) Caltech. Data were collected from 6–18 GHz using a previously described chirped pulse-Fourier transform microwave (CP-FTMW) spectrometer [7]. Selective excitation of a sample with broad bandwidth microwave pulses ($\Delta\omega \approx 4$ GHz) was achieved in a two-step process. First, a DC-2 GHz chirp was produced by generating a rapid, linear frequency sweep on an Analog Devices 9914 direct digital synthesizer board (DDS) [12]. As shown in Fig. 2.1, this chirp (labelled R) was then combined in a microwave mixer with a local oscillator (L) tuned to an arbitrary higher frequency ω . The mixer produced a 4 GHz wide intermediate frequency (I) ranging across $\omega \pm 2$ GHz. Power was increased with a gallium nitride microwave amplifier. Broadcast of the pulse into the vacuum chamber then polarized dimers formed in a coincident pulsed supersonic molecular expansion. In these experiments, a reservoir nozzle was filled with a 1:1 molar mixture of isopropanol and water, and heated to ≈ 40 degree Celsius. Argon at 46 psi pressurized the nozzle. The nozzle was pulsed at 10 Hz, creating a supersonic expansion perpendicular to two waveguide horns. Forty $1\ \mu\text{s}$ duration chirps were broadcast with each gas pulse. After polarization with the chirped pulse, detection of the molecular free induction decay (FID) used the same process in reverse. A second microwave horn detected the decaying FID, and the signal was down-converted in a second mixer back to DC-2 GHz. This low frequency signal was then easily recorded with a high speed Agilent digitizer card. Data were collected for 300 seconds at each local oscillator setting. Line centers were measured to an accuracy of 20 kHz.

(b) UNIBO. Measurements were performed between 6–18.5 GHz using a pulsed jet Fourier transform microwave (PJFTMW) spectrometer described elsewhere [13], based on the pioneering designs of Flygare [14] and Grabow [15]. Adducts were

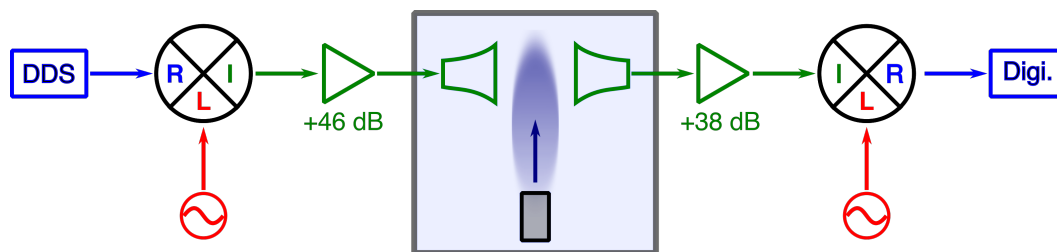


Figure 2.1: A schematic diagram of the CP-FTMW spectrometer. A direct digital synthesizer (DDS) generated a DC-2 GHz chirp. Upon mixing with a local oscillator at ω GHz, the $\omega \pm 2$ GHz pulse was amplified and emitted into the vacuum chamber. A supersonic gas expansion, polarized by the pulse, emits a molecular FID which was detected by a second microwave horn. Down-conversion with the same LO yielded an easily digitized waveform for further analysis.

formed by flowing helium through a stainless steel reservoir containing a 50% by mole mixture of isopropanol and water, and running the resulting gaseous mixture through a pulsed supersonic expansion. Rotational frequencies were determined after the Fourier transform of 8000-data point time-domain FIDs, recorded with 40 ns sampling intervals. The pulsed molecular beam was introduced parallel to the axis of the Fabry–Pérot resonator. Consequently, each observed transition appeared as a Doppler doublet, and the line frequency was determined as the arithmetic mean of the frequencies of the two Doppler components. The accuracy of frequency measurements is estimated to be better than 3 kHz.

2.3 Ab initio calculations

Before searching for the rotational spectrum, we ran several theoretical calculations, in order to constrain reliable starting conformations for spectral assignment. The MP2/6-311++G(d,p) level of theory was used, in Gaussian09 [16].

Five energy minima were found, shown in Fig. 2.2, corresponding to the *trans* or *gauche* conformation of isopropanol, to the proton donor or proton acceptor role of water, and to the orientation of water with respect to the symmetry plane of *gauche* isopropanol (Inner indicates water is oriented along the IP symmetry plane; Outer indicates water is oriented perpendicular to the IP symmetry plane). The corresponding spectroscopic parameters are listed in Table 2.1.

As has been seen for the simpler aliphatic alcohol adducts, the complexes where the water acts as a proton donor are more stable, and, as for ethanol–water dimer, the *gauche* conformation of the alcohol is preferred. Cooperative water donor/isopropanol

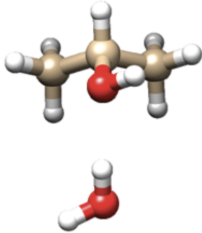
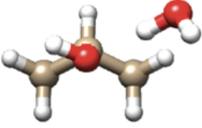
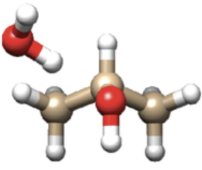
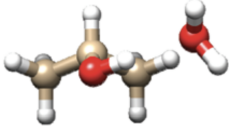
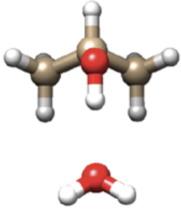
IP is the proton acceptor			
	<i>GAI</i> ^a	<i>GAO</i>	<i>TA</i>
	$\Delta E/\text{cm}^{-1}$ 0 ^b	102	128
IP is the proton donor			
	<i>GD</i>	<i>TD</i>	
	$\Delta E/\text{cm}^{-1}$ 248	433	

Figure 2.2: Conformations and relative energies of the 5 most stable forms of IP-W.

^a G = *gauche*, T = *trans*, A = Acceptor (Alcohol), D = Donor (Alcohol), I = Inner (position of water), O = Outer (position of water). ^b Absolute energy = -270.134153 E_h.

acceptor structures (GAI, GAO, and TA) comprise the three lowest energy dimers, while anti-cooperative hydrogen bonding increases the GD and TD dimer energies by over 100 cm⁻¹. The relative energy difference between GAI, GAO, and TA indicates the *trans/gauche* position of the alcohol hydroxyl may account for ~20 cm⁻¹ in energy. However, a significant stabilization of 100 cm⁻¹ occurs when the water is oriented symmetrically between the alcohol's two methyl groups, as in GAI. This stabilization is likely attributable to increased opportunities and/or improved alignment for secondary stabilizing C-H...OH₂ bonding interactions.

As has been seen for the simpler aliphatic alcohol adducts, the complexes where the water acts as a proton donor are more stable, and, as for ethanol-water dimer, the *gauche* conformation of the alcohol is preferred. Cooperative water donor/isopropanol acceptor structures (GAI, GAO, and TA) comprise the three lowest energy dimers, while anti-cooperative hydrogen bonding increases the GD and TD dimer energies by over 100 cm⁻¹. The relative energy difference between GAI, GAO, and TA in-

	GAI	GAO	TA	GD	TD
A [MHz]	5121.4	8058.8	7528.5	8039.6	5188.1
B [MHz]	2527.4	2073.1	2155.3	1996.1	2364.8
C [MHz]	2388.2	1758.2	1837.5	1701.5	2225.1
μ_A [D]	1.95	-2.62	2.42	3.07	-2.69
μ_B [D]	0.20	-1.17	0.87	-0.83	0.00
μ_C [D]	1.51	-0.64	0.37	-0.48	1.62

Table 2.1: MP2/6-311++G(d,p) calculated spectroscopic parameters of the five most stable IP-W dimers.

icates the *trans/gauche* position of the alcohol hydroxyl may account for 20 cm^{-1} in energy. However, a significant stabilization of 100 cm^{-1} occurs when the water is oriented symmetrically between the alcohol’s two methyl groups, as in GAI. This stabilization may be attributed to increased opportunities and/or improved alignment for secondary stabilizing C-H \cdots OH₂ bonding interactions.

2.4 Results: GAI (Inner) conformer

Rotational spectrum

The rotational spectrum of this isomer was assigned at Caltech, using the SP-FIT/SPCAT suite of programs [17] and a graphical Python fitting program. Double resonance of assigned transitions was performed to validate the fit. Later on, complementary measurements were performed at UNIBO. Rotational transitions are split into two component lines, with an intensity ratio of about 5:1, corresponding to a vibrational splitting of about 1 cm^{-1} . The doublet of the $2_{1,1} \leftarrow 1_{1,0}$ transition is shown in Fig. 2.3 A. Since the GAI isomer is a near symmetric top, the S-reduction and I' representation have been chosen [18]. The fitted spectroscopic parameters are reported in Table 2.2.

Isotopologues were not assigned for the GAI isomer due to their complex spectra. Instead, the justification for our structural assignment comes from the good agreement between predicted and experimental rotational constants. The intensities of the GAI and GAO transitions also agree with relative populations consistent with the ab initio energies. Finally, the flexible model analysis based upon the GAI structure (mentioned next) faithfully reproduces splitting of transitions ascribed to that isomer.

The fitting of the transition frequencies was complicated by the Coriolis’ interactions between the $\nu=0$ and $\nu=1$ vibrational levels. The following coupled Hamiltonian

Table 2.2: Experimental spectroscopic constants of IP-W-GAI (S-reduction, I' representation). ^aErrors in parenthesis are expressed in units of the last digit. ^bStandard deviation of the fit. ^cNumber of fitted transitions.

	$\nu=0$	$\nu=1$
A [MHz]	5098.624(3) ^a	5099.953(3)
B [MHz]	2485.250(1)	2484.560(1)
C [MHz]	2353.853(1)	2352.743(1)
D_J [kHz]	7.98(4)	
D_{JK} [kHz]	21.6(2)	
D_K [kHz]	-17.3(6)	
d_1 [kHz]	0.27(2)	
ΔE_{01} [GHz]	25.16(8)	
F_{ab} [MHz]	47.87(2)	
F_{bc} [MHz]	4.2(1)	
σ^b [kHz]	3.7	
N^c	33	

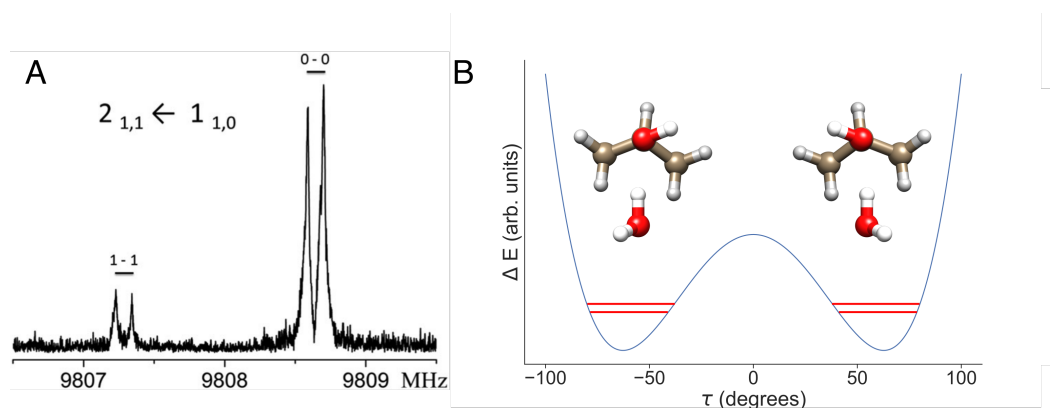


Figure 2.3: A) Tunneling components of the $2_{1,1} \leftarrow 1_{1,0}$ transition. Each of the peaks are further doubled by the Doppler effect. B) The tunneling motion in of IP-W-GAI is predominantly due to the internal rotation of the hydroxyl group, accompanied by a structural relaxation of the “free” water hydrogen

was therefore used:

$$H = H_0^R + H_1^R + H^{CD} + H^{int} \quad (2.1)$$

where H_0^R and H_1^R account for the rotational energies for the 0 and 1 substates, respectively, H^{CD} represents the centrifugal distortion corrections (forced to the same value for $\nu=0$ and $\nu=1$), and H^{int} the interaction between the $\nu=0$ and $\nu=1$ states, expressed as:

$$H^{int} = \Delta E_{01} + [F_{bc}(P_b P_c + P_c P_b)] + [F_{ab}(P_a P_b + P_b P_a)] \quad (2.2)$$

ΔE_{01} is the energy difference between the 0 and 1 sub-states, while F_{bc} and F_{ab} are Coriolis' coupling parameters. The $(P_c P_a + P_a P_c)$ Coriolis term was not used in the fit, consistent with an inversion motion through the b-axis. This inversion motion is further verified in the ab initio structure, which confirms that the proton movements occur along the b-axis.

Flexible model analysis of the tunneling motion

The determined ΔE_{01} splitting is related to the barrier between the two equivalent minima (Fig. 2.3 B) as a function of the internal rotation of the OH group (given by the dihedral angle τ), the amplitude of the motion (in our case a $\approx 120^\circ$ rotation of the OH group), and the reduced mass of the motion, which is a function of τ and also of the structural relaxation which takes place in the complex.

Meyer's flexible model [19, 20] is especially suitable to determine potential energy surfaces from rotational and vibrational experimental data. In our case we consider τ as the key parameter to describe the motion, with any structural relaxations of the dimer taken into account as a function of τ .

In principle, the OH internal rotation should be described by a periodic function, but, considering the shape of the potential energy function (that is, when OH is in the *trans* position, the potential energy is very high), we can reasonably assume that the tunneling effects are produced 'locally' in the range of the HO-CH dihedral angle (τ) between ca. -120 and $+120^\circ$. In this case, the potential can be described by the two parameters required in the following double minimum potential:

$$V(\tau) = B_2[1 - (\tau/\tau_0)^2]^2 \quad (2.3)$$

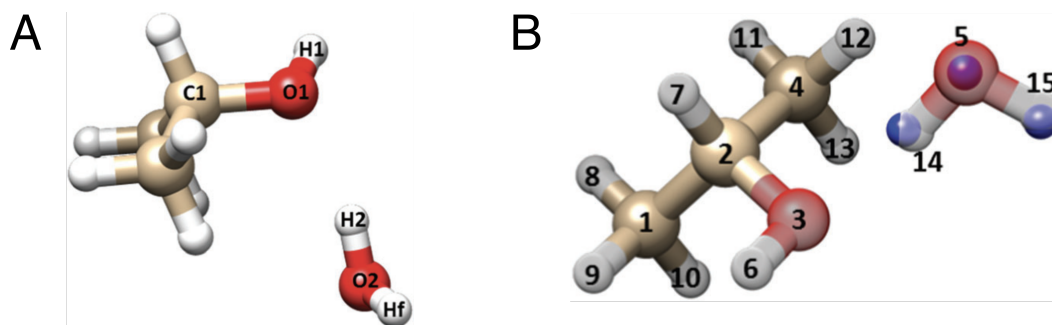


Figure 2.4: A) Structure of the GAI (Inner) conformer of IP-W, with labeling of the atoms involved in the flexible model analysis of IP-W-GAI. Hf indicates the “free” (not involved in the hydrogen bond) water hydrogen. B) Structure of the GAO (Outer) conformer of IP-W, with atom numbering. The r_s substitution positions of the three water atoms are shown as smaller blue spheres, superimposed to the MP2/6-311++G(d,p) geometry.

where B_2 is the barrier at $\tau = 0^\circ$ and τ_0 is the equilibrium value of the inversion angle. Since we have only one data point, we fixed τ_0 at its ab initio value (62.7°). Guided by the ab initio structural differences between the energy minimum ($\tau = \tau_0$) and the transition state ($\tau = 0^\circ$), we took into account the structural relaxations of four structural parameters as a function of the leading parameter τ , according to the following expressions (see Fig. 2.4 A for numbering of atoms in the structural parameters):

$$\angle \text{H2O2-O1C1} = 180 - 30.7(\tau/\tau_0) \quad (2.4)$$

$$\angle \text{HfO2-H2O1} = 180 - 10.3(\tau/\tau_0) \quad (2.5)$$

$$\angle \text{H2O2O1} = 15.3 - 3(1 - \cos(3\tau)) \quad (2.6)$$

$$R(\text{O2} \leftrightarrow \text{O1}) = 2.843 + 0.006(1 - \cos(3\tau)) \quad (2.7)$$

Applying Meyer’s one-dimensional flexible model, a barrier of $B_2 \sim 440 \text{ cm}^{-1}$ best reproduced the experimental value of ΔE_{01} . In the flexible model calculations the τ coordinate has been considered in the $\pm 120^\circ$ range and solved into 81 mesh points [19, 20].

2.5 Results: GAO (Outer) isomer

Rotational spectra

The spectrum of this species was observed only at UNIBO, using He as carrier gas. It is possible that a supersonic expansion with Ar encourages GAO to conformationally relax into GAI [21]. Here, the μ_a -dipole moment component has the highest value; for this reason we first scanned the frequency region expected to include the $J=2 \leftarrow 1$ μ_a -bands of all species. We could identify only one triplet composed of the $2_{1,2} \leftarrow 1_{1,1}$, $2_{0,2} \leftarrow 1_{0,1}$, and $2_{1,1} \leftarrow 1_{1,0}$ individual transitions. We could easily extend the assignment up to the $J=4 \leftarrow 3$ μ_a -band and to 4 additional μ_b - and μ_c -transitions, for a total of 16 rotational lines. The measured transition frequencies have been fitted with a semi-rigid Hamiltonian [18], obtaining the spectroscopic parameters (rotational constants and 4 quartic centrifugal distortion constants) reported in the first column of Table 3.

The experimental values of the rotational constants match best with those calculated for the GAO species, that is isopropanol in the *gauche* isomer acting as a proton acceptor, and with H₂O in the outer position. This interpretation was confirmed by the assignment of the rotational spectra of four additional isotopologues, obtained by deuteration of the water hydrogens, or by replacing H₂O with H₂¹⁸O in the pre-expansion mixture. The rotational frequencies (generally a smaller number with respect to the parent species) of the isotopologues were fitted with the same procedure used for the parent species. Occasionally, some centrifugal distortion constants were not determinable and therefore were fixed to the values of the parent species. All the obtained spectroscopic parameters are listed in Table 2.3.

Structural information

Some structural information has been obtained from the six available rotational constants. First the Kraitchman coordinates [22] of the water oxygen and of the water hydroxyl hydrogen atoms were calculated in the principal axis system of the parent species. The obtained values are reported in Table 2.4 (see Fig. 2.4 B for atom numbering), where the ab initio and the partial r_0 (see below) values are also given for comparison. The ab initio values correspond to the bottom of the vibrational potential energy surface and are indicated by the notation r_e (or equilibrium structure).

A partial r_0 structure which reproduces the rotational constants in the vibrational ground state has been determined by adjusting, with respect to the ab initio geometry,

Table 2.3: Experimental spectroscopic parameters of the isotopologues of the GAO (Outer) conformer of IP-W. ^aError in parentheses in units of the last digit. ^bValues in brackets were fixed at the corresponding value of the parent species. ^cNumber of lines in the fit. ^dRoot-mean-square deviation of the fit.

	IP-H2O	IP-H218O	IP-DOH	IP-HOD	IP-D2O
A [MHz]	7918.293(1) ^a	7909.561(1)	7902.499(2)	7855.730(2)	7845.8(1)
B [MHz]	2049.4385(7)	1928.2259(3)	2021.8056(3)	1960.3019(3)	1934.9157(3)
C [MHz]	1745.1053(7)	1656.8025(3)	1724.2112(4)	1682.2996(4)	1662.5451(4)
D _J [kHz]	7.15(1)	6.878(5)	6.642(7)	7.485(7)	6.374(9)
D _{JK} [kHz]	-36.43(6)	-39.2(2)	-34.5(2)	-50.7(2)	[36.43]
d ₁ [kHz]	-0.29(2)	[-0.29] ^b	[-0.29]	[-0.29]	[-0.29]
d ₂ [Hz]	-0.043(5)	[-0.043]	[-0.043]	[-0.043]	[-0.043]
N ^c	16	15	12	12	9
σ ^d [kHz]	2.3	2.7	3.2	4.2	4.0

Table 2.4: Experimental (r_s and r_0), and ab initio (r_e , MP2/6-311++G(d,p)) coordinates of the substituted atoms of the GAO (Outer) conformer of IP-W. ^aError in parenthesis are in units of the last digits. ^bCalculated from the partial r_0 structure of Table 2.5, combined with the ab initio structure.

		O5	H14	H15
a [Å]	r_s	2.8098(5) ^a	1.8454(8)	3.2916(5)
	r_0^b	2.8240	1.9512	3.3367
	r_e	2.8021	1.9283	3.3072
b [Å]	r_s	0.03(3)	0.370(4)	0.237(6)
	r_0	0.0189	0.3411	0.0355
	r_e	0.0073	0.3550	0.1835
c [Å]	r_s	0.193(7)	0.07i	0.693(2)
	r_0	0.1983	0.0703	0.6119
	r_e	0.1642	0.0667	0.6162

Table 2.5: Partial r_0 and r_e geometry, and derived hydrogen bond length of the GAO (Outer) conformer of IP-W. ^a MP2/6-311++G(d,p) values. ^b Error in parentheses in units of the last digit.

Fitted parameters	r_e^a	r_0
r O5 \leftrightarrow O3 [Å]	2.8602	2.869(3) ^b
\angle O5O3-C2C1 [°]	178.3	184.0(2)
\angle H15O5-O3C2 [°]	-144.6	-138(8)
Derived H-bond distance	r_e^a	r_0
r OH \leftrightarrow O [Å]	1.898	1.908

the O5-O3 distance and the \angle O5O3-C2C1 and \angle H15O5-O3C2 dihedral angles (see Table 2.5). The discrepancies between the experimental and calculated values of the rotational constants with such an effective structure have been reduced by 90% with respect to the pure ab initio geometry. The r_0 value of the O5 \leftrightarrow O3 distance is about 0.01 Å larger than the ab initio data, according to the ground state vibrational effects for the stretching motion leading to dissociation.

2.6 Results: Conformational equilibrium

Relative intensity measurements of nearby a-type transitions of GAI $\nu=0$ and GAO (in He) showed that the normalized intensities of the Inner species were about 3 times higher than those of the Outer adduct. Taking into account the values of the μ_a dipole moment component, one can extrapolate a population ratio $\sim 4/1$ in favor

of the Inner conformer, in the $\nu=0$ state. About 80% of the ground state population of the Inner species is in the $\nu=0$ state, while Outer is doubly degenerate. Thus, we should increase this ratio by a factor 8/5, that is, a population ratio of $\sim 6/1$.

Assuming that no conformational relaxation takes place during the supersonic expansion, a relative energy difference of 370 cm^{-1} would be estimated (from $\Delta E_{0,0} = kT \ln(\text{ratio})$). This value is much larger than the ab initio value, but the formation and dissociation of the adduct is likely to take place many times during the supersonic expansion, finally favoring the population of the most stable species.

It is somewhat surprising that the TA conformer was not observed as the energy difference is only 26 cm^{-1} with respect to GAO. However, the absence of *trans* species seems to be a general feature of this kind of complex. For example: (i) in the dimer of isopropanol we measured the rotational spectra of 5 conformers, but in only one of them the *trans* form was present. In addition, some conformers containing *trans* monomers, which have been calculated to be more stable than some of the observed species, have not been detected [23]; (ii) in ethanol–water only the *gauche* form has been observed [7]. Strong conformational relaxation of isopropanol monomer from *trans* to *gauche* has been previously reported and may also help explain the lack of observed TA [21]. Assuming the calculated energy difference between GAI and GAO (102 cm^{-1}) is roughly correct, the observed GAI/GAO population ratio suggests an effective temperature of ~ 82 Kelvin. At 82 Kelvin we expect a TA/GAI population ratio of $\sim 1/10$. Therefore, if present, TA transitions should be detectable given the experimental noise floor. However, no other observable transitions could be fit and attributed to the TA conformer. Given the strong relaxation of the isopropanol monomer to the *gauche* conformation, there may be so little TA present in the expansion that the conformer is rendered undetectable. To fully analyze this question will involve detailed modeling of the interconversion barriers in the isopropanol monomer and the isopropanol–water dimer, which are outside the scope of this paper.

2.7 Conclusion

The present study confirms the inclination of aliphatic alcohols to play a proton acceptor role in their complexes with water, as observed in the previous investigations of this kind [2, 6, 7, 8]. Such a trend appears to be inverted upon fluorination of the aliphatic chain, as shown by Shahi and Arunan in the case of hexafluoroisopropanol–water [11]. In addition, aromatic alcohols (phenols) adopt a proton donor

role upon complexation with one water molecule [9]. Secondary weak hydrogen bonding interactions between alkyl protons also appear to play a stabilizing role. Orientation of the water to maximize the number of secondary CH–O interactions may stabilize the GAI isomer by a significant amount (prediction $\sim 100\text{ cm}^{-1}$, experiment $\sim 370\text{ cm}^{-1}$) compared to GAO. This is despite the known energetic cost of water accepting more than one hydrogen bond [5]. The acceptance of more than one weak CH \cdots O interaction by the water oxygen may be achieved by changes to hydrogen bond lengths in GAI cf. GAO. Ab initio structures indicate weak hydrogen bond lengths of 2.83 Å and 2.94 Å for GAI, and 2.79 Å for GAO. Therefore, we may conclude that multiple, comparatively weaker hydrogen bonding interactions may be favoured over a single stronger hydrogen bond in certain alcohol–water complexes. That ab initio calculations successfully predict the structures of isopropanol–water dimers indicates appropriate consideration of weaker hydrogen bonds into structural calculations.

BIBLIOGRAPHY

1. L. Evangelisti *et al.*, Conformational equilibrium and internal dynamics in the iso-propanol–water dimer. en, *Phys. Chem. Chem. Phys.* **19**, 568–573, DOI 10.1039/C6CP06315B (2017).
2. L. Evangelisti, W. Caminati, Internal dynamics in complexes of water with organic molecules. Details of the internal motions in tert-butylalcohol–water. en, *Phys. Chem. Chem. Phys.* **12**, 14433, DOI 10.1039/c0cp01195a (2010).
3. S. Melandri, M. E. Sanz, W. Caminati, P. G. Favero, Z. Kisiel, The Hydrogen Bond between Water and Aromatic Bases of Biological Interest: An Experimental and Theoretical Study of the 1:1 Complex of Pyrimidine with Water. en, *J. Am. Chem. Soc.* **120**, 11504–11509, DOI 10.1021/ja982192s (Nov. 1998).
4. S. Blanco, J. C. Lopez, J. L. Alonso, P. Ottaviani, W. Caminati, Pure rotational spectrum and model calculations of indole–water. en, *The Journal of Chemical Physics* **119**, 880–886, DOI 10.1063/1.1578996 (July 2003).
5. G. R. Desiraju, T. Steiner, *The weak hydrogen bond: in structural chemistry and biology*, eng, OCLC: 246186951 (Oxford Univ. Pr, Oxford, 1999).
6. P. A. Stockman, G. A. Blake, F. J. Lovas, R. D. Suenram, Microwave rotation-tunneling spectroscopy of the water–methanol dimer: Direct structural proof for the strongest bound conformation. en, *The Journal of Chemical Physics* **107**, 3782–3790, DOI 10.1063/1.474736 (Sept. 1997).
7. I. A. Finneran, P. B. Carroll, M. A. Allodi, G. A. Blake, Hydrogen bonding in the ethanol–water dimer. en, *Phys. Chem. Chem. Phys.* **17**, 24210–24214, DOI 10.1039/C5CP03589A (2015).
8. A. R. Conrad, N. H. Teumelsan, P. E. Wang, M. J. Tubergen, A Spectroscopic and Computational Investigation of the Conformational Structural Changes Induced by Hydrogen Bonding Networks in the GlycidolWater Complex. en, *J. Phys. Chem. A* **114**, 336–342, DOI 10.1021/jp908351u (Jan. 2010).
9. S. Melandri, A. Maris, P. G. Favero, W. Caminati, Free jet absorption millimetre-wave spectrum and model calculations of phenol–water. en, *Chemical Physics* **283**, 185–192, DOI 10.1016/S0301-0104(02)00600-6 (Oct. 2002).
10. E. Hirota, Y. Kawashima, Internal Rotation of the Hydroxyl Group in Iso-propanol and the Chirality of the Gauche Form: Fourier Transform Microwave Spectroscopy of (CH₃)₂CHOD. en, *Journal of Molecular Spectroscopy* **207**, 243–253, DOI 10.1006/jmsp.2001.8352 (June 2001).

11. A. Shahi, E. Arunan, Microwave spectroscopic and theoretical investigations of the strongly hydrogen bonded hexafluoroisopropanolwater complex. en, *Phys. Chem. Chem. Phys.* **17**, 24774–24782, DOI 10.1039/C5CP03585F (2015).
12. I. A. Finneran, D. B. Holland, P. B. Carroll, G. A. Blake, A direct digital synthesis chirped pulse Fourier transform microwave spectrometer. en, *Review of Scientific Instruments* **84**, 083104, DOI 10.1063/1.4818137 (Aug. 2013).
13. W. Caminati *et al.*, Molecular beam Fourier transform microwave spectrum of the dimethylether–xenon complex: tunnelling splitting and ¹³¹Xe quadrupole coupling constants. en, *Chemical Physics Letters* **392**, 1–6, DOI 10.1016/j.cplett.2004.05.038 (July 2004).
14. T. J. Balle, W. H. Flygare, Fabry–Perot cavity pulsed Fourier transform microwave spectrometer with a pulsed nozzle particle source. en, *Review of Scientific Instruments* **52**, 33–45, DOI 10.1063/1.1136443 (Jan. 1981).
15. J. Grabow, W. Stahl, H. Dreizler, A multioctave coaxially oriented beam-resonator arrangement Fourier-transform microwave spectrometer. en, *Review of Scientific Instruments* **67**, 4072–4084, DOI 10.1063/1.1147553 (Dec. 1996).
16. M. Frisch, G. W. Trucks, Gaussian 09, revision A.02. *Gaussian 09, Revision A.02*, ISBN: 9781935522027 tex.referencecetype: generic (2009).
17. H. M. Pickett, The fitting and prediction of vibration-rotation spectra with spin interactions. en, *Journal of Molecular Spectroscopy* **148**, 371–377, DOI 10.1016/0022-2852(91)90393-0 (Aug. 1991).
18. J. K. Watson, Vibrational spectra and structure. Publisher: Elsevier: Amsterdam (1977).
19. R. Meyer, Flexible models for intramolecular motion, a versatile treatment and its application to glyoxal. en, *Journal of Molecular Spectroscopy* **76**, 266–300, DOI 10.1016/0022-2852(79)90230-3 (June 1979).
20. R. Meyer, W. Caminati, Quartic centrifugal distortion constants derived from a flexible model for 3-methylthietan. en, *Journal of Molecular Spectroscopy* **150**, 229–237, DOI 10.1016/0022-2852(91)90206-P (Nov. 1991).
21. R. S. Ruoff, T. D. Klots, T. Emilsson, H. S. Gutowsky, Relaxation of conformers and isomers in seeded supersonic jets of inert gases. en, *The Journal of Chemical Physics* **93**, 3142–3150, DOI 10.1063/1.458848 (Sept. 1990).
22. J. Kraitchman, Determination of Molecular Structure from Microwave Spectroscopic Data. en, *American Journal of Physics* **21**, 17–24, DOI 10.1119/1.1933338 (Jan. 1953).

23. M. S. Snow, B. J. Howard, L. Evangelisti, W. Caminati, From Transient to Induced Permanent Chirality in 2-Propanol upon Dimerization: A Rotational Study. en, *J. Phys. Chem. A* **115**, 47–51, DOI 10.1021/jp1107944 (Jan. 2011).

*Chapter 3*IDENTIFICATION OF TWO CONFORMATIONALLY TRAPPED
N-PROPANOL-WATER DIMERS IN A SUPERSONIC
EXPANSION

Two conformers of the n-propanol-water dimer have been observed in a supersonic expansion using chirped pulse-Fourier transform microwave spectroscopy. Structural assignments reveal the n-propanol sub-unit is conformationally trapped, with its methyl group in *Gauche* and *Trans* orientations. Despite different carbon backbone conformations, both dimers display the same water-donor/alcohol-acceptor hydrogen bonding motif. This work builds upon other reported alcohol-water dimers and upon previous work detailing the trapping of small molecules into multiple structural minima in rare gas supersonic expansions.

This chapter has been reproduced with permission from:

G. J. Mead *et al.*, Identification of two conformationally trapped n -propanol-water dimers in a supersonic expansion. en, *Journal of Molecular Spectroscopy* **335**, 68–73, DOI 10.1016/j.jms.2017.03.008 (May 2017),

3.1 Introduction

Intermolecular hydrogen bond interactions are of great importance for many chemical and biochemical systems, and can exist in strong and weak forms based upon the atoms involved. Strong hydrogen bonds range from 4-40 kcal/mol, and typically occur between electronegative atoms such as oxygen or fluorine ($\text{O-H} \cdots \text{O}$, $\text{F-H} \cdots \text{O}$). These strong bonding interactions display a distinct orientational preference [2]. In contrast, weak hydrogen bonds (<4 kcal/mol) display less directional preference [3]. The potential combinations of bonding partners increase dramatically in the weak case, where a bonding interaction may exist between any group of atoms with the general relationship $\text{X-H}^{\delta+} \cdots \text{A}^{\delta-}$. Strong and weak hydrogen bonds can display a cooperative effect, where the strength of multiple linked hydrogen bonds is greater than an equal number of unlinked hydrogen bonds [2]. Alcohol-water dimers present a good opportunity for studying how various strong and weak hydrogen bonding interactions influence structural organization via this cooperative effect.

Microwave spectroscopy is capable of providing detailed structural information on molecular dimers and clusters produced through strong and weak hydrogen bonding [4]. Previous work on small alcohol-water dimers have included the methanol-water dimer, the ethanol-water dimer, and the *tert*-butanol-water dimer [5, 6, 7]. This paper's focus, n-propanol, has increased structural complexity due to an additional methyl group. By lengthening the carbon backbone of the alcohol, new potential sites for cooperative hydrogen bonding interactions with water are introduced. In addition, re-orientation of the methyl group is prevented by a large potential barrier, which traps multiple conformers in a supersonic expansion [8]. Therefore, in contrast to the previously studied alcohol-water dimers, multiple n-propanol-water dimers are possible in an argon expansion as a result of conformational trapping and subsequent aggregation. Ab initio modeling of alcohol-water clusters is a useful compliment to experimental rotational studies for producing accurate spectral predictions that guide fitting and analysis [9].

In this study, we observe two dimer species, corresponding to water aggregating with two n-propanol conformers trapped in local minima. Ab initio calculations and Kraitchman substitutions of water and alcohol hydroxyl protons indicate these conformers display the same cooperative hydrogen-bonding motif despite structural differences in the n-propanol sub-unit.

3.2 Experimental approach

All experimental data was recorded with the Caltech chirped pulse-Fourier transform microwave (CP-FTMW) spectrometer between 6–18 GHz. A previous publication [10] has described the experimental setup in detail, but specifics to this study will be briefly mentioned. The heterodimer was produced by flowing argon gas at 46 psi through a glass bubbler partially filled with n-propanol, and then into a reservoir nozzle filled with water. A cartridge heater warmed the reservoir nozzle to $\sim 40^\circ$ Celsius. Pulsing the valve at 10 Hz into a vacuum chamber at 10^{-5} Torr produced a supersonic expansion of the alcohol-water vapor. This expansion was polarized with a 1 μ s duration chirped pulse, which had been heterodyne up-converted with a local oscillator (LO) and amplified prior to broadcast with a waveguide horn into the chamber. The free induction decay (FID) of the molecular expansion was detected on a second waveguide horn, amplified with a low noise amplifier, heterodyne down-converted, amplified a second time and digitized on a 4 giga-sample/s analog-to-digital converter. Double resonance experiments were performed by combining a -10 dBm, 1 μ s single tone pulse with the chirp prior to amplification and broadcast. N-propanol (> 99.5% purity, Sigma Aldrich) and D₂O (99.9% purity, Cambridge Isotope Laboratories) were used without further purification.

Data were collected over 100 hours at 6 LO settings spanning 6–18 GHz. A Python script cycled the local oscillator through a series of LO settings covering 6–18 GHz, collecting data for 300 seconds at each setting. Spectral measurements were double side-band, spanning 4 GHz of bandwidth around each LO setting. Heterodyne down-conversion condensed the 4 GHz of bandwidth into 2 GHz of detection bandwidth, so care was taken to correctly identify upper and lower side-band molecular transitions after digitization. To this end, data were also collected at all LO+10 MHz frequencies. A Python script compared spectra taken at LO and LO+10 Mhz settings to distinguish between upper and lower side-band peaks. Fittings of the spectra were performed using the Watson-A Hamiltonian in SPFIT/SPCAT integrated into a Python graphical interface [11]. Kraitchman substitutions were calculated using the KRA program [12].

3.3 Ab initio calculations

Gaussian 09 was used to perform all ab initio calculations [13]. Structures were optimized with second-order Møller-Plesset (MP2) perturbation theory [14] and the augmented correlation consistent polarized Valence-only Triple-Zeta (aug-cc-pVTZ) basis set [15]. Harmonic frequency calculations were performed using the

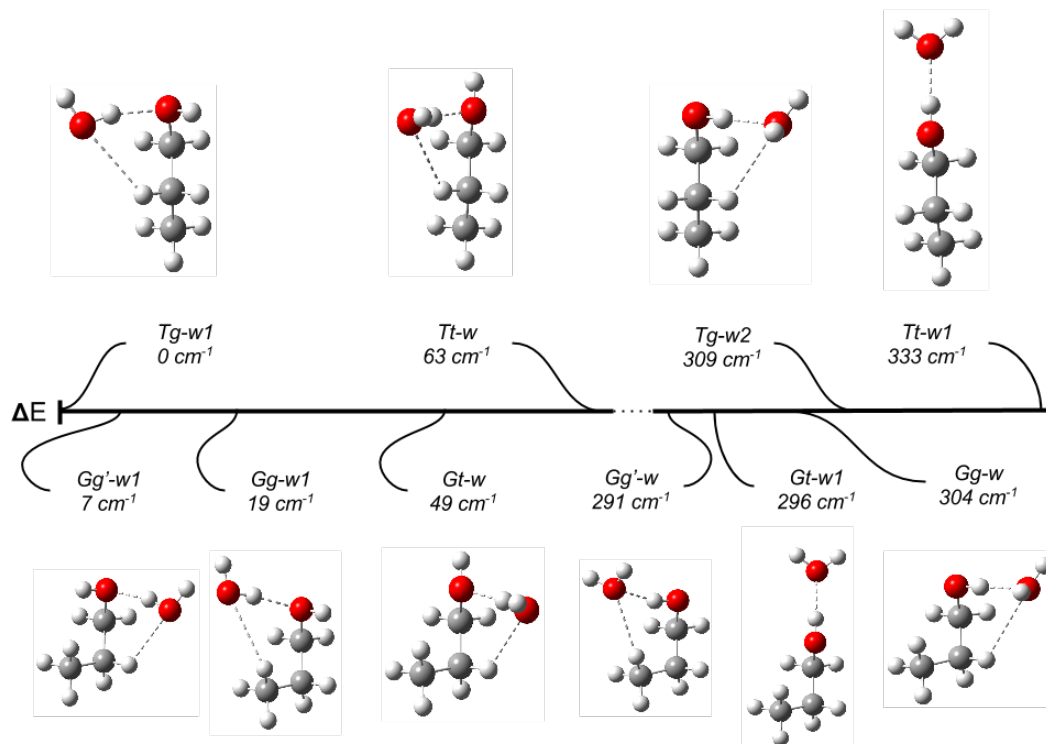


Figure 3.1: MP2/aug-cc-pVTZ optimized structures and CCSD(T)/aug-cc-pVTZ ZPVE-corrected relative energies of the ten n-propanol-water dimer conformers.

same level of theory as the optimization to verify structures were true potential energy surface minima. Single-point coupled cluster energy calculations with singles, doubles and perturbative triples (CCSD(T)) [16] using the aug-cc-pVTZ basis set were performed on the MP2/aug-cc-pVTZ optimized structures. This single point energy value was then added to the zero point vibrational energy (ZPVE) contribution calculated during the harmonic frequency calculations. Equilibrium rotational constants (B_e) were computed from the geometries optimized at MP2/aug-cc-pVTZ. Due to computational limitations, anharmonic calculations of ground state rotational constants (B_0) and quartic distortion constants were performed at MP2/6-311++G(d,p) [17].

3.4 Results: Ab initio structures

The structures and relative energies of the ten calculated n-propanol-water dimers are shown in Figure 3.1, with respective equilibrium rotational constants (B_e) listed in Table 3.1.

Structural calculations indicate two possible orientations of n-propanol's methyl

Table 3.1: Equilibrium MP2/aug-cc-pVTZ rotational constants, dipole moments, and zero-point corrected relative energies of the ten n-propanol-water dimer conformers. Water-donor structures make up the five lowest energy structures, while water-acceptor structures make up the five highest energy structures.

	<i>Tg-w1</i>	<i>Gg'-w1</i>	<i>Gg-w1</i>	<i>Gt-w</i>	<i>Tt-w</i>	<i>Gg'-w</i>	<i>Gt-w1</i>	<i>Gg-w</i>	<i>Tg-w2</i>	<i>Tt-w1</i>
A [MHz]	5697	5253	5132	4702	5860	5115	12180	5863	6439	15544
B [MHz]	2276	2505	2729	2900	2191	2702	1459	2078	1882	1302
C [MHz]	1773	2081	1969	2081	1737	1948	1389	1825	1558	1236
$ \mu_A $ [D]	1.11	1.61	2.03	1.73	0.82	2.12	2.88	2.49	2.09	2.66
$ \mu_B $ [D]	1.70	1.19	1.86	2.98	1.85	2.41	0.09	1.56	2.13	0.82
$ \mu_C $ [D]	0.40	0.63	0.57	0.39	0.20	0.47	0.40	0.70	0.16	0.01
ΔE [cm ⁻¹]	0	7	19	49	63	291	296	304	309	333

group relative to the C-O bond, which are labelled *Trans* (*T*) and *Gauche* (*G*). The position of the hydroxyl proton similarly has two general conformations, *trans* and *gauche*, although in the *G* conformation there are two non-identical hydroxyl positions, *g* and *g'*. Herein these five n-propanol conformers are labeled *Trans-trans*, *Trans-gauche*, *Gauche-trans*, *Gauche-gauche*, and *Gauche-gauche'*, following the same convention used for the n-propanol monomer [18].

We observe the water molecule occupying local conformational minima around the *T* and *G* structures, acting as a proton donor for the five lowest energy structures. Ab initio calculations indicate a clear preference for water donor conformers, in agreement with prior work on other water-alcohol dimers [5, 6, 7]. This preference may be due to the optimized electron delocalization possible when the water donates a proton to the alcohol, producing a strong hydrogen bond [2]. Secondary effects, such as weak hydrogen bonding between an alkyl proton and the water oxygen, can provide a further stabilizing interaction in water donor structures. Indeed, cooperative hydrogen bonding interactions are present in all five water-donor structures. Calculations suggest an immediate ~ 230 cm⁻¹ increase in relative energy between the highest energy water-donor structure, *Tt-w*, and the lowest energy water-acceptor structure, *Gg'-w*. Water-acceptor structures are believed to be energetically unfavorable due to anti-cooperative arrangements of strong and weak hydrogen bonding interactions (*Gg-w*, *Tg-w2*, and *Gg'-w*) and/or extremely elongated, singly bound structures (*Gt-w1*, *Tt-w1*).

Ab initio results suggest *Tg-w1* is the ground state conformer. However, given previous work on conformational trapping of the n-propanol monomer [8], it is plausible we may observe two distinct n-propanol-water dimer structures. Therefore, the lowest energy conformer not within the *T* family, *Gg'-w1*, is also likely to be

observed experimentally.

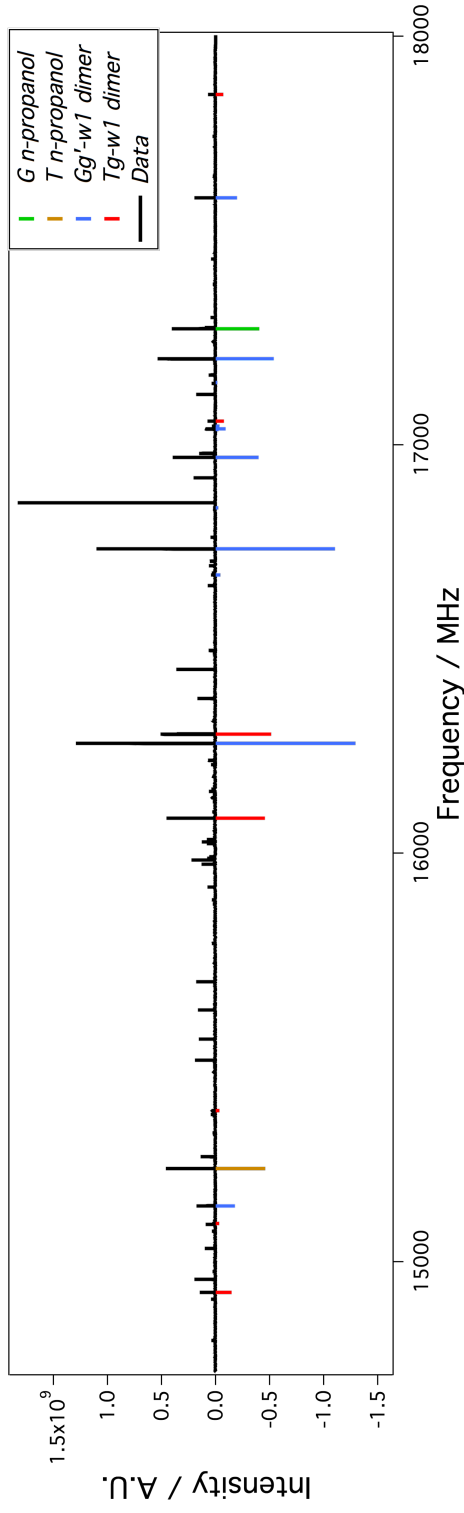
3.5 Results: Observation of $Gg'-w1$ and $Tg-w1$ conformers

A portion of the raw data from 15–18 GHz can be seen in Figure 3.2 A, with Tt and Gt n-propanol monomers and two n-propanol-water dimers identified. Raw data from the spectrometer was analyzed as follows. To remove the strongest water dimer, n-propanol monomer and n-propanol homodimer transitions, separate sets of data were collected with only water and only n-propanol present in an argon expansion under identical experimental conditions. Subtraction of these peaks using a Python script produced a residual spectrum with moderately strong unidentified peaks. Analysis proceeded under the assumption that the n-propanol-water dimer transitions were responsible for many of the unidentified peaks in the residual spectrum.

Two normal-species conformers were fit from the residual spectrum, accounting for almost every single strong transition from 6–18 GHz (Figure 3.2 B). Given the length of data collection, the weaker remaining transitions may be attributable to various molecular trimers. Experimental and predicted rotational constants for the two conformers are found in Table 3.2. Expansion in HOD and D₂O allowed for the assignment of seven deuterated isotopologues. Double resonance of A-type/B-type transition pairs verified all nine fits. Substitution coordinates were calculated using the KRA program [12] and compared to ab initio normal species coordinates (Table 3.3). Kraitchman substitutions are shown in Figure 3.3. Caveats with Kraitchman substitution include potentially unreliable calculation results when the isotopic change occurs near a principle axis origin [20]. Deuteration also slightly alters the hydrogen bond distance, changing the proton coordinate (the Ubbelohde effect) [7, 21]. Even so, Kraitchman substitutions were sufficient to assign one conformer unequivocally as $Tg-w1$.

Assigning the second conformer as $Gg'-w1$ or $Gg-w1$ was less definitive with substitution coordinates alone. Comparison of experimental to MP2/6-311++G(d,p) rotational constants revealed a maximum difference of 5% for $Gg'-w1$ and a maximum difference of 11% for $Gg-w1$. In conjunction with a lower ab initio energy for $Gg'-w1$, we assigned the second conformer as $Gg'-w1$. Both assigned conformers have experimental B constants that differ substantially from predicted B_e and B_0 constants. The percent difference between experiment and harmonic MP2/aug-cc-pVTZ predictions are up to twice that of experiment compared to anharmonic MP2/6-311++G(d,p) predictions. Previously reported clusters have already identi-

A



B

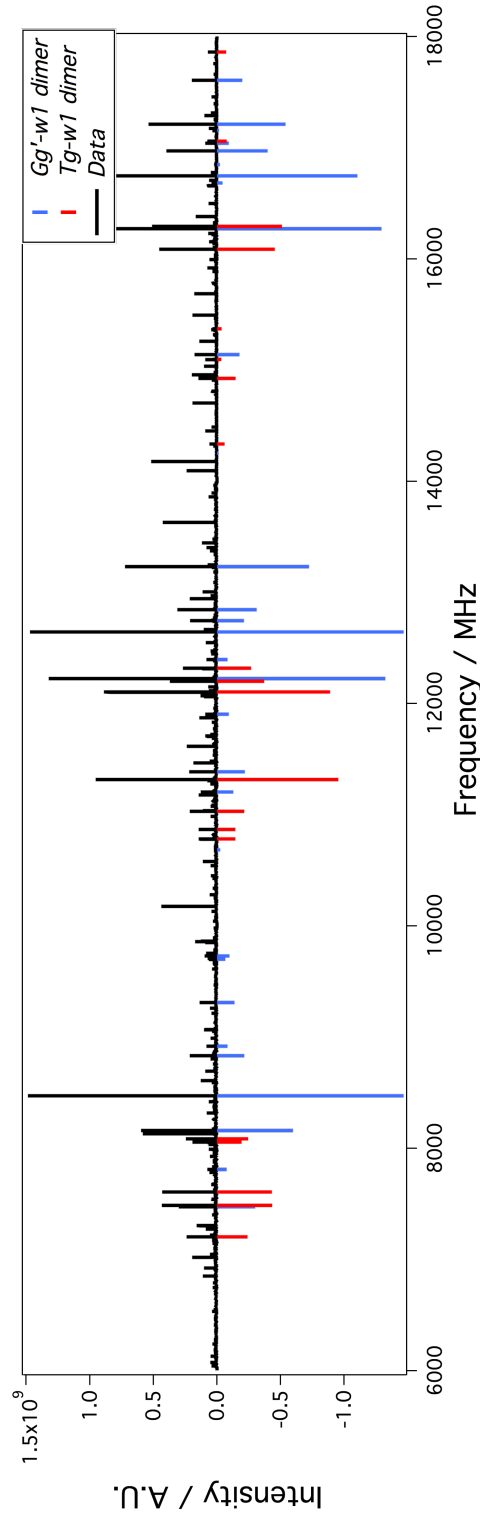


Figure 3.2: A) A sub-section from the full data set (100 hour acquisition time, 42 million averages at 6 LO settings). Plotted as stick spectra are transitions from the *Tt* *n*-propanol monomer [19], *Gt* *n*-propanol monomer [18], and the *Gg'*-*w1* and *Tg*-*w1* dimers. B) Stick spectra from 6–18 GHz of the normal species *Gg'*-*w1* and *Tg*-*w1* transitions observed in a supersonic expansion of *n*-propanol with water. Line centers are accurate to a microwave rms of ~20 kHz. Double resonance experiments confirmed all normal and deuterated species fits. Monomer and homodimer transitions have been subtracted.

fied the importance of vibrational corrections to rotational constants [6, 22].

Transitions from two predicted low energy n-propanol-water conformers, *Gt-w*, and *Tt-w* were not observed in the data. In the case of these conformers, cooling to *Gg'-wl* and *Tg-wl* may be readily achieved through small movements of the alcohol and the free water protons. A similar effect was observed in the ethanol-water dimer, where *trans*-ethanol monomer relaxes into a *gauche* conformation upon aggregating with water [6]. Studies of the ethanol-ethanol homodimer also find a preference for a *gauche*-ethanol proton acceptor structure [23, 24].

Also of note is that while the $Gg'-wl$ and $Gg-wl$ dimers are within 12 cm^{-1} in energy, dimerization with water appears to result exclusively in the $Gg'-wl$ conformer. This is despite the fact that water encountering Gt n-propanol in the gas phase could (in theory) produce roughly equivalent populations of $Gg'-wl$ and $Gg-wl$. Rearrangements of the $Gg-wl$ alcohol and free water protons into the $Gg'-wl$ structure seem unlikely to occur, given the concomitant long migration of the water molecule to achieve the $Gg'-wl$ structure. A plausible argument suggests

Table 3.2: Ab initio MP2/aug-cc-pVTZ equilibrium rotation constants, MP2/6-311++G(d,p) ground state rotational and quartic distortion constants, and experimental rotational and distortion constants for normal and deuterated $Gg'-wI$ and $Tg-wI$ conformers. Asterisks indicate the normal species value was used, while standard errors appear in parentheses.

$Gg'-wI$	aug-cc-pVTZ	6-311++G(d,p)	nPropOH:H ₂ O	nPropOH:DOH	nPropOD:DOH	nPropOH:D ₂ O	nPropOD:D ₂ O
A [MHz]	5253	5310	5517.1047(45)	5511.3493(85)	5323.069(53)	5480.054(38)	5287.55(14)
B [MHz]	2505	2419	2291.9966(53)	2259.7031(35)	2283.8315(99)	2163.8641(99)	2157.528(18)
C [MHz]	2081	2030	1955.4564(51)	1932.1810(32)	1951.4702(99)	1858.3159(96)	1855.129(15)
Δ_J [MHz]		0.01249	0.017493(51)	0.01663(10)	0.01708(29)	0.01476(30)	0.01454(51)
Δ_{JK} [MHz]		-0.05996	-0.08637(19)	-0.08293(28)	-0.07932(72)	-0.0725(15)	-0.0646(32)
Δ_K [MHz]		0.13826	0.29850(25)	*	0.237(13)	*	0.461(23)
δ_J [MHz]		0.00404	0.006003(37)	*	*	*	*
δ_K [MHz]		0.01007	0.0150(10)	*	*	*	*
N lines			33	20	19	15	10
RMS [kHz]			9	18	46	42	45
$Tg-wI$	aug-cc-pVTZ	6-311++G(d,p)	nPropOH:H ₂ O	nPropOH:DOH	nPropOD:DOH	nPropOH:D ₂ O	nPropOD:D ₂ O
A [MHz]	5697	5856	5795.8587(38)	5808.9003(72)	5560.774(38)	5727.787(12)	
B [MHz]	2276	2157	2131.5063(16)	2095.0489(29)	2086.4310(74)	2013.9058(52)	
C [MHz]	1773	1719	1689.9550(15)	1667.9292(21)	1650.3481(87)	1611.2293(48)	
Δ_J [MHz]		0.00274	0.008674(20)	*	0.00828(19)	0.00780(11)	
Δ_{JK} [MHz]		0.12134	-0.053290(74)	*	*	*	
Δ_K [MHz]		0.04714	0.14216(80)	*	*	*	
δ_J [MHz]		-0.00047	0.0027569(97)	*	*	*	
δ_K [MHz]		0.02816	0.00788(57)	*	*	*	
N lines			28	22	15	15	
RMS [kHz]			5	32	47	34	

Table 3.3: MP2/aug-cc-pVTZ predicted normal species and experimentally derived principle axis coordinates for the three isotopically interchangeable protons. †Indicates predicted value was used for plotting in Figure 3.3.

	Prediction				Experiment		
$Gg'-wl$	H_F	H_B	H_A		H_F	H_B	H_A
A	-3.247	-1.794	0.073	A	3.148	1.761	2* i^\dagger
B	-0.482	-0.031	0.988	B	0.741	0.172	1.185
C	-0.054	-0.225	-1.365	C	0.132	0.262	1.330
$Tg-wl$	H_F	H_B	H_A		H_F	H_B	H_A
A	-3.145	-1.946	-0.674	A	3.092	2.041	0.410
B	-1.062	-0.206	1.683	B	1.076	0.4* i^\dagger	1.743
C	-0.377	0.039	0.987	C	0.393	0.09* i^\dagger	0.934

Table 3.4: Comparison of predicted strong and weak hydrogen bond distances and angles for $Tg-wl$, $Gg'-wl$, and $Gg-wl$. Also listed are values for the g -ethanol-water dimer structure from [6].

MP2/aug-cc-pVTZ	$Tg-wl$	$Gg'-wl$	$Gg-wl$	g -EW
r (O-H \cdots O) [\AA]	1.88	1.88	1.87	1.88
θ (O-H \cdots O) [$^\circ$]	162.1	165.2	168.8	162.6
r (C-H \cdots O) [\AA]	2.65	2.62	2.80	2.66
θ (C-H \cdots O) [$^\circ$]	128.4	129.3	116.4	127.1

hydrogen bonding from the water oxygen to a methyl (β -carbon) proton (as in $Gg-wl$) is less stabilizing than hydrogen bonding to an α -carbon proton (as in $Gg'-wl$). This effect is difficult to attribute to relative pKas of various alkyl protons, since accurately extrapolating from solvent acidity to gas-phase acidity is quite difficult [25]. Instead, the effect may be largely geometric. Table 3.4 lists calculated bond distances and angles of the strong and weak hydrogen bonds in the $Tg-wl$, $Gg'-wl$, and $Gg-wl$ conformers. Dimensions from the g -ethanol-water dimer are also included for comparison [6]. Characteristics of the strong hydrogen bond between water and the alcohol -OH moiety are remarkably conserved in all four structures. Similarly, the weak hydrogen bond parameters for $Tg-wl$, $Gg'-wl$, and g -EW are nearly identical. However, $Gg-wl$ has both an increased C-H \cdots O bonding distance (+0.2 \AA , 2.80 \AA) and a decreased C-H \cdots O bonding angle (-13° , 116.4 $^\circ$), each of which contribute to a weaker CH \cdots O bond by reducing overlap with the oxygen lone pair electrons [2]. From these results, it appears that a weak hydrogen bond interaction between the Gt alcohol monomer and water has a decisive influence on the resulting dimer's structural conformation.

3.6 Conclusion

We report two n-propanol-water dimers in a supersonic expansion with argon. Trapping of n-propanol provides two distinct conformers for aggregation with water molecules. Isotopic substitution has definitively assigned these two dimers as *Tg-wI* and *Gg'-wI*. Both conformers are the ground state structures within their respective n-propanol conformational group, *T* or *G*. Ab initio calculations similarly predicted *Tg-wI* and *Gg'-wI* as the two ground state conformers. The hydrogen bonding network of strong and weak interactions does not change between the two n-propanol structures. Instead, a conserved pattern of a strong O-H \cdots O bond stabilized by a weak C $_{\alpha}$ -H \cdots O interaction is observed.

Broadly, this work builds upon a trend of water-donor, alcohol-acceptor clusters studied in the gas-phase using rotational spectroscopy. N-propanol, in comparison to methanol/ethanol/*t*-butanol, presents the most conformationally varied alcohol studied in a dimer complex with water up to this point. Utilizing the useful property of conformational trapping in rare-gas expansions will aid future studies of more conformationally diverse alcohol-water clusters.

BIBLIOGRAPHY

1. G. J. Mead, E. R. Alonso, I. A. Finneran, P. B. Carroll, G. A. Blake, Identification of two conformationally trapped n -propanol-water dimers in a supersonic expansion. en, *Journal of Molecular Spectroscopy* **335**, 68–73, DOI 10.1016/j.jms.2017.03.008 (May 2017),
2. G. R. Desiraju, T. Steiner, *The weak hydrogen bond: in structural chemistry and biology*, eng, OCLC: 246186951 (Oxford Univ. Pr, Oxford, 1999).
3. T. Steiner, G. R. Desiraju, Distinction between the weak hydrogen bond and the van der Waals interaction. *Chem. Commun.*, 891–892, DOI 10.1039/a708099i (1998).
4. K. R. Leopold, G. T. Fraser, S. E. Novick, W. Klemperer, Current Themes in Microwave and Infrared Spectroscopy of Weakly Bound Complexes. en, *Chem. Rev.* **94**, 1807–1827, DOI 10.1021/cr00031a004 (Nov. 1994).
5. P. A. Stockman, G. A. Blake, F. J. Lovas, R. D. Suenram, Microwave rotation-tunneling spectroscopy of the water–methanol dimer: Direct structural proof for the strongest bound conformation. en, *The Journal of Chemical Physics* **107**, 3782–3790, DOI 10.1063/1.474736 (Sept. 1997).
6. I. A. Finneran, P. B. Carroll, M. A. Allodi, G. A. Blake, Hydrogen bonding in the ethanol–water dimer. en, *Phys. Chem. Chem. Phys.* **17**, 24210–24214, DOI 10.1039/C5CP03589A (2015).
7. L. Evangelisti, W. Caminati, Internal dynamics in complexes of water with organic molecules. Details of the internal motions in tert-butylalcohol–water. en, *Phys. Chem. Chem. Phys.* **12**, 14433, DOI 10.1039/c0cp01195a (2010).
8. R. S. Ruoff, T. D. Klots, T. Emilsson, H. S. Gutowsky, Relaxation of conformers and isomers in seeded supersonic jets of inert gases. en, *The Journal of Chemical Physics* **93**, 3142–3150, DOI 10.1063/1.458848 (Sept. 1990).
9. E. E. Fileti, P. Chaudhuri, S. Canuto, Relative strength of hydrogen bond interaction in alcohol–water complexes. en, *Chemical Physics Letters* **400**, 494–499, DOI 10.1016/j.cplett.2004.10.149 (Dec. 2004).
10. I. A. Finneran, D. B. Holland, P. B. Carroll, G. A. Blake, A direct digital synthesis chirped pulse Fourier transform microwave spectrometer. en, *Review of Scientific Instruments* **84**, 083104, DOI 10.1063/1.4818137 (Aug. 2013).
11. H. M. Pickett, The fitting and prediction of vibration-rotation spectra with spin interactions. en, *Journal of Molecular Spectroscopy* **148**, 371–377, DOI 10.1016/0022-2852(91)90393-0 (Aug. 1991).
12. Z. Kisiel, English. In *Spectroscopy from Space*, ed. by J. Demaison, K. Sarka, E. A. Cohen, OCLC: 840307733 (Springer Netherlands : Imprint : Springer, Dordrecht, 2001), pp. 91–106.

13. M. Frisch, G. W. Trucks, Gaussian 09, revision A.02. *Gaussian 09, Revision A.02*, ISBN: 9781935522027 tex.referencetype: generic (2009).
14. C. Møller, M. S. Plesset, Note on an Approximation Treatment for Many-Electron Systems. en, *Phys. Rev.* **46**, 618–622, DOI 10.1103/PhysRev.46.618 (Oct. 1934).
15. R. A. Kendall, T. H. Dunning, R. J. Harrison, Electron affinities of the first-row atoms revisited. Systematic basis sets and wave functions. en, *The Journal of Chemical Physics* **96**, 6796–6806, DOI 10.1063/1.462569 (May 1992).
16. J. A. Pople, M. Head-Gordon, K. Raghavachari, Quadratic configuration interaction. A general technique for determining electron correlation energies. en, *The Journal of Chemical Physics* **87**, 5968–5975, DOI 10.1063/1.453520 (Nov. 1987).
17. R. Krishnan, J. S. Binkley, R. Seeger, J. A. Pople, Self-consistent molecular orbital methods. XX. A basis set for correlated wave functions. en, *The Journal of Chemical Physics* **72**, 650–654, DOI 10.1063/1.438955 (Jan. 1980).
18. Z. Kisiel *et al.*, Determination of precise relative energies of conformers of n-propanol by rotational spectroscopy. en, *Phys. Chem. Chem. Phys.* **12**, 8329, DOI 10.1039/c002156c (2010).
19. H. Dreizier, F. Scappini, Centrifugal Distortion and Internal Rotation Analysis in the Ground State of Trans N-Propanol. *Zeitschrift für Naturforschung A* **36**, 1187–1191, DOI 10.1515/zna-1981-1109 (Nov. 1981).
20. L. Pierce, Note on the use of ground-state rotational constants in the determination of molecular structures. en, *Journal of Molecular Spectroscopy* **3**, 575–580, DOI 10.1016/0022-2852(59)90049-9 (Jan. 1959).
21. S. Tang, I. Majerz, W. Caminati, Sizing the Ubbelohde effect: the rotational spectrum of a tert-butylalcohol dimer. en, *Phys. Chem. Chem. Phys.* **13**, 9137, DOI 10.1039/c1cp20210c (2011).
22. C. Perez *et al.*, Structures of Cage, Prism, and Book Isomers of Water Hexamer from Broadband Rotational Spectroscopy. en, *Science* **336**, 897–901, DOI 10.1126/science.1220574 (May 2012).
23. J. P. I. Hearn, R. V. Cobley, B. J. Howard, High-resolution spectroscopy of induced chiral dimers: A study of the dimers of ethanol by Fourier transform microwave spectroscopy. en, *The Journal of Chemical Physics* **123**, 134324, DOI 10.1063/1.2049267 (Oct. 2005).
24. I. A. Finneran, P. B. Carroll, G. J. Mead, G. A. Blake, Hydrogen bond competition in the ethanol–methanol dimer. en, *Phys. Chem. Chem. Phys.* **18**, 22565–22572, DOI 10.1039/C6CP03980D (2016).
25. D. K. Bohme, E. Lee-Ruff, L. B. Young, Standard acidity scale. The pK_a of alcohols in the gas phase. en, *J. Am. Chem. Soc.* **93**, 4608–4609, DOI 10.1021/ja00747a054 (Sept. 1971).

Part III

Terahertz Spectroscopy

Chapter 4

FUNDAMENTALS OF NONLINEAR TERAHERTZ KERR EFFECT SPECTROSCOPY

In this chapter, we introduce the theory underlying nonlinear terahertz Kerr effect spectroscopies and discuss the experimental techniques used throughout this section of the thesis.

4.1 Theory

Much of this theory discussion follows results from an excellent paper on correlation functions in third-order spectroscopy [1]. In all spectroscopies, the n^{th} -order optically induced polarization of the sample is given by the product of the n^{th} -order susceptibility $\chi^{(n)}$ and n electric field terms E_ζ , where the Greek subscript denotes the electric field's polarization in the lab frame.

$$P_\eta = \chi_{\eta\alpha}^{(1)} E_\alpha + \chi_{\eta\beta\alpha}^{(2)} E_\beta E_\alpha + \chi_{\eta\gamma\beta\alpha}^{(3)} E_\gamma E_\beta E_\alpha + \dots \quad (4.1)$$

Equation 4.1 can be applied to understand all spectroscopic measurements. For example, in the case of a linear absorption measurement, the leading order term is $P_\eta = \chi_{\eta\alpha}^{(1)} E_\alpha$. Nonlinear spectroscopies rely on higher order terms. In an isotropic media, such as a liquid, the first non-zero higher order term is $\chi_{\eta\gamma\beta\alpha}^{(3)} E_\gamma E_\beta E_\alpha$, which indicates that all third-order spectroscopies depend upon some combination of three electric field interactions to produce an electronic polarization in a sample. The magnitude and characteristics of this polarization will be dependent upon the $\chi_{\eta\gamma\beta\alpha}^{(3)}$ response of the sample, as well as the particular experimental technique.

Nonlinear terahertz spectroscopy is performed using time-domain measurements, so it is logical to transform the frequency-domain $\chi_{\eta\gamma\beta\alpha}^{(3)}$ susceptibility into a time-domain material response function $\mathbf{R}_{\eta\gamma\beta\alpha}^{(3)}(t_3, t_2, t_1)$.

$$\begin{aligned}
\mathbf{R}_{\eta\gamma\beta\alpha}^{(3)}(t_3, t_2, t_1) = & \frac{1}{8\pi^3} \int_0^\infty d\omega_3 \int_0^\infty d\omega_2 \int_0^\infty d\omega_1 \chi_{\eta\gamma\beta\alpha}^{(3)} \\
& \times \exp(-i(\omega_3 + \omega_2 + \omega_1)t_3) \\
& \times \exp(-i(\omega_2 + \omega_1)t_2) \\
& \times \exp(-i(\omega_1)t_1)
\end{aligned} \tag{4.2}$$

In general, a time varying third-order nonlinear signal can then be written as:

$$\begin{aligned}
P_\eta^{(3)}(k, t) = & (-i^3) \int_0^\infty dt_3 \int_0^\infty dt_2 \int_0^\infty dt_1 \mathbf{R}_{\eta\gamma\beta\alpha}^{(3)}(t_3, t_2, t_1) \\
& \times \exp(-i(\omega_3 + \omega_2 + \omega_1)t_3) \\
& \times \exp(-i(\omega_2 + \omega_1)t_2) \\
& \times \exp(-i(\omega_1)t_1) E_{3\gamma}(t - t_3) E_{2\beta}(t - t_2) E_{1\alpha}(t - t_1)
\end{aligned} \tag{4.3}$$

Kerr effect spectroscopy is a special subset of third-order nonlinear spectroscopy. Unlike, for example, the highly directional emission from a phase-matched third-order coherent Anti-stokes Raman scattering (box-CARS) spectroscopy, Kerr effect spectroscopy measures an intrinsically bulk effect. Irradiation of a region of a sample with an intense electric field results in a detectable change in the sample's indices of refraction. Because the key observable in Kerr effect spectroscopy is this induced birefringence, polarimetric detection techniques are commonly employed, including in this thesis. A second characteristic of Kerr effect spectroscopy is the ubiquity of the effect irrespective of pump frequency. Both optical and THz radiation can induce birefringence responses in the same sample, albeit through slightly different mechanisms [2]. In this thesis, we will demonstrate three different kinds of Kerr effect experiments: 1D optical (1D-OKE), 1D THz (1D-TKE), and 2D THz (2D-TTR).

Correlation functions

Changes in a sample's Kerr effect response are observed in the time-domain by altering the time between the intense pump field, $E_{\text{pump}}E_{\text{pump}}^*$, and the weaker probe field, E_{probe} (Fig. 4.1). In 1D optical and THz Kerr effect experiments, the two pump fields interact simultaneously in the sample so that $t_1 = t_3 = 0$ in Eq. 4.3. The orientational component of the material response function can be compactly written [3] as a time-dependent correlation function dependent upon the sample's

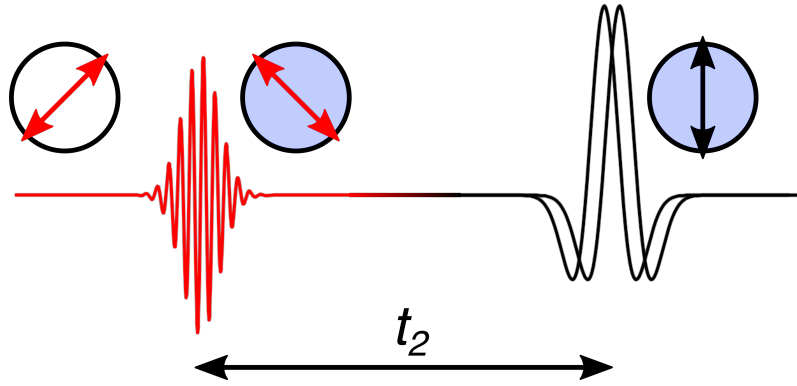


Figure 4.1: 1D-TKE experimental electric field polarizations and time definitions. Two simultaneous THz pump field interactions (Y polarized) generate a birefringence in a sample that is probed at time t_2 with a $(X + Y)$ polarized optical field. A Raman signal is generated with $(X - Y)$ polarization.

Raman polarizability tensor, Π . (Note the symbol α is more commonly used to represent this tensor, but we will use Π herein for consistency with other 2D-TTR literature [4] and to avoid confusion with the Greek subscript α used to denote field polarization.)

$$R_{\eta\gamma\beta\alpha}^{\Pi}(t_2) = \langle \Pi_{\eta\gamma}(t_2) \Pi_{\beta\alpha}(0) \rangle \quad (4.4)$$

When applied to room-temperature liquid samples, the 1D-OKE and 1D-TKE responses are sensitive to the low-frequency, thermally populated continuum of states within the liquid [5, 6]. Both the non-resonant, high photon energy optical pump and the low photon energy THz pump fields interact with the sample via the $\Pi_{\beta\alpha}(0)$ Raman tensor element.

In contrast, a third-order signal arising from resonant dipole interactions, M , would be described as a four-time correlation function. (Again, note the symbol μ is more commonly used to represent this tensor, but we will use M herein for consistency with other 2D-TTR literature [4].)

$$R_{\eta\gamma\beta\alpha}^M(t_3, t_2, t_1) = \langle M_{\eta}(t_3 + t_2 + t_1) M_{\gamma}(t_2 + t_1) M_{\beta}(t_1) M_{\alpha}(0) \rangle \quad (4.5)$$

From Eqs. 4.4 and 4.5, it was reasonably hypothesized [7] that the hybrid 2D-TTR signal obeyed a three-time correlation function, shown in Eq. 4.6. It will be shown

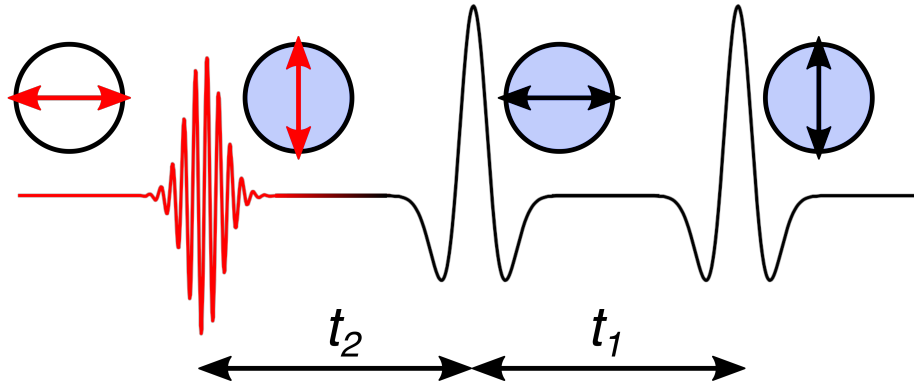


Figure 4.2: 2D-TTR experimental electric field polarizations and time definitions. Two THz pump field interactions (Y and X polarized) separated by a time t_1 generates a birefringence in a sample that is probed at time t_2 with a (Y) polarized optical field. A Raman signal is generated with (X) polarization. Note that a correction factor (“deskewing”) must be applied to t_2 when $t_1 < 0$ [4].

in later sections that 2D-TTR is, in some cases, actually better described by Eq. 4.4.

$$R_{\eta\gamma\beta\alpha}^{\text{TTR}}(t_2, t_1) = \langle \Pi_{\eta\gamma}(t_2 + t_1) M_\beta(t_1) M_\alpha(0) \rangle \quad (4.6)$$

Polarization of the experimental electric fields

From the current overview, we can see that a Kerr effect signal reflects a multi-time correlation function involving the sample’s polarizability and dipole operators. We have neglected thus far to examine the important role that the polarization of the electric fields have in determining which component of the correlation function is observed. If we define the electric field polarizations in the lab frame, where X and Y are orthogonal to the optical axis of propagation Z, there are four non-equivalent polarizations components in the material response function. If the first electric field polarization is fixed along X ($\psi_1 = 0^\circ$), the four components may be written as:

$$\begin{aligned} P^{(3)} = & R_{XXXX} \cos(\psi_4) \cos(\psi_3) \cos(\psi_2) \\ & + R_{XYYX} \cos(\psi_4) \sin(\psi_3) \sin(\psi_2) \\ & + R_{YYXX} \sin(\psi_4) \sin(\psi_3) \cos(\psi_2) \\ & + R_{YXYX} \sin(\psi_4) \cos(\psi_3) \sin(\psi_2) \end{aligned} \quad (4.7)$$

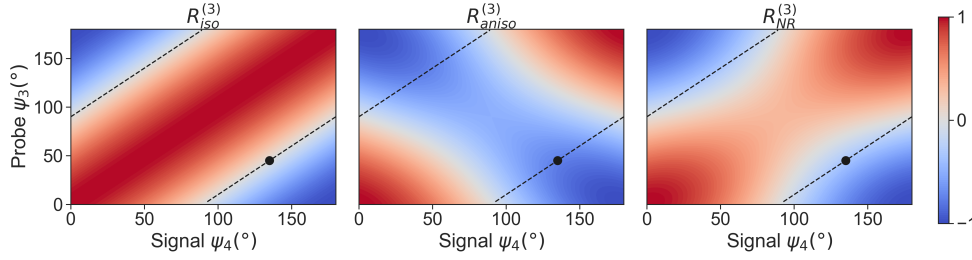


Figure 4.3: In the case where $\psi_2 = \psi_1 = 0^\circ$ (1D-TKE and 1D-OKE), the isotropic response is completely suppressed for $\psi_3 \perp \psi_4$ (black dashed line). The anisotropic response is maximized under these same polarization conditions if the probe polarization is oriented at 45° to the pump fields. Unless otherwise noted, the black dot marks the polarization condition used for 1D-TKE experiments in this thesis.

These four components of the third-order response function, $R^{(3)}$, contribute in varying proportions to the non-resonant ($R_{NR}^{(3)}$), the isotropic ($R_{iso}^{(3)}$), and the anisotropic ($R_{aniso}^{(3)}$) components of $R^{(3)}$. The relationships between the four field polarizations and their individual contributions to the three components of $R^{(3)}$ are perhaps most easily understood visually. In Figs. 4.3 (proportional to 1D-TKE) and 4.4 (proportional to 2D-TTR), the distribution of non-resonant, isotropic, and anisotropic components are shown as a function of the probe (ψ_3) and signal (ψ_4) polarizations. Either one or all three $R^{(3)}$ components may be eliminated through the choice of experimental polarizations.

Black dashed lines trace the case where $\psi_3 \perp \psi_4$, which is the case for all experiments described herein. (This choice of polarization is for a number of pragmatic reasons. First, crossed polarizations reduces background photon noise, increasing the achievable experimental signal-to-noise. Second, the photo-detectors have a limited dynamic range which favors limiting the background light to a level just sufficient for heterodyne detection on the detector.)

Pump photon energy

It is worth first noting that the several orders of magnitude difference in pump photon energies in 1D-OKE vs. 1D-TKE experiments has implications for the mechanistic description of the pump interaction step [2]. Optical Kerr effect pump excitation proceeds through a Raman scattering pathway, where $\omega_{\text{pump}}^A - \omega_{\text{pump}}^B \approx \omega_\nu$, where ω_ν can be a low frequency intermolecular bath mode. In this case, the torque applied by the pump field is described in the literature as a interacting via a dipole-

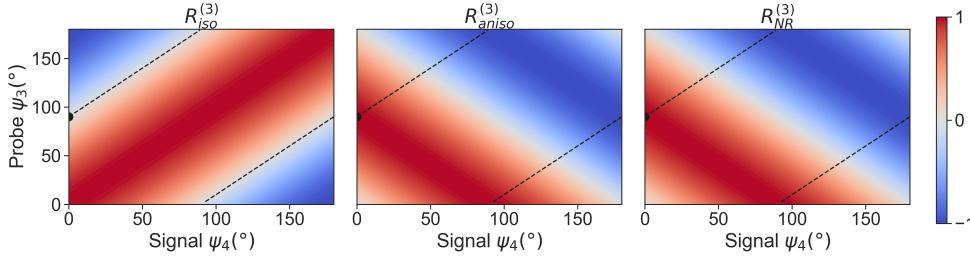


Figure 4.4: In the case where $\psi_2 \perp \psi_1$ (2D-TTR), the isotropic response is fully suppressed for all orthogonal probe/signal polarizations. In contrast to 1D-TKE, the anisotropic response is maximized if $\psi_3 \parallel \psi_1$ and $\psi_4 \parallel \psi_2$. Unless otherwise noted, the black dot marks the polarization condition used for 2D-TTR experiments in this thesis.

induced dipole mechanism. In contrast, the direct THz pump excitation, where $\omega_{\text{pump}}^A + \omega_{\text{pump}}^B \approx \omega_\nu$ proceeds through a dipole-dipole interaction.

Apart from diffuse intermolecular modes which give rise to the orientational response in liquids at room temperature, much of later works described in this thesis will be more focused on excitations of intramolecular vibrational mode. 1D-OKE excites these vibrations via a Raman scattering process. As has been recently reported in a theory paper from 2019 [8], the direct analog of this process with THz pump excitation is $\omega_{\text{pump}}^A + \omega_{\text{pump}}^B \approx \omega_\nu$, where the THz pumps interact in a sum-frequency manner with the sample. Experimental evidence of a THz sum-frequency process was actually reported a few years earlier [9, 10], where a 40 THz phonon mode in diamond was found to be selectively excited under intense THz pumping at $\omega = 20$ THz. A similar sum-frequency excitation mechanism for intramolecular vibrational modes observed in 1D-TKE measurements of halogenated methane liquids was proposed in 2015 [11].

4.2 Experimental technique

A consolidated overview of the optical layouts used for nonlinear Kerr effect experiments is shown in. Fig. 4.5. An excellent review of the 1D-OKE technique and theory can be found in [5]. The THz equivalent, first reported in 2009 [12], differs most substantially from 1D-OKE in the method by which the intense THz pump fields are produced. Other factors of experimental setup, probe and pump polarizations, and data acquisition via a scanning delay stage are identical to the 1D-OKE technique. The most prominent difference in experimental setup between 1D-OKE, 1D-TKE, and 2D-TTR spectroscopies recorded using single-shot and

stage scan techniques lie in the probe pathway and data processing. Here, we lay out the constant elements underpinning all of these experiments, and then discuss small variations in how the pump fields are produced. Details specific to single-shot detection are found in Chapter 5.

A 1 kHz Coherent Legend UltraShort Pulse (USP) regenerative amplifier seeded with an 80 MHz Coherent Micra oscillator is used for all nonlinear experiments. The Legend output pulses are split, with 85% of the beam pumping a Light Conversion TOPAS-C optical parametric amplifier (OPA; input 3.2 mJ, $\sim 30\%$ conversion efficiency signal+idler) and a small portion of the remainder used for the detection of Kerr effect signals. Nonlinear pumping of a sample is achieved by using the $\sim 1.4 \mu\text{m}$ signal output of the Light Conversion TOPAS optical parametric amplifier. High-pass filtering can separate residual visible light for 1D-OKE experiments, but more commonly the beam is low-pass filtered to isolate the infrared light which then pumps an organic crystalline THz emitter. The current optical/THz pump transport pathway consists of three off-axis parabolic (OAP) mirrors which collect, expand, and re-focus light from the pump source onto the sample. Pump light is received by the system using a $f = 25.4 \text{ mm}$ gold coated OAP (25.4 mm \varnothing). This light is quickly focused down and captured by a $f = 190 \text{ mm}$ gold coated OAP (50.8 mm \varnothing). The now pseudo-collimated pump beam is finally transported to a $f = 50.8 \text{ mm}$ gold coated OAP (50.8 mm \varnothing) which focuses the light onto the sample of interest. For 2D TTR measurements, a wire grid polarizer is added before the first OAP as a beam combiner.

One key design consideration for the THz pump transport pathway is the diameter of the organic crystal emitter relative to the magnification imparted by the OAPs. With the development of large area organic crystalline THz emitters, the diameter of the emitted THz beam entering the first OAP can approach 6 mm. To a first order approximation, magnification by the first two OAPs by a factor of 7.5 expands the THz beam diameter to 45 mm, which is quite close to the diameter of the second OAP. Thus, there is an upper useable limit to commercially available emitter sizes without redesigning the pump transport optics. Larger emitters necessitate smaller magnification factors, which could have the additional benefit of reducing the length a THz field has to travel within the experiment.

Another consideration related to the transport of THz radiation is the location of the emitter relative to the first OAP. Since THz wavelengths are at the boundary between optical and quasi-optical systems [13], beam divergence from nominally

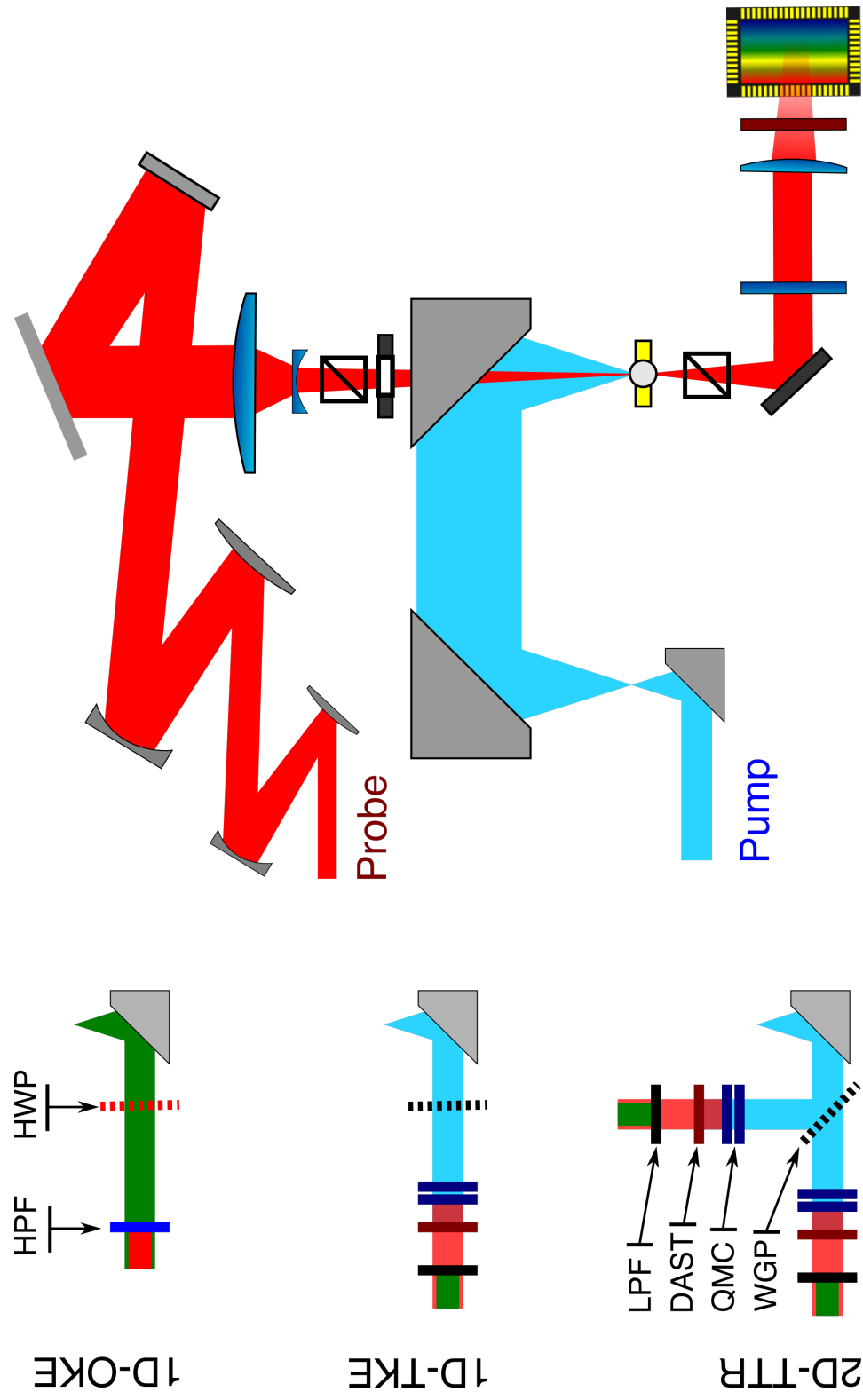


Figure 4.5: Diagram of the single shot Kerr effect experimental apparatus. Details on the probe pathway are given in Chapter 5. Abbreviations in figure: HPF - high pass filter; HWP - half wave plate; LPF - low pass filter; DAST - THz emitter; QMC - THz low pass filter; WGP - wire grid polarizer.

collimated, millimeter diameter sources must be considered. One very useful and intuitive approach for evaluating THz transport along the optical path uses ABCD matrices.

$$\begin{pmatrix} r' \\ \theta' \end{pmatrix} = \begin{pmatrix} A & B \\ C & D \end{pmatrix} \begin{pmatrix} r \\ \theta \end{pmatrix} \quad (4.8)$$

These 2×2 matrices characterize the radius r and divergence θ of a beam (represented by a 1×2 vector) propagating through an optical element, be it a lens or free space. Under the paraxial (small divergence angle) approximation, the action of a lens with focal length f is specified by:

$$\begin{pmatrix} 1 & 0 \\ -1/f & 1 \end{pmatrix} \quad (4.9)$$

while propagation through free space a distance d is given by:

$$\begin{pmatrix} 1 & d \\ 0 & 1 \end{pmatrix} \quad (4.10)$$

Transfer matrices for off-axis parabolic mirrors are much more complex [14]; to calculate the THz beam transport pathway to a reasonable approximation, these elements may be treated as lens. Doing so, we can examine all properties of the pump transport, including optimizing the distance between the emitter and first OAP, OAP telescope magnification, and theoretical THz spot size at the final focus. The frequency dependent response is naturally included by considering the beam divergence, which is calculated as $d = \frac{\lambda}{2\pi r}$, where λ is the pump wavelength and r the pump radius. Fig. 4.6 shows how the transport efficiency of THz light can change for a system based upon the location of the emitter relative to the first OAP, and the frequency of the THz field. Larger divergence at 1 THz cf. 10 THz can quickly lead to over-expansion of the beam if the emitter is placed too far from the collection OAP. This effect is quite pronounced with a 6 mm diameter emitter, and becomes more important as the emitter diameter decreases.

1D-OKE

Optical Kerr effect (1D-OKE) measurements used an optical pump at ~ 520 nm, which is naturally produced during the generation of the TOPAS signal beam fun-

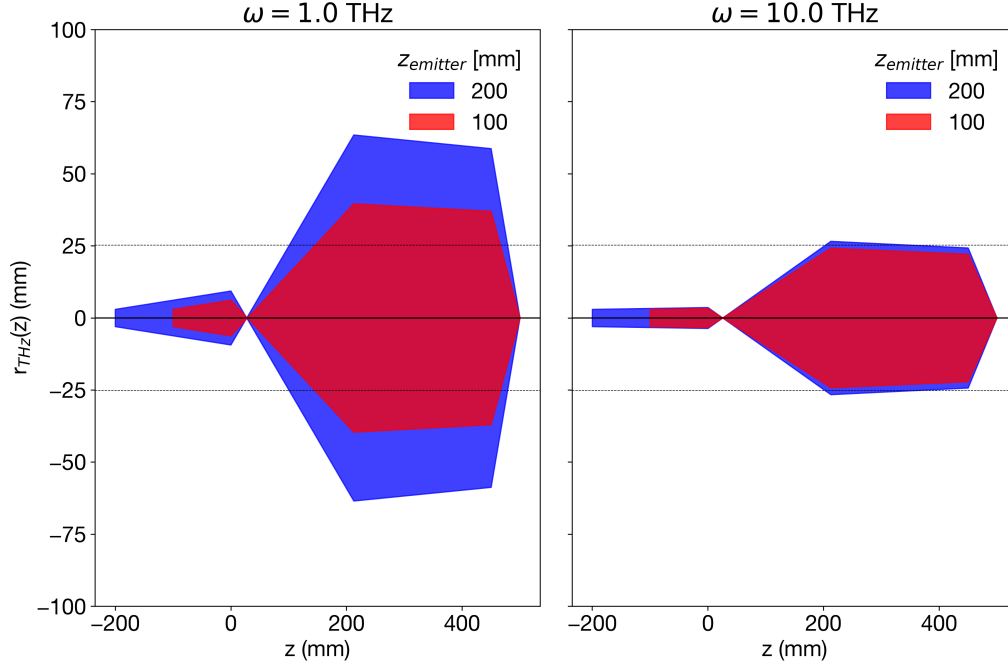


Figure 4.6: The THz pump beam radius along the transport pathway calculated as a function of THz frequency and the emitter's distance from the first off-axis parabolic mirror. Greater divergence is expected for lower frequencies, which can result in over-expansion of the beam relative to the OAP's 25.4 mm radius (dashed black lines).

damental at $1.4 \mu\text{m}$. Residual 800 nm and signal light was removed with two high pass filters. A neutral density filter was used to further attenuate the $70 \mu\text{J}$ optical pump pulse down to $\sim 8 \mu\text{J}$ (4 mW average power at 500 Hz modulation.) such that the beam would not strike a plasma when focused at the sample. After filtering and attenuation, the pump beam was directed through a half wave plate to rotate the horizontally polarized pump beam by 45° . The output of the OPA is modulated with an optical chopper referenced to the 1 kHz regenerative amplifier TTL output. The pump beam was then expanded with a $7.5\times$ magnification off axis parabolic mirror (OAP) telescope and focused onto the sample with a third OAP mirror (Fig. 4.5). The $1/e^2$ radius of the pump spot at the sample was estimated to be 60-70 μm , corresponding to an average power density of 31 W/cm^2 (peak power of $\geq 60 \text{ GW/cm}^2$). A conical hole machined into the rear side of the third OAP mirror provided clearance for the probe beam to pass through with minimal clipping on the sides of the mirror. The exit hole at the OAP front surface was 3 mm in diameter, which negligibly attenuated the 50 mm diameter pump beam.

THz generation

As third-order spectroscopies, the Kerr effect signal magnitude is highly dependent upon the pump electric field strength. In the first demonstration of 1D-TKE, the inorganic crystal lithium niobate (LiNbO_3) was used to generate an intense, < 1 THz pump field via optical rectification [12]. Improvements in the conversion efficiency, emission bandwidth, and reductions in cost of paired anion-cation organic crystalline emitters such as DAST (4-N,N-dimethylamino-4'-N'-methyl-stilbazolium tosylate) and DSTMS (4-N,N-dimethylamino-4'-N'-methyl-stilbazolium 2,4,6-trimethylbenzene sulfonate) have allowed these emitters to rival LiNbO_3 as go-to high-field THz sources [15, 16, 17, 18].

Apart from large achievable field strengths (commonly reported in excess of 10 MV/cm) and higher bandwidths, a further benefit of organic emitters compared to LiNbO_3 is the simple optical setup. In contrast to the use of wedged LiNbO_3 crystals, which use non-co-linear optical pumping schemes to improve index matching during optical rectification, organic emitters can simply be irradiated with a 1-2 μm pump beam. Rotation of the crystal about the axis of propagation quickly improves the alignment of the optical axis to the pump polarization, resulting in intense few-cycle THz radiation with minimal effort.

1D-TKE

For terahertz Kerr effect (1D-TKE) measurements, dry nitrogen was used to remove water vapor from the terahertz pump path. The unfiltered 500 μJ 1.4 μm TOPAS signal beam pumped a 6 mm diameter DAST organic crystal THz emitter (Swiss Terahertz). Residual pump light after the DAST emitter was removed with two THz band-pass filters (QMC). The THz pump followed the same path as in 1D-OKE, with the addition of a wire grid polarizer in the collimated region between OAP 2 and OAP 3 to enforce the 45° pump polarization. The THz pump pulse energy was $\sim 1.5 \mu\text{J}$, and was focused by the third OAP to a $1/e^2$ radius of 200 μm at the sample, producing an average power density of 0.6 W/cm^2 (and an estimated peak power exceeding 1 GW/cm^2).

One general assumption made in 1D-TKE and 2D-TTR measurements is that there is minimal extra heating of the sample despite the much larger absorption cross-section of liquids at THz cf. optical frequencies. For example, under a unity efficient absorption of each THz pulse by the sample, the energy deposited into the probed volume would raise the local temperature by ~ 100 milliKelvin. Distribution of this

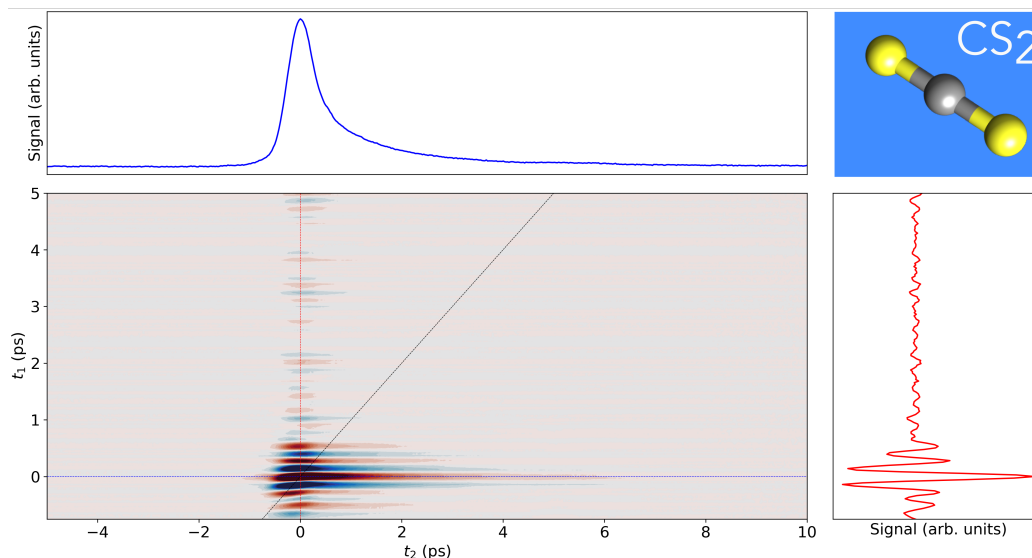


Figure 4.7: The 2D-TTR response of carbon disulfide (CS_2). Main panel shows the full 2D data set, while the colored slices at $t_1 = 0$ and $t_2 = 0$ are shown in the side panels. A clear orientational decay occurs along t_2 , while the t_1 response provides information on the experimental electric fields. The black dashed line marks $t_1 = t_2$.

local thermal energy into the bath states is expected to be quite efficient, occurring on the picosecond time scale. With kHz pump rates, the sample should always be at thermal equilibrium with the bath states.

2D-TTR

2D-TTR experiments divided the 500 μJ 1.4 μm signal output with a 50:50 beam-splitter. One OPA pump line was passed off a mechanical stepping delay stage which controls the relative time delay between the two pump fields. Additionally, one of the 1.4 μm pump line's polarization was rotated 90 degrees with a half wave-plate. Two 6 mm clear aperture DAST THz emitters (Swiss Terahertz) generate orthogonally polarized THz fields. Emission from the two sources was recombined and collimated with a wire-grid polarizer (WGP). After recombination, the THz light was filtered with 4 QMC 18 THz low-pass filters (2 after each crystal) to remove any residual optical bleed-through. The THz light was collected, collimated, and focused with a series of off-axis parabolic (OAP) mirrors before being focused onto the sample.

4.3 Data analysis

Kerr effect data acquired using either a traditional stage scan or a single-shot approach will have a constant set of common features. For illustrative purposes, the 2D-TTR response of carbon disulfide (CS_2) is shown in Fig 4.7. The pump-probe time delay t_2 increases from left-to-right, while the pump-pump time delay t_1 increases from bottom-to-top. A slice at the maximum of the 2D response along t_2 is shown in the top panel. A sharp onset of signal at $t_2 = 0$ ps accompanies the excitation of the sample with the two pump fields. An instantaneous non-resonant electronic response marks the peak of the signal, as the electrons in the sample react more quickly than the nuclei to the applied pump fields. A gradual nuclear orientational decay accounts for the majority of the signal after several hundred femtoseconds. There are many phenomenological models in the literature for modelling the electronic and orientational components of the Kerr effect response for a liquid [5, 19, 20, 21]. For cases such as bromoform where the analysis focuses on intramolecular vibrational features, models for the orientational response may be fit and de-trended from the data.

4.4 The sample cuvette

A glass cuvette with a silicon nitride window on the entrance face is used for all liquid THz Kerr effect experiments. A $1\ \mu\text{m}$ thick, $5\times 5\text{mm}$ clear aperture silicon nitride membrane window (QX10500F, Norcada) is epoxied over a $1/4$ inch diameter hole (diamond core drill bit, SKU 415102, Santa Fe Jewelers) drilled into one side of a 1 mm path length glass cuvette (Z802689, Hellma absorption cuvette). Two notes of caution when building and using SiN membrane cuvettes. First, the membranes are extremely fragile, and should be handled as little as possible. Nylon-tipped tweezers should be used when extracting the membrane from the gel cap packaging and positioning onto the cuvette prior to adhering with epoxy. Second, the thin membrane flexes very easily, which effectively creates a lens at the sample surface that distorts the echelon imaging pathway. Care must be taken when covering the top of the cuvette to not form an air-tight seal which would create pressure, and lensing, in the cuvette during the course of an experiment.

The silicon nitride membrane's thinness and small nonlinear refractive index ($n_2 \approx 40\times$ smaller than diamond) results in a very weak nonlinear signal [22]. Nonetheless, the sensitivity of the single-shot spectrometer means the response can be measured relatively easily in an empty cuvette (Fig. 4.8). This signal is helpful for several reasons. As with diamond, the relatively flat phase matching across the visible and

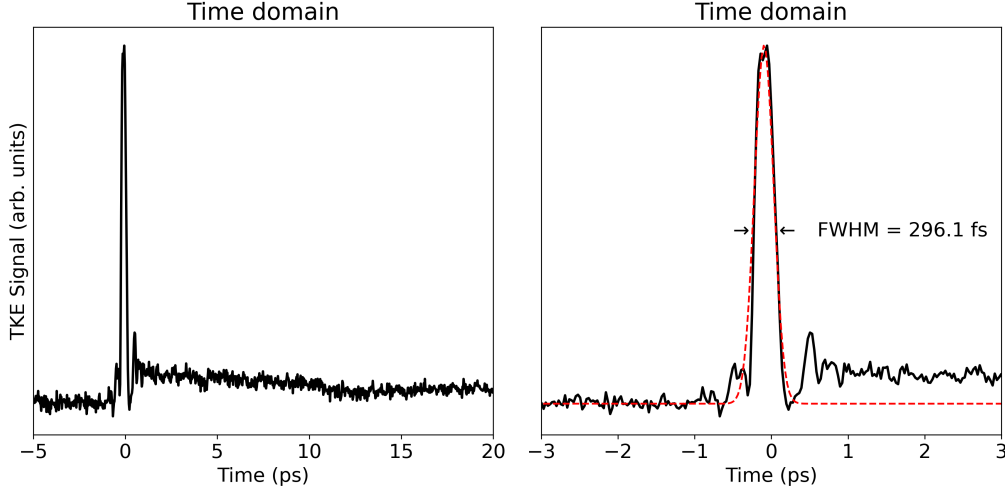


Figure 4.8: 1D-TKE response of the silicon nitride cuvette window, recorded under an argon gas atmosphere. The electronic response has a FWHM of ~ 300 fs, providing an estimate of $E_{THz}^2(t)$. A slight baseline offset after the main electronic response arises from a very slightly imperfect removal of background photons.

THz regions, and the extremely short path length, provide a reasonable achromatic estimate of $E_{THz}^2(t)$. For reference, DAST THz emission measured in SiN had a FWHM of ≈ 300 fs. Second, the magnitude of undesired scatter from the cuvette can be estimated from the integration time required to see the SiN 1D-TKE response. For a minimally scattering cuvette, a typical averaging time to resolve the peak SiN response from background noise is on the order of 10 seconds. A scattering cuvette can completely prevent observation of the SiN response.

While cuvette scatter is less of an issue for liquids with large n_2 (e.g. CS_2 , CHBr_3), water and aqueous solutions require a minimally scattering background. A useful comparison to estimate scatter is to fully remove the cuvette and observe the Kerr non-linearity created in the nitrogen atmosphere at the THz focus. (This response is quite interesting in its own right and will be discussed in detail in Chapter 8.) The SNR difference for a given integration time is indicative of the magnitude of scatter introduced by the cuvette, as well as the overall THz field strengths due to adequate focusing, and optimal pump-probe overlap.

BIBLIOGRAPHY

1. A. Tokmakoff, Orientational correlation functions and polarization selectivity for nonlinear spectroscopy of isotropic media. I. Third order. *Journal of Chemical Physics* **105**, 13–21, DOI 10.1063/1.471859 (1996).
2. M. Sajadi, M. Wolf, T. Kampfrath, Transient birefringence of liquids induced by terahertz electric-field torque on permanent molecular dipoles. *Nature Communications* **8**, 1–9, DOI 10.1038/ncomms14963 (2017).
3. A. Tokmakoff, Orientational correlation functions and polarization selectivity for nonlinear spectroscopy of isotropic media. I. Third order. en, *The Journal of Chemical Physics* **105**, 1–12, DOI 10.1063/1.471856 (July 1996).
4. I. B. Magdău, G. J. Mead, G. A. Blake, T. F. Miller, Interpretation of the THz-THz-Raman Spectrum of Bromoform. en, *J. Phys. Chem. A* **123**, 7278–7287, DOI 10.1021/acs.jpca.9b05165 (Aug. 2019),
5. Q. Zhong, J. T. Fourkas, Optical Kerr Effect Spectroscopy of Simple Liquids[†]. en, *J. Phys. Chem. B* **112**, 15529–15539, DOI 10.1021/jp807730u (Dec. 2008).
6. D. A. Turton, K. Wynne, Stokes–Einstein–Debye Failure in Molecular Orientational Diffusion: Exception or Rule? en, *J. Phys. Chem. B* **118**, 4600–4604, DOI 10.1021/jp5012457 (May 2014).
7. I. A. Finneran, R. Welsch, M. A. Allodi, T. F. Miller III, G. A. Blake, Coherent two-dimensional terahertz-terahertz-Raman spectroscopy. *Proceedings of the National Academy of Sciences* **113**, 6857–6861 (2016).
8. V. Y. Shishkov, E. S. Andrianov, A. A. Pukhov, A. P. Vinogradov, A. A. Lisyansky, Enhancement of the Raman Effect by Infrared Pumping. *Physical Review Letters* **122**, 153905, DOI 10.1103/PhysRevLett.122.153905 (2019).
9. S. Maehrlein, A. Paarmann, M. Wolf, T. Kampfrath, Terahertz Sum-Frequency Excitation of a Raman-Active Phonon. *Physical Review Letters* **119**, 1–6, DOI 10.1103/PhysRevLett.119.127402, arXiv: 1703.02869 (2017).
10. D. M. Juraschek, S. F. Maehrlein, Sum-frequency ionic Raman scattering. *Physical Review B* **97**, 1–8, DOI 10.1103/PhysRevB.97.174302, arXiv: 1801.05987 (2018).
11. M. A. Allodi, I. A. Finneran, G. A. Blake, Nonlinear terahertz coherent excitation of vibrational modes of liquids. *Journal of Chemical Physics* **143**, ISBN: 0831040831, 234204, DOI 10.1063/1.4938165 (2015).
12. M. C. Hoffmann, N. C. Brandt, H. Y. Hwang, K.-L. Yeh, K. A. Nelson, Terahertz Kerr effect. en, *Appl. Phys. Lett.* **95**, 231105, DOI 10.1063/1.3271520 (Dec. 2009).

13. P. F. Goldsmith, *Quasioptical systems: Gaussian beam quasioptical propagation and applications* (IEEE Press, Piscataway, NJ, 1998).
14. P. Argüjo, M. S. Scholl, Exact ray-trace beam for an off-axis paraboloid surface. en, *Appl. Opt.* **42**, 3284, DOI 10.1364/AO.42.003284 (June 2003).
15. C. Vicario *et al.*, High efficiency THz generation in DSTMS, DAST and OH1 pumped by Cr:forsterite laser. en, *Opt. Express* **23**, 4573, DOI 10.1364/OE.23.004573 (Feb. 2015).
16. A. Schneider, I. Biaggio, P. Günter, Optimized generation of THz pulses via optical rectification in the organic salt DAST. en, *Optics Communications* **224**, 337–341, DOI 10.1016/j.optcom.2003.07.013 (Sept. 2003).
17. B. Monoszlai, C. Vicario, M. Jazbinsek, C. P. Hauri, High-energy terahertz pulses from organic crystals: DAST and DSTMS pumped at Ti:sapphire wavelength. en, *Opt. Lett.* **38**, 5106, DOI 10.1364/OL.38.005106 (Dec. 2013).
18. M. Jazbinsek, U. Puc, A. Abina, A. Zidansek, Organic Crystals for THz Photonics. en, *Applied Sciences* **9**, 882, DOI 10.3390/app9050882 (Mar. 2019).
19. C. H. Kwak, G. Y. Kim, Rigorous theory of molecular orientational nonlinear optics. en, *AIP Advances* **5**, 017124, DOI 10.1063/1.4906521 (Jan. 2015).
20. K. Kiyohara, K. Kamada, K. Ohta, Orientational and collision-induced contribution to third-order nonlinear optical response of liquid CS₂. en, *J. Chem. Phys.* **112**, 12 (2000).
21. X. Ji *et al.*, A combined instantaneous normal mode and time correlation function description of the optical Kerr effect and Raman spectroscopy of liquid CS₂. en, *The Journal of Chemical Physics* **112**, 4186–4192, DOI 10.1063/1.481539 (Mar. 2000).
22. M. Sajadi, M. Wolf, T. Kampfrath, Terahertz-field-induced optical birefringence in common window and substrate materials. *Optics Express* **23**, 28985, DOI 10.1364/oe.23.028985 (2015).

Chapter 5

FUNDAMENTALS OF SINGLE-SHOT SPECTROSCOPY

While simple in principle, there are significant design considerations when building a single-shot Kerr effect spectrometer. In this chapter, we will discuss the characteristics of the nickel echelon, and issues and solutions encountered in designing the optical imaging pathway and data acquisition. Experimentally helpful diagnostic procedures that use the camera are also discussed. Portions of this chapter were re-used with permissions from:

G. J. Mead *et al.*, An echelon-based single shot optical and terahertz Kerr effect spectrometer. *Review of Scientific Instruments* **90**, 053107, DOI 10.1063/1.5088377 (May 2019),

G. J. Mead *et al.*, Sum-Frequency Signals in 2D-Terahertz-Terahertz-Raman Spectroscopy. *J. Phys. Chem. B*, acs.jpcc.0c07935, DOI 10.1021/acs.jpcc.0c07935 (Sept. 2020),

5.1 Overview

Single-shot spectroscopies use multiplexing techniques to encode molecular information onto a degree of freedom that can be measured with each laser pulse (in a “single-shot”). There are a wide variety of approaches and applications in the literature [3] that may be grouped under spectral, temporal, or hybrid multiplexing techniques (Fig. 5.1). In the case of the echelon-based single-shot spectrometer considered here, reflection from a large area (30×30 mm²) computer numerically controlled (CNC) machined reflective nickel echelon imparts a temporal wave-front across the width of a large diameter probe beam (Fig. 5.2). This wave-front allows the spectrometer to measure tens of picoseconds of molecular dynamics with no moving parts. A system of lenses images the echelon surface onto a scientific complementary metal–oxide–semiconductor (sCMOS) 5.5 megapixel Andor Zyla camera (Fig. 4.5). The molecular sample is placed in the transport path of the imaging system at the echelon image’s Fourier plane. Nonlinear polarization induced by the optical or THz pump within the sample produces a time-dependent change in the probe beam polarization, which is then encoded by the imaging system onto a spatial axis of the detector array.

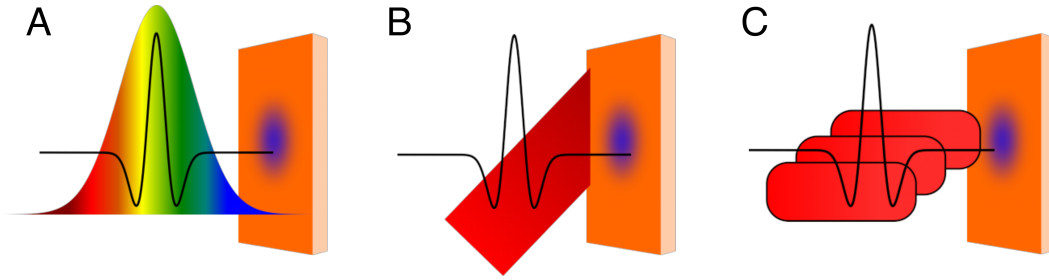


Figure 5.1: Three approaches to single-shot encoding of THz dynamics. A) Time-to-wavelength encoding of THz dynamics onto a spectrally chirped probe pulse. B) Time-to-angle encoding using non-collinear THz and probe pulses. C) Time-to-space encoding using a series of spatially dispersed probe “beamlets”. This work focuses on time-to-space encoding using a probe beam reflected off of a stair-step echelon.

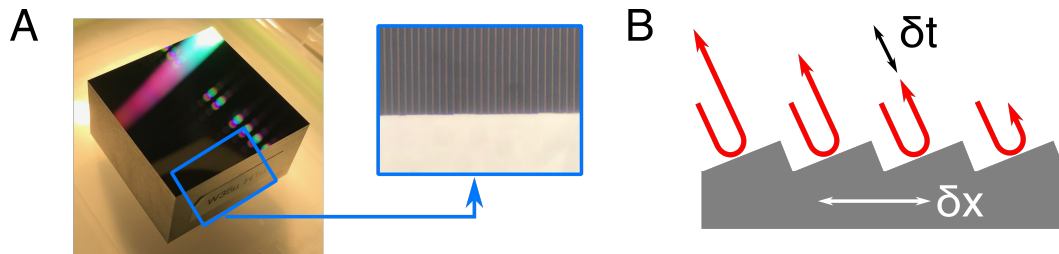


Figure 5.2: A) Photograph of the reflective echelon mirror. Note the slight diffraction effects in the reflected light. The stair-step grooves are visible in the inset micrograph of the echelon surface edge. B) Ray paths of the reflected probe light, clarifying the mapping between the spatial echelon axis and the temporal pulse front.

In many cases, 1D-OKE and 1D-TKE data with good signal-to-noise are captured within a few seconds of integration. Electro-optically sampled THz-TDS measurements require even less integration time; useful data can be recorded in milliseconds with a 1 kHz regenerative amplifier system. Similar time savings were realized in the multi-dimensional THz experiments: a well optimized single-shot 2D-TTR experiment can collect $> 10\times$ more data per unit integration time compared to the dual stage scan approach.

While reflective echelons offer substantial time savings over traditional stage scan experiments, their limitations must also be recognized. Experimental setup is non-trivial because of the care required to properly image the echelon onto the detector with a low photon background and minimal distortions induced by lensing effects and other aberrations. Other limitations of the echelon-based approach include the fixed sampling rate of the echelon, which imposes a fixed temporal window on the

data. Diffraction effects are also present at the focal region at the sample, as are vignetting effects. Each of these challenges and their solutions will be discussed in further detail below.

5.2 Probe transport pathway

A few words of caution are appropriate before discussing the imaging pathway in more detail. The Zyla camera is an extremely sensitive instrument. First and foremost, always minimize the amount of probe light reaching the detector. Two crossed nanoparticle film polarizers (LPVIS050-MP2, Thorlabs) with $10^7:1$ extinction ratio at 800 nm are always placed in the probe path. If removal of one or both of the polarizers is required, block the probe path with the manual shutter and block the detector with aluminum foil over the lens tube. Very small angular adjustments to the polarizers and quarter wave plate can easily saturate the detector. Second, an 800 nm band-pass filter is used to remove residual room light from reaching the detector.

A Raman probing process is used for all 1D-OKE/1D-TKE/2D-TTR experiments. The probe is derived from light that passes through the first beamsplitter after the Legend amplifier, and first passes through an iris to attenuate power. Pre-compensation is achieved by pre-chirping the probe with multiple bounces off of a negative group-velocity-delay (GVD) mirror pair. This step is helpful because of the multiple lenses and polarization optics that the probe must pass through. As shown in Fig. 4.5, probe beam then passes through two reflective $8\times$ magnification Gaussian telescopes before illuminating the reflective echelon. This expansion increases the beam diameter from $\sim 2\text{mm}$ to 50mm , creating a relatively homogeneous intensity profile across the reflective echelon surface.

Once the echelon surface is illuminated, the probe transport quickly becomes more complex. The probe must travel around and through multiple optical components, including polarization optics, the final holey OAP, and onto the sCMOS detector, without any severe reduction in light intensity due to clipping. Ray transfer ABCD matrices again become useful here for modeling the probe beam diameter along the imaging pathway (Fig. 5.3). After reflecting off the echelon, a Barlow lens pair is used to achieve the initial focusing of the large diameter probe through a thin-film polarizer, quarter wave plate, the hole in the third OAP, and onto the sample. A crossed polarizer immediately after the sample attenuates the vast majority of probe light while allowing photons rotated by the nonlinear birefringence in the sample to

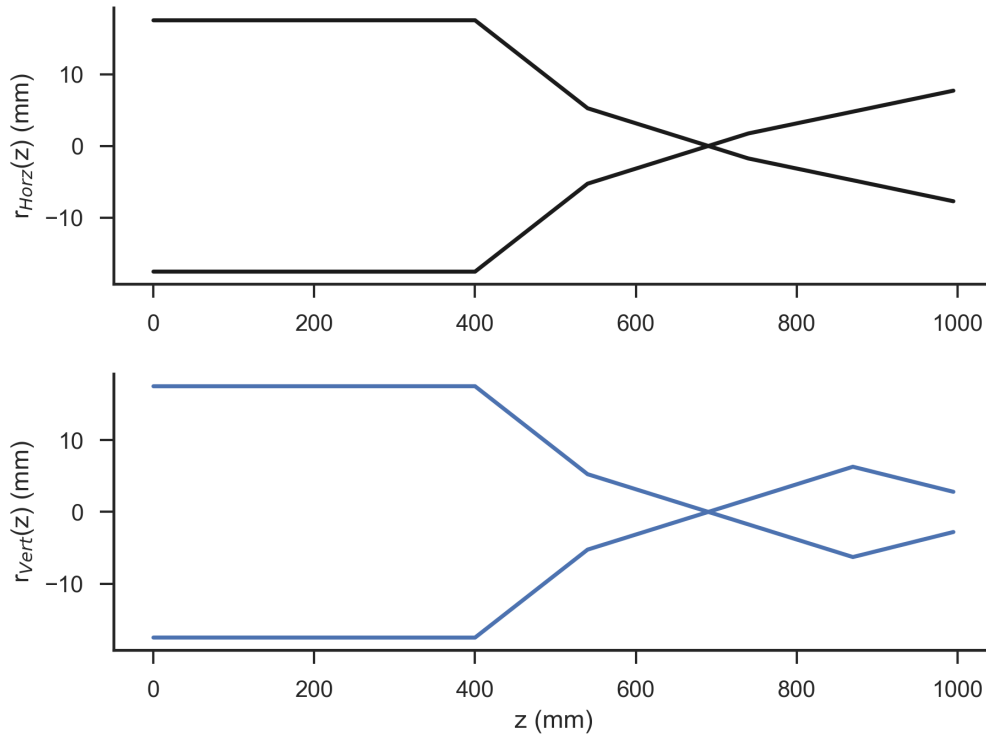


Figure 5.3: Ray transfer matrix calculations of the horizontal and vertical probe beam dimensions throughout the echelon imaging pathway. The left hand side corresponds to the echelon surface; the right hand side the sCMOS detector surface.

pass. Two cylindrical lenses then perform the final image de-magnification along the horizontal and vertical laboratory axes before the final image is formed on the camera detector.

5.3 Echelon imaging pathway

Equally important to the efficiency of the spectrometer is considering the echelon image formation pathway. A crisp image of the echelon surface must be formed on the camera surface using the probe transport lenses while creating a sharp focal region (Fourier plane) at the same position in three-dimensional space as the optical or THz pump focus, and while passing through numerous constrictions in the probe transport pathway (e.g. the small aperture drilled in the third OAP.)

First we will consider the image formation process. The illuminated echelon surface is treated as the first “object” in the imaging pathway. Light reflected from the echelon object travels a distance $z = O$ before passing through a lens with a focal length f , which creates an image at a image distance $z = I$ given by the relationship:

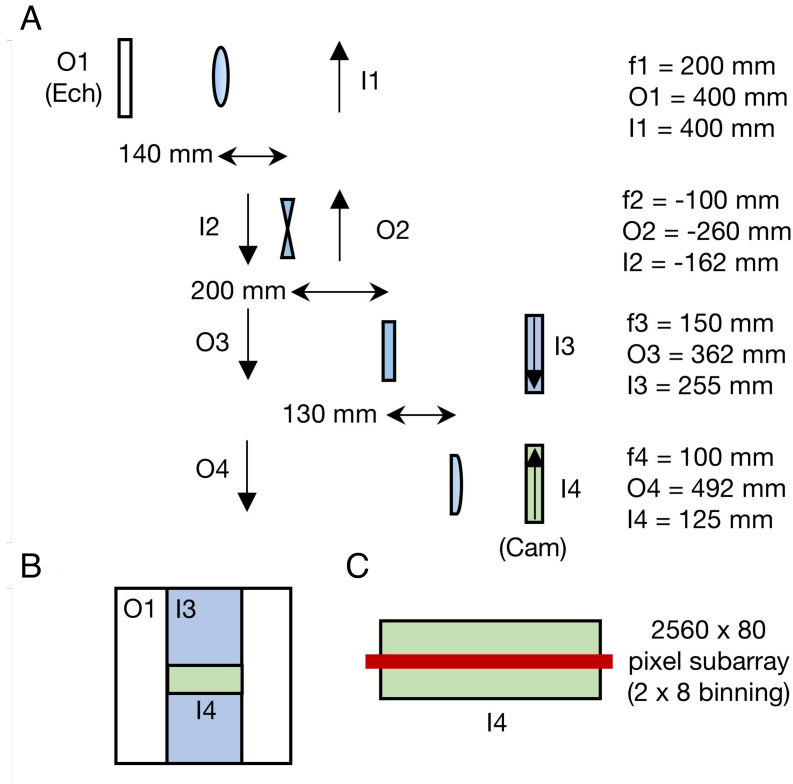


Figure 5.4: A) Echelon image formation pathway, specifying the position of the object and image for each imaging component. B) Comparison of the dimensions of the original echelon object (O1), the horizontally de-magnified image (I3), and the final vertically de-magnified image (I4). C) Comparison of the final echelon image on the detector array, versus the overall sCMOS detector array area.

$$z_{\text{Focal length}}^{-1} = z_{\text{Object}}^{-1} + z_{\text{Image}}^{-1} \quad (5.1)$$

This first image subsequently becomes the object for the second lens, which creates a second image that similarly propagates through a third lens, and so on. Changes in image magnification are given by the ratio of the image and object distance at each imaging step. A schematic of the full echelon imaging pathway is shown in Fig. 5.4. Verification of proper imaging onto the detector may be achieved by observing the image formed by probe light passing through crossed polarizers in the Solis program, as shown in Fig. 5.5.

Modulation transfer function

An imaging system's modulation transfer function (MTF) determines the intensity with which different spatial frequencies (cycles/mm) are transmitted by the system

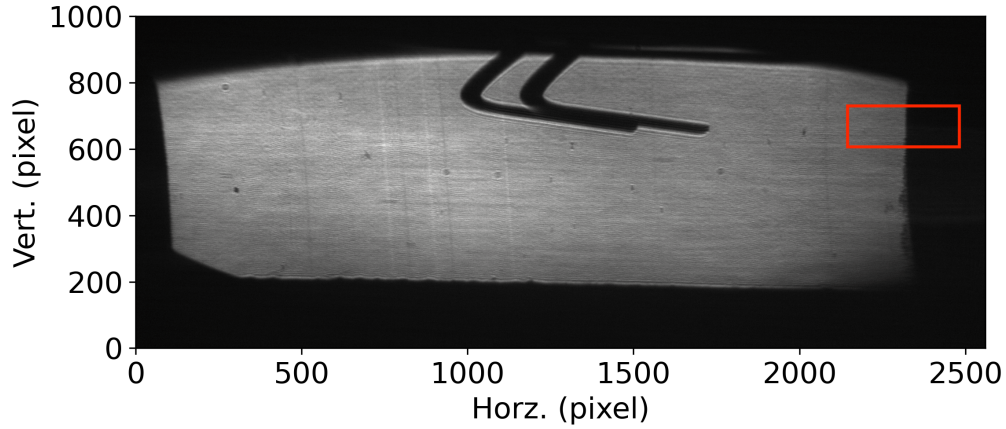


Figure 5.5: Image of the echelon surface after passing through the imaging pathway shown in Fig. 5.4. A small hex key is held close to the echelon surface to demonstrate the crisp image produced. The red rectangle is used for calculating the modulation transfer function in the next section.

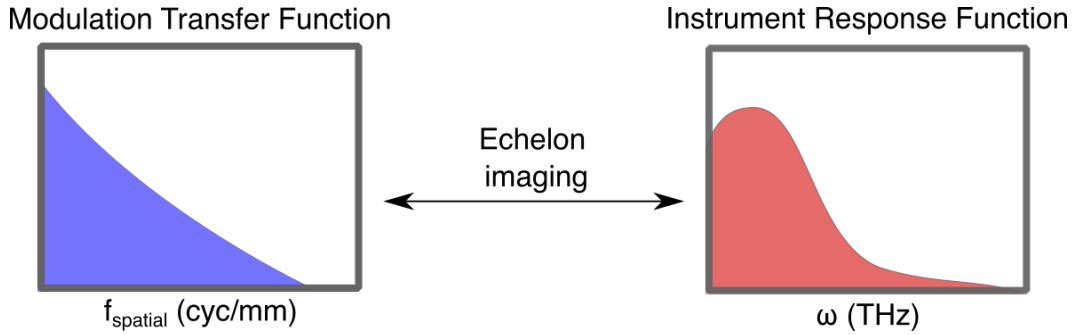


Figure 5.6: Correspondence between the experimental MTF and IRF

[4]. A well-focused system's MTF will peak at 0 cycles/mm and decrease linearly to a diffraction-limited cutoff at high spatial frequencies. Because of the time-to-space mapping of the echelon onto the camera, the MTF can directly limit the detectable spatial frequency along t_2 or, analogously, the detectable signal frequency on ω_2 (Fig. 5.6).

The MTF is commonly estimated by first measuring the edge spread function using a knife-edge test. We use the right-hand edge of the echelon image (Fig. 5.5) as a knife-edge cutoff. Several averages are taken vertically along the image and fit to an edge spread function $ESF = a + \frac{b}{1+e^{(x+c)/d}}$. Differentiating this response yields a line spread function, and subsequent Fourier transformation yields the final MTF.

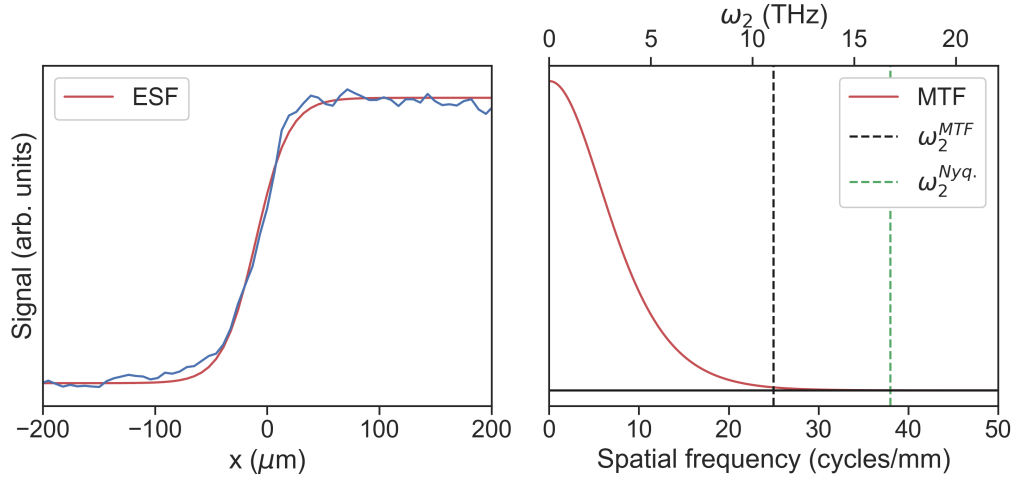


Figure 5.7: Edge spread function fits to experimental data of the edge of the echelon surface. Differentiation yields the line spread function, which is transformed into the MTF in the frequency domain. A cutoff of 25 cycles/mm or 11 THz is imposed by the imaging optics.

Calculation of the correspondence between the Nyquist frequency of the probe beamlets (at a 1:1 mapping of beamlets to 2x binned horizontal pixels) finds a MTF-limited probe frequency of around 11 THz. Thus, the Nyquist sampling rate of the probe is not the limiting factor in the single-shot system; instead, a lower frequency limit is set by the MTF.

5.4 Echelon constraints

Fixed sampling rate

Due to the nature of their construction, the Nyquist sampling rate of the machined echelon cannot be readily adjusted. The height H between adjacent steps with width W sets the sampling time point achievable for the echelon geometry, while the number of steps defines the overall temporal snap-shot the echelon can measure at a given probe-pump delay. While in theory the lack of adjustability is a limitation, in practice we have found a ~ 30 ps echelon with a Nyquist frequency of 16-17 THz provides a good balance between signal strength, optical power reaching the detector, and similarity of signal between single-shot measurements and reference stage scans. (Even with the relatively diffuse probe light, it is possible to fill the finite well depth of the detector pixels during EO-THz-TDS measurements thanks to the strength of the generated THz fields.) In the event a narrower temporal window with higher bandwidth is desired, a 6 ps echelon may be used. However, optimizing

its performance and linearity has been substantially more difficult, as discussed in following sections.

Diffraction effects

Weak diffraction effects from the echelon produce multiple reflected orders and results in an elongated focal spot size at the sample position. The elongated focal spot size can hamper detection of the Kerr signal by reducing the intensity of the probe pulse passing through the nonlinearly perturbed region of the sample. Kerr effect signals inherently scale linearly with the probe electric field ($\propto \sqrt{I_{probe}}$), so a reduction in probe intensity is clearly theoretically of concern. In practice, however, other limitations in the system, particularly the finite detector well depth, are benefited by the reduced signal intensity.

Substantially different focal spots may be achieved with different echelon step geometries. The fundamental equation describing diffraction off of an echelon with N steps of width W and height H , illuminated at an angle θ , is given by Eq 5.2 [5].

$$S \times I = \frac{\sin(\frac{N\pi(W\theta+2H)}{\lambda}) \times \text{sinc}(\frac{\pi W\theta}{\lambda})}{N \times \sin(\frac{\pi(W\theta+2H)}{\lambda})} \quad (5.2)$$

This equation contains an envelope response S and the diffraction order response I for a single wavelength. Applying Eq 5.2 to an 800 nm pulse with 30 nm of bandwidth, and picking out each wavelength's intensity in the primary diffraction order allows us to model the expected angular separation achieved when the reflected order is focused at the sample. As seen in Fig 5.8, the horizontal cross-section of the 30 ps and 6 ps echelon focal regions are reproduced well with Eq. 5.2.

Vignetting effects

Vignetting is characterized by an optical intensity envelope that sharply decreases towards the edges of the image. While of arguable artistic merit in other settings, the result of vignetting in single-shot experiments is an artificial modulation of the observed signal intensity. Although uneven illumination of the echelon surface can produce similar signal intensity modulations, this effect is most prominently correlated with passage through the perturbed region of a sample under tight focusing. Therefore, we hypothesize that vignetting arises from a nonlinear aperture created in the sample that acts as a constricting pupil which reduces the etendue of the imaging system.

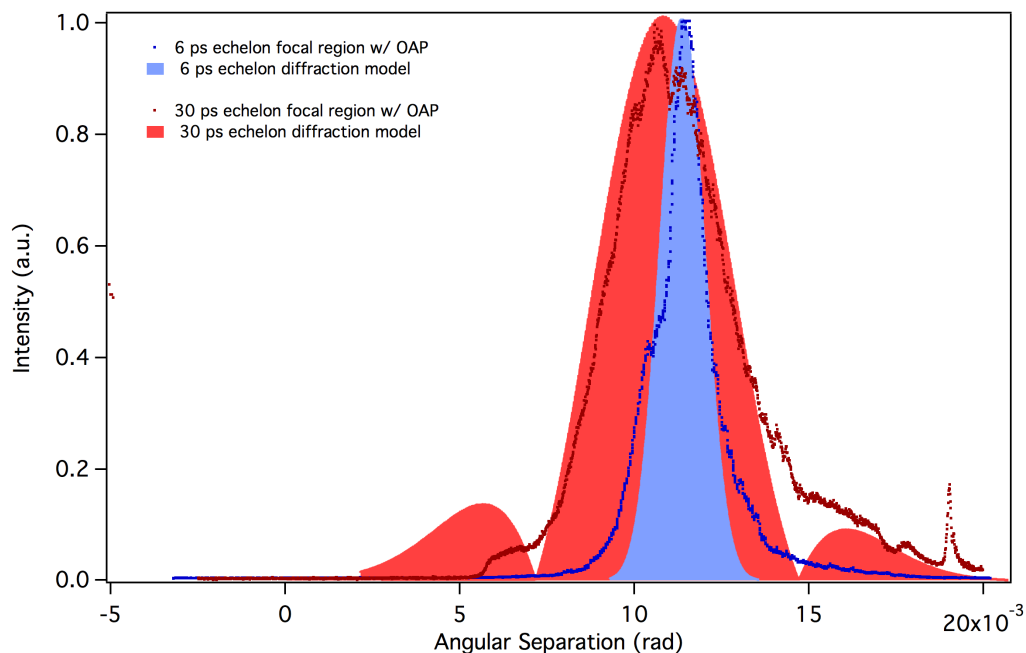


Figure 5.8: Comparison between the echelon angular separation model from Eq. 5.2 and the horizontal axis of the probe focus.

A clear example of vignetting is seen in a series of 1D-OKE experiments using the 6 ps echelon to measure the orientational decay of bromoform. Data were recorded as a function of sample position along the axis of propagation. Due to the fast focus pulled by the final OAP, small changes in the sample position rapidly change the pump intensity, while the softly focused probe beam changes much less rapidly. A clear qualitative effect was the correlation between the magnitude of vignetting and the pump focal size (Fig. 5.9). As the sample was moved away from the tightly focused region of the pump, the mono-exponential molecular response bordered with sharp edges at the edge of the echelon is recovered.

Removing the effects of vignetting is critical for the long-term utility of this technique, but may require substantial redesign of the probe optical transport pathway. In the interim, there are several ways to reduce vignetting. First, using the 30 ps echelon distributes the vignetting effect over a longer time, minimizing the effect over relevant molecular dynamics time scales. Second, positioning the molecular response in the center of the intensity profile ensures the majority of the signal is recorded in the most slowly varying region of the vignette envelope. Finally, softening the pump focus to the extent possible further decreases the impact of vignetting on the data. In the particular case of halogenated methanes, we are inter-

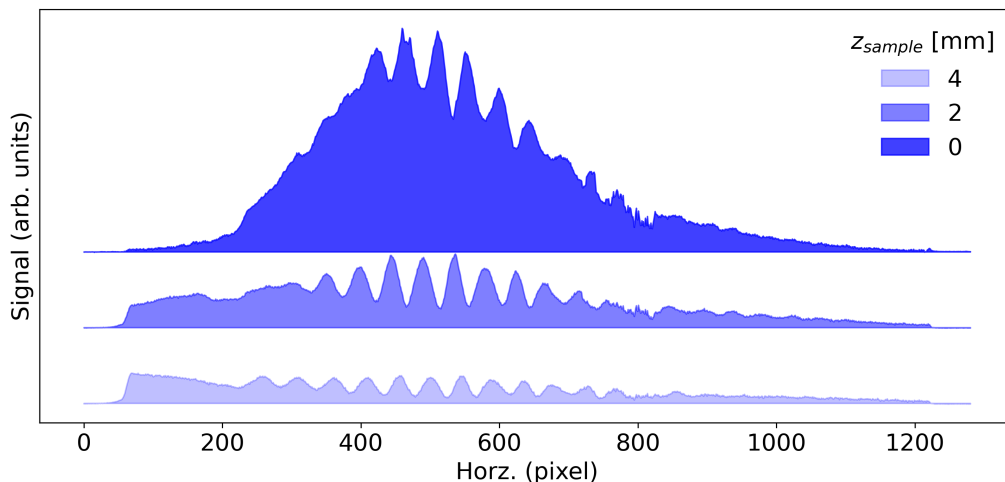


Figure 5.9: Vignetting of bromoform's orientational decay observed with a 6 ps echelon, plotted as a function of the sample position relative to the optical pump focus. At the signal maximum defined as $z_{sample} = 0$ mm, there are prominent distortions of the signal. Detuning the sample from the pump focus by 4 mm results in a less vignettted Kerr response.

ested in small, short-lived intramolecular coherences which are negligibly effected by vignetting.

5.5 Data acquisition

There are two software options available for data collection: the proprietary Andor Solis program and a home-built MATLAB GUI. Both have advantages in particular applications. For example, echelon imaging and diagnostic imaging of the system is most easily accomplished with the Andor Solis program. With the camera data cables connected to the acquisition computer and the camera powered on, simply open the Solis program. A host of acquisition parameters are listed on the right hand side of the program GUI. With the acquisition parameters set, it is important to record a background prior to recording data. This subtracts out the response of several dead pixels on the detector array.

The MATLAB GUI may be used to record all data from EO-sampled THz TDS, 1D-TKE/1D-OKE, and 2D-TTR experiments, and is a remarkably useful program thanks to the long hours and care Haw-Wei Lin has put into its design and functionality. As discussed in the following sections, MATLAB is also a very convenient method for orchestrating the numerous sub-systems required to perform single-shot 2D-TTR measurements.

Laser-to-camera communication

There are multiple input/output cables extending from the Zyla camera. The TRIGGER cable is used to externally trigger the camera's electronic global shutter. Because we would like to acquire every single laser shot emitted by the Legend regenerative amplifier, a TTL output from the SDG delay generator is routed directly to the Zyla TRIGGER input via a BNC cable. An advantage to using the SDG delay generator is the variable delay that can be added to the TTL output, which compensates for the distance the signal must travel between SDG and camera. To maximize the overlap between probe pulse arrival at the detector and the detector's global shutter, the SDG delay output timing can be scanned while observing video streamed from the Zyla camera to Solis.

Camera-to-computer communication

All commands to the camera and data streaming to the computer is accomplished using two 10 tap Camera Link cables. These cables directly connect to the rear of the camera housing and feed into a Camera Link PCI card installed in the computer.

Camera/optical chopper-to-DAQ communication

While the Zyla is the heart of the single-shot experiment, the National Instruments Data Acquisition Card (DAQ) is the conductor that synchronizes all of the different data streams for further MATLAB processing. The DAQ is initialized when the MATLAB GUI is started, and digitizes inputs from both optical choppers, the camera's SYNC output line, as well as a TTL signal from the Legend SDG (Fig. 5.10). These signals are sent to MATLAB and used as inputs to the lock-in detection algorithm, which replicates the phase-sensitive detection of standard stage scan experiments.

5.6 Single-shot data processing

While there are several divergent elements in the single-shot spectrometer compared to the traditional stage scan approach, perhaps the greatest difference is the lack of a digital or analog lock-in amplifier. Without this critical equipment, we had to develop techniques to extract the desired signal from a large background of probe photons. Two approaches were used, and are discussed here. The probe line beam conditioning for single-shot acquisition is unchanged, regardless of whether the data are from 1D-TKE/1D-OKE or 2D-TTR experiments.

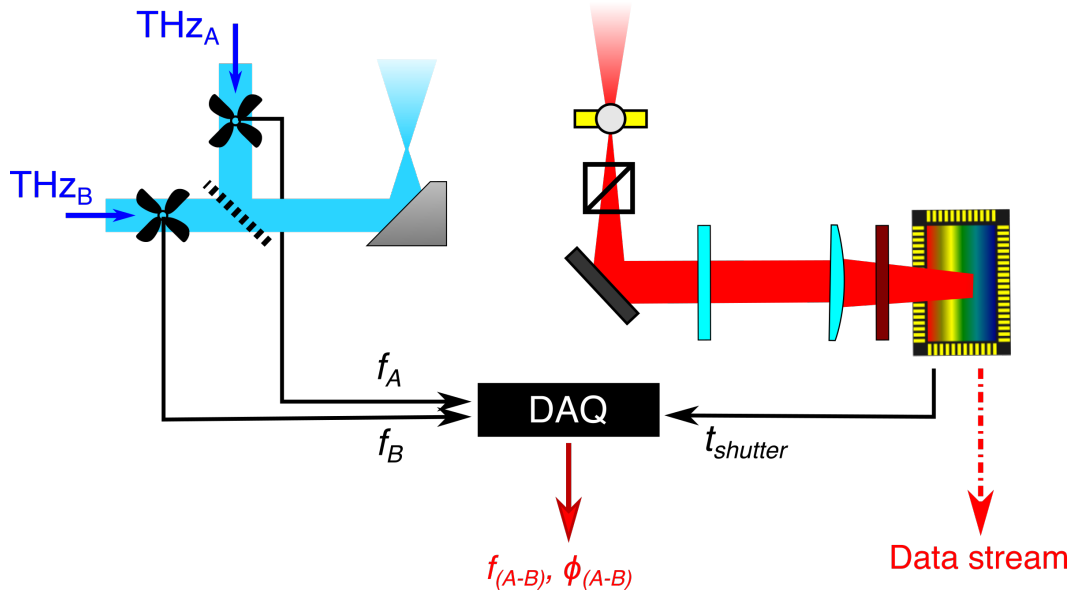


Figure 5.10: When performing 1D-TKE/1D-OKE and 2D-TTR experiments with the MATLAB GUI, a National Instruments DAQ card digitizes the chopper frequencies and phases, as well as the camera acquisition start signal. These three data sets, along with the raw camera data stream and 1 kHz TTL signal, are sent to the control computer for further processing by the GUI.

1D-TKE/1D-OKE (DAQ-free approach)

The first data processing approach was used for the one-dimensional Kerr effect measurements in [1]. Data were acquired at 1 kHz on the Andor Solis program. Acquisitions were triggered from the regenerative amplifier delay generator, and the exposure time was set to $800 \mu\text{s}$ so that only a single laser pulse was captured in each image. Chopping the pump beam at 500 Hz allowed for data to be acquired in an on-off manner, which compensated for drift from shot-to-shot fluctuations in beam intensity and pointing. Each data set consisted of 10,000 images (5,000 on, 5,000 off), that were acquired in 10 seconds and saved to disk in ‘.dat’ format. A Python script was then used for data processing, and is included in Appendix A.

After reshaping the raw data to match the camera dimensions and the number of images acquired, odd and even numbered images were separately co-added. The two data sets (corresponding to pump on and pump off conditions) were then subtracted and normalized by the pump off data set (Eq. 7.2). As the pump off data set corresponds to E_{LO}^2 , the subtraction of the two data sets removes this term. In the experimental case of $E_{LO} \gg E_{sig}$, the resulting signal becomes $E_{sig}^2 + 2E_{LO}E_{sig} \approx 2E_{LO}E_{sig}$.

$$\text{Sig}_{\text{O/TKE}} = \frac{\text{Sig}_{\text{ON}} - \text{Sig}_{\text{OFF}}}{\text{Sig}_{\text{OFF}}} \quad (5.3)$$

Due to the large file sizes produced by the camera's 1 kHz frame rate, integration times longer than 10 seconds quickly become difficult for the program to write and the computer to process. The frequency domain acquisition approach described in the next section avoids these limitations by keeping the camera data in RAM and performing data processing on-the-fly.

2D-TTR

A schematic of the computational steps in 2D-TTR data processing is shown in Fig. 5.11. All data and experimental parameters were controlled from the MATLAB GUI. Within the GUI, the number of acquisitions per average and the number of averages are specified by the user. To capture a data set at a given t_1 time, typical acquisition settings for bromoform are to collect 5 averages with 2,000 shots per average, for a total acquisition time of ~ 12 seconds, which includes 2 seconds of camera and computational overhead and the 10 seconds of data acquisition. The data set for each average is first collected as a $2,000 \times 1280$ array, with dimensions specified by the number of laser shots captured (e.g. 2,000) and the 1280 horizontal binned output pixels from the camera that capture the time-domain molecular response along t_2 at the fixed t_1 time. Once enough averages are acquired for one t_1 setting, the GUI will incrementally step across a range of t_1 times as specified by the user.

To extract the 2D-TTR signal from this data array, we first must calculate a sinusoidal waveform with a length equal to the number of shots recorded in each average. In this example, we will consider a 2,000 row data set. Differential chopping of the two THz pump fields ensures the 2D-TTR response is modulated at the difference of the two chopper frequencies. The waveform frequency is set equal to this difference frequency. Generating the proper waveform phase is also critical since each average is acquired at a random point in the differential chopping cycle. By using the signals digitized by the DAQ (chopper A and B frequency and phase, and the camera acquisition start time), we can compute the phase for each average and apply a correction factor to ensure all averages recorded for a fixed t_1 , as well as all averages recorded as t_1 changes, have a fixed uniform phase. This preserves the overall phase of the 2D-TTR signal while eliminating the need to coordinate the chopper phases and camera acquisition in real time.

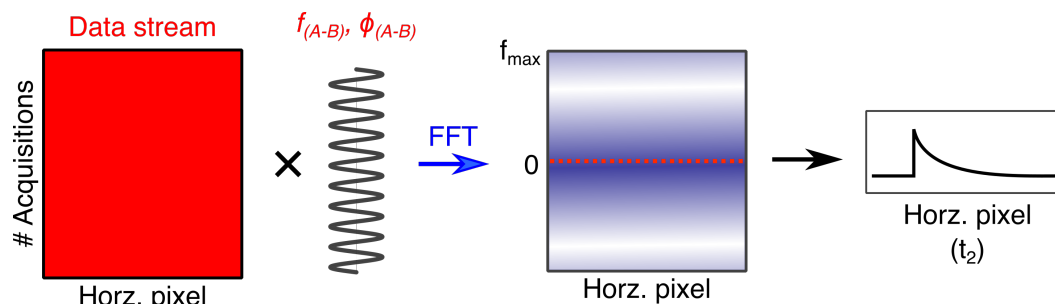


Figure 5.11: Schematic representation of the MATLAB data processing. By performing a Fourier transform on each horizontal pixel column with a reference sinusoid, the difference frequency signal is shifted to the 0 Hz position of the spectrograph.

With a properly constructed waveform, this signal is multiplied with each of the 1280 columns of data before an FFT is performed on each column. Multiplication shifts the desired differential signal to the DC position in the frequency domain FFT output. The DC response from all 1280 channels are then saved as a 1×1280 data array for each average, and are co-added until all averages are collected. In essence, this approach creates a software equivalent to the standard digital lock-in amplifier typically used for collection of single channel spectroscopic data.

5.7 Diagnostic imaging using the Andor camera

Polarimetric imaging with Solis is helpful for optimizing a myriad of experimental conditions, from THz and probe focusing to echelon imaging and order identification. *Note: never use the following techniques to image an optical pump spot. The camera detector will be permanently burned.*

THz pump imaging

Directly imaging the THz focal region is difficult to accomplish with most detectors available on the market, although a few niche products, such as the Rigi Camera (Swiss Terahertz) have recently come to market. While these direct THz imaging cameras require the most minimal setup (typically only requiring placing the detector in the focal plane of the THz beam), they are sensitive to thermal noise, and are extremely susceptible to damage from the intense THz beam. Attenuation with multiple silicon wafers and wire grid polarizers is usually required to safely image the focal plane of an organic crystalline THz emitter.

An alternative approach for THz imaging is naturally presented in the spectrometer

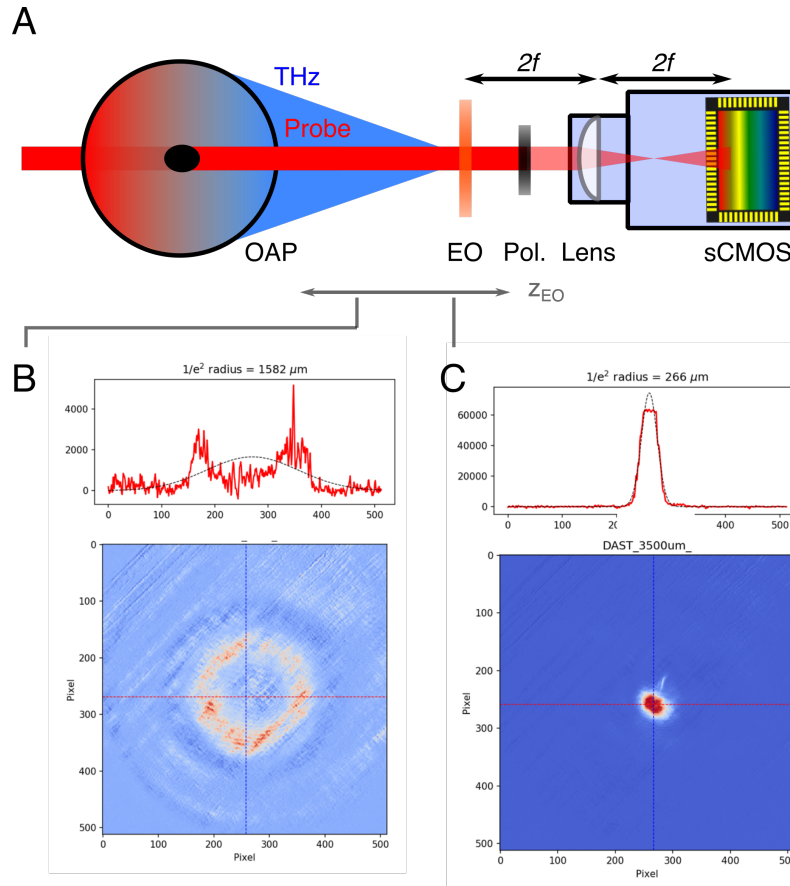


Figure 5.12: A) The focal region of the THz pump may be observed using an electro-optic crystal such as ZnTe imaged with a simple $4f$ lens configuration. Take care that the polarizer after the EO crystal is fully blocking the majority of the probe light. Scanning the EO crystal along the z -axis of the THz beam, with appropriate adjustments to the lens and camera assembly, allows the symmetry of the THz light cone to be observed over several millimeters (B), and the beam waist region (C) to be measured.

setup. This approach uses the surface of an EO crystal as a primary detector whose birefringent response to THz light is detected by a loosely collimated probe beam that collinearly passes through the EO crystal. Only a few minor modifications are required to transform the single-shot spectrometer into a THz imaging camera. The second, concave lens in the Barlow lens pair is first removed to generate a large diameter, pseudo-collimated beam that passes through the OAP hole and illuminates a large area of the EO crystal. An imaging lens is then added to the lens tube attached to the camera. Finally, the camera is retracted along its rail to a position where the imaging lens is symmetrically positioned in a $2f - 2f$ configuration between the EO crystal surface and the camera detector surface (Fig. 5.12 A).

Using Solis, a crisp image of the EO crystal surface should easily be seen (Fig. 5.12 B and C). With the optical probe and THz pump delay aligned to zero temporal offset, a bright spot will be observed on the crystal surface. From here, the emitter rotation and orientation relative to the TOPAS pump beam can be optimized for maximum THz generation. Tuning the OAP mirrors is somewhat helpful for optimizing the symmetry of the THz focus along the Z axis. However, this is less helpful in reducing the THz focal spot size in the XY plane, especially if the $1.4\ \mu\text{m}$ pump beam is already focused into a plasma at each of the two OAP focal points along the transport pathway. *Note: never image the TOPAS pump beam plasma with this technique.*

Combining and aligning the two THz pump beams with the wire grid polarizer is especially simple with this imaging technique. First, simply find the EO THz-TDS signal of each line using the spectrometer. Next, transition to the imaging setup and find each THz pump on the crystal surface. Note the crystal may need to be rotated 90° to pick up the orthogonally polarized THz beams. Maximum overlap of the two THz pumps is achieved by slight walking of the two mirrors leading the THz emitter whose emission is reflected by the wire grid polarizer. Tuning the WGP angle of reflection is also critical for improving overlap of the two THz pumps. Ultimately, the best route for alignment is maximizing the power of the transmitted THz pump beam (e.g. by achieving plasma at both OAP focal planes), and then bringing the reflected THz pump into alignment with the transmitted THz pump.

Probe imaging and pump-probe overlap

An identical process is useful for imaging the probe focal spot quality (Fig. 5.13). The two cylindrical imaging lenses may be removed while the Barlow lens combination is left in place. The $2f - 2f$ imaging lens can then be tuned to observe the probe focal region. Diagnostic applications include, e.g., identifying clipping on the third off-axis-parabolic mirror. This is easily determined by observing the focal spot with and without the OAP present. A small amount of clipping is acceptable, since the image of the echelon is contained at every point along the echelon focus. (This fact explains why 30 ps of molecular dynamics can be measured even when the pump overlaps with only a small portion of the probe at the focal region.) Overlap of the THz pump and optical probe can be achieved by imaging the two spots on the surface of an EO crystal (Fig. 5.14). Note, again, to never perform these observations with an optical pump spot.

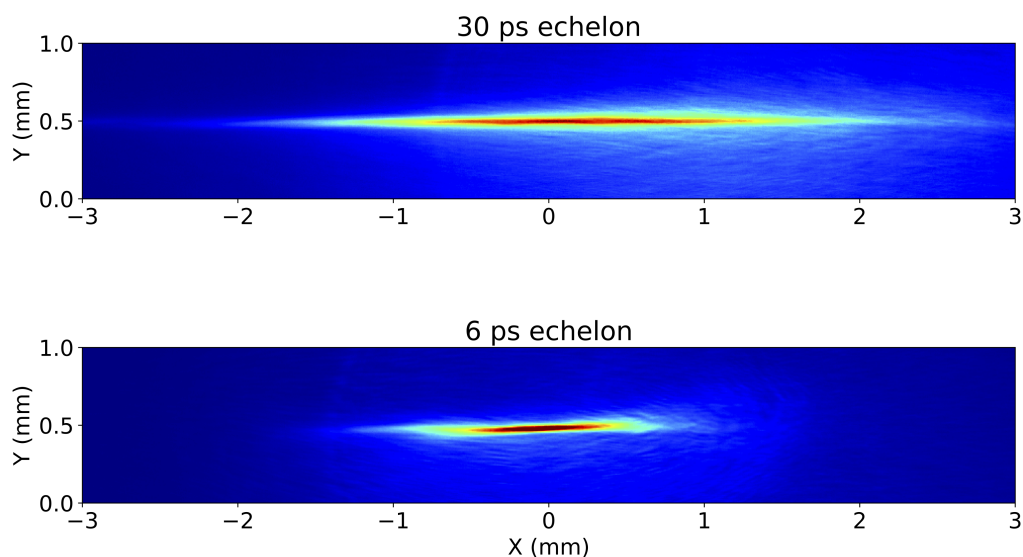


Figure 5.13: Comparison of the 30 ps and 6 ps echelon probe focal spots. The effects of diffraction are clearly observed in the horizontal extent of the two probe beams.

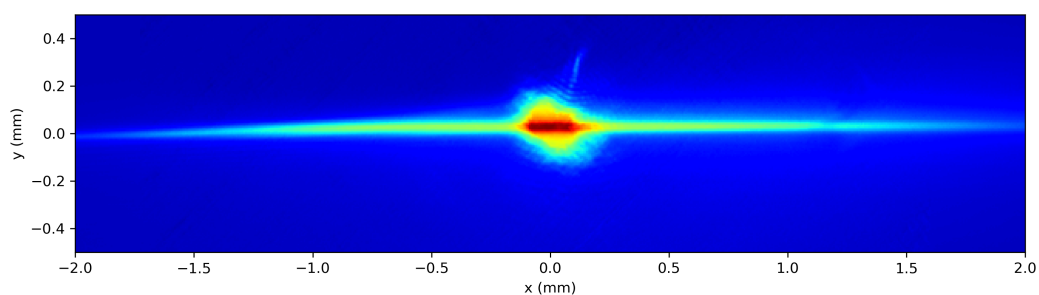


Figure 5.14: Pump-probe focal spot overlap. This image is a composite of two images, one of the probe focal spot imaged without an EO crystal present, and the other of the THz pump imaged with an EO crystal. A small amount of scatter will be present when an EO crystal is used to directly image the pump-probe overlap.

BIBLIOGRAPHY

1. G. J. Mead, I. Katayama, J. Takeda, G. A. Blake, An echelon-based single shot optical and terahertz Kerr effect spectrometer. *Review of Scientific Instruments* **90**, 053107, DOI 10.1063/1.5088377 (May 2019),
2. G. J. Mead, H.-W. Lin, I.-B. Magdau, T. F. Miller, G. A. Blake, Sum-Frequency Signals in 2D-Terahertz-Terahertz-Raman Spectroscopy. en, *J. Phys. Chem. B*, acs.jpcc.0c07935, DOI 10.1021/acs.jpcc.0c07935 (Sept. 2020),
3. S. M. Teo, B. K. Ofori-Okai, C. A. Werley, K. A. Nelson, Invited Article: Single-shot THz detection techniques optimized for multidimensional THz spectroscopy. *Review of Scientific Instruments* **86**, 051301, DOI 10.1063/1.4921389 (2015).
4. G. D. Boreman, *Modulation transfer function in optical & electro-optical systems* (SPIE Press, Bellingham, Wash., USA, 2001).
5. D. H. McMahon, R. F. Cooper, W. A. Dyes, A. Mahapatra, W. C. Robinson, Echelon grating multiplexers for hierarchically multiplexed fiber-optic communication networks. *Applied Optics* **26**, 2188, DOI 10.1364/ao.26.002188 (1987).

*Chapter 6*AN ECHELON-BASED SINGLE-SHOT OPTICAL AND
TERAHERTZ KERR EFFECT SPECTROMETER

We report on the design and performance of an echelon-based single-shot visible/near-infrared spectrometer with adequate sensitivity to measure the nonlinear optical and terahertz Kerr effects in neat molecular liquids at room temperature. Useful molecular information spanning tens of picoseconds can be measured in just a few milliseconds, and the signal-to-noise performance scales favorably with respect to the standard stage scan technique. These results demonstrate the viability of stage-free nonlinear Kerr effect measurements and provide a route for improvements to the speed of future multi-dimensional Kerr effect studies.

This chapter has been reproduced with the permission of AIP Publishing from:

G. J. Mead *et al.*, An echelon-based single shot optical and terahertz Kerr effect spectrometer. *Review of Scientific Instruments* **90**, 053107, DOI 10.1063/1.5088377 (May 2019),

6.1 Introduction

Direct probes of ultra-fast molecular dynamics in liquids are of great interest to both experimentalists and theorists seeking to understand fundamental properties of chemical dynamics and energy transfer. Optical and terahertz Kerr effect (1D-OKE/1D-TKE) spectroscopies are particularly useful in this pursuit, offering sub-picosecond resolution of a liquid's response to a nonlinear perturbation [2, 3, 4]. While easily performed along one time dimension, Kerr effect spectroscopy can be extended to multiple time (frequency) dimensions, revealing fundamental couplings between low energy vibrational and librational modes [5, 6]. One root limitation in the speed of 1D-OKE/1D-TKE data acquisition is the need to use motorized delay stages which indirectly sample the molecular response in the time domain. While not a large impediment in one dimensional studies, scanning multiple delay lines in multi-dimensional experiments rapidly becomes a limiting factor, dictating some compromise between experimental duration, time (frequency) resolution, and sensitivity.

Generally, stage scan limitations have been overcome using specialized gratings, prisms, or spectrally chirped probe pulses. In conjunction with photodiode arrays, these multiplexing techniques can encode many picoseconds of molecular dynamics onto a degree of freedom that can be measured in a single, or a small number of laser shots. A large body of works have described the application of time-to-frequency, time-to-angle, and time-to-space multiplexing techniques to the linear analog of 1D-TKE, terahertz time domain spectroscopy (THz-TDS), and to studying irreversible processes and dynamics in optically excited materials [7, 8, 9, 10, 11, 12, 13, 14]. While these techniques are exceedingly useful for probing ultra-fast dynamics of a material's degradation or the profile of a terahertz waveform, we are interested in applying single-shot techniques to study Kerr effect phenomena in liquids. Although a few studies have used spectrally chirped probe pulses for single-shot 1D-OKE measurements of liquids, the application of other single-shot techniques is still very much under-investigated [15, 16].

In this paper, we describe the construction of a single-shot apparatus based upon a reflective stair step echelon which maps delay time onto the pixel space of a scientific CMOS (sCMOS) camera array. The design provides a 30 picosecond measurement window which can be recorded at a 1 kHz acquisition rate. This approach eliminates the use of a stage scan and can measure the 1D-OKE and 1D-TKE responses of simple liquids in as little as 10 milliseconds (10 laser shots).

The echelon technique also avoids fundamental limits in temporal resolution present in time-to-frequency mapping approaches [14]. We demonstrate good agreement between data recorded using the single-shot apparatus and the conventional stage scan approach. We further quantify the signal-to-noise scaling of the single-shot approach, and find favorable performance relative to using a stage scan. Overall, the performance achieved demonstrates the feasibility of using a reflective stair step echelon to detect nonlinear molecular Kerr effect signals, extending the utility of the reflective echelon technique beyond the well demonstrated linear electro-optic Pockels effect.

6.2 Experimental approach

Adapting previously reported designs, the probe beam passed through two reflective telescopes pairs, of which each provided a $8\times$ magnification of the probe beam [17, 18, 19]. An iris was also placed between the two telescope pairs to further improve the final beam profile homogeneity. The probe beam diameter after magnification is 50 mm, and so completely illuminates the 1000 step nickel echelon (step width = $35\ \mu\text{m}$; step depth = $5\ \mu\text{m}$). This echelon geometry provides 30 ps of total optical delay, with 30 fs of delay between adjacent ‘beamlets’. The reflected probe beam was then directed off a 50 mm diameter gold mirror before being focused with a Barlow lens combination through the hole in the third OAP. Immediately before passing through the OAP, the probe beam polarization was conditioned with a 10,000:1 preparatory polarizer and a quarter wave plate (QWP). The energy of the probe beam at this position was 600 nJ, and focused into an ellipse with a vertical $1/e^2$ radius spot of $73\ \mu\text{m}$. This corresponds to an average power density of $3.56\ \text{W}/\text{cm}^2$, which is several fold larger than the THz average power density. However, the probe power is not contained in a few hundred femtosecond pulse but across 30 picoseconds, which drops the instantaneous power density by several hundred fold (to on the order of $100\ \text{MW}/\text{cm}^2$, such that the THz pump power density is much greater than the probe power density).

The orientation of the probe and pump polarizations are aligned such that the measured 1D-OKE/1D-TKE signals arise from the anisotropic component of the molecular response function ($R_{aniso} \propto R_{XYXY}$) [20]. A traditional optical heterodyne detection scheme was employed to improve the strength of the Kerr effect signals [21]. The fast axis of the QWP was aligned parallel to the preparatory polarizer axis, and then the polarizer was slightly de-tuned ($\sim 2^\circ$) to introduce a small amount of orthogonally polarized light, which acquires from the QWP a $\pi/2$ phase shift

relative to the majority of the probe beam. This small quadrature component acts as a local oscillator during the heterodyne detection of the rotated probe light. When the local oscillator and signal fields arrive at the camera array, each square law detector (camera pixel) produces a signal proportional to the square of the two incident fields:

$$(E_{\text{LO}} + E_{\text{sig}})^2 = E_{\text{LO}}^2 + E_{\text{sig}}^2 + 2E_{\text{LO}}E_{\text{sig}} \quad (6.1)$$

This equation is a valid approximation for the single-shot measurements, where both the preparatory polarizer detuning angle and induced birefringence in the sample are small. The polarizer angle can be adjusted to ensure that the local oscillator background is always much greater than the Kerr effect response, which ensures the signal is dominated by the term in Eq. 1 that is linearly proportional to E_{sig} . The ultimate limit to the intensity of the local oscillator background is the well depth of the camera pixels. The probe intensity in these experiments corresponded to $\approx 3,000$ total photon counts per individual unbinned pixel per image (or 10,000 incident photons at a QE of 30% at 800 nm). This probe illumination intensity falls well within the linear photon counting regime of the camera, which has a linearity greater than 99% of the well depth of 30,000 e^- .

In 1D-OKE measurements, a 1mm path length Suprasil QS cuvette contained the sample, while for 1D-TKE measurements a $5 \times 5 \text{ mm}^2$ clear aperture, $1 \mu\text{m}$ thick silicon nitride window on a $10 \times 10 \text{ mm}^2$ Si substrate (Norcada) was epoxied in place over a glass cuvette with a 6.5 mm diameter hole drilled through one wall, creating an effective path length of 1.5 mm. After interacting with the pumped sample, the probe beam passed through a second 10,000:1 analyzing polarizer which was crossed at 90° with respect to the fast axis of the QWP. The probe beam then passes through two cylindrical imaging lenses and a 750 nm long pass filter before hitting the camera's sCMOS array. Proper imaging of the echelon surface onto the camera array is absolutely critical for ensuring good quality measurements. The imaging pathway, as well as specific properties and positions of the post-echelon Barlow and imaging lenses, is shown in Fig. 5.4.

Data were collected as described in section 5.6. For traditional Kerr effect studies using single element photo-diodes, the small nonlinear homodyne component can be removed in a few different ways: for example, through performing two measurements with the preparatory polarizer oriented at $\pm\phi$, or through measuring the difference

signal recorded by a pair of photo-diodes after passing through the sample and a series of post-sample polarization optics [22]. In contrast, the simultaneous measurement of E_{LO}^2 in the single-shot experiment allows E_{sig} to be numerically calculated using a single data set. Once determined, the heterodyne and homodyne component can be easily separated. (See Section 6.6 for more discussion of this process). For data throughout this study, the very small homodyne component was not removed from the stage scan or echelon data. Instead, we demonstrate the deconstruction of the echelon data into its homodyne and heterodyne components, thus verifying the necessary condition $E_{\text{LO}} \gg E_{\text{sig}}$.

To improve sensitivity, a 2 pixel horizontal bin and an 8 pixel vertical bin were applied to the 2560×80 pixel subarray of the camera used to acquire data. The 8 pixel vertical binning was aligned parallel to the long axis of the beamlets and so binning in this direction had no impact on the temporal resolution of the experiment. Co-adding along the vertical dimension produced a final data array of 1280×1 values. Accounting for small regions on each side of the camera array which were not illuminated by the probe beam, the 1000 echelon steps were imaged onto an area that horizontally spanned around 1100 2× binned pixels (or 2200 total pixels). This slight oversampling of the probe beamlets ensured that the temporal dynamics encoded by the probe were fully resolved by the camera.

Calibrating the pixel-to-time mapping was achieved by translating a delay stage on the probe beam path by 1.4989 mm (10 ps of delay), which resulted in the echelon signal peak shifting along the array by z pixels. (A similar calibration could easily be achieved without a delay line by using a small plate of material with a known thickness and index at 800 nm.) A cross-correlation between the $t=0$ ps and $t=10$ ps data sets calibrated the time axis, and time resolution per pixel was found to be ~ 28 fs. This provided a Nyquist-limited bandwidth of 17 THz. Unlike the stage scan technique whose Nyquist-limited bandwidth is easily tuned by changing the sampling rate and speed of the stage scan, the echelon measurements are less flexible due to the finite number of beamlets and detector elements.

While the Nyquist-limited sampling bandwidth set by the echelon imaging onto the sCMOS array is 17 THz, the group velocity dispersion introduced by optics along the probe beam path prior to the sample could reduce the bandwidth by broadening the probe pulse duration. To combat dispersion, the probe beam (initially 51.9 fs after being split from the main Legend beam) makes 6 reflections off of a pair of negative GVD mirrors immediately prior to the reflective telescope. This pre-

compensation effectively negates the dispersion introduced by two focusing lenses, polarizer, quarter wave plate, and sample cuvette. The final probe pulse duration immediately before the sample was estimated to be 56.8 fs, which sets the upper practical bandwidth at ~ 7.7 THz.

6.3 Results: Kerr effect measurements

The temporal resolution of the system was evaluated using dimethyl sulfoxide (DMSO), which has a 1D-OKE signal dominated by an instantaneous electronic response that follows the square of the optical pump electric field [16]. The stage scan and echelon methods were both used to measure the response of DMSO and produced nearly identical results (Fig. 6.1 A).

The full-width at half maximum of the DMSO response was measured to be 283.8 fs and 285.5 fs using the stage scan and echelon respectively. As demonstrated by the difference between the stage scan and echelon data (Diff, offset -0.2), good agreement between the two techniques is achieved, and confirms the echelon is imaged properly onto the sCMOS array. Transforming the DMSO data into the frequency domain reveals the echelon data has a signal-to-noise transition around 7.7 THz, with similar results from the stage scan data (Fig. 6.1 B)).

The small oscillations apparent in the difference between the DMSO data prompted further investigation. To completely remove any molecular orientational response, the empty Suprasil quartz cuvette was directly measured using the two techniques by shifting the focal region from the cuvette volume to the cuvette wall (Fig 6.1 C). While the instantaneous 1D-OKE response is similar between the two techniques (FWHM echelon = 299.5 fs, FWHM stage = 280.9 fs), diffraction patterns in the echelon data are visible. The diffraction signal is visible only in the echelon data because the camera provides far greater spatial resolution than a single photo-diode. The sinc-like shape of the diffraction pattern is attributed to the probe beam passing through the 3 mm circular aperture in the third OAP. While such diffraction occurs with radial symmetry in the direction of probe propagation, binning and co-adding along the vertical axis results in only diffraction along the horizontal axis of the camera array being resolved.

The aperture diameter responsible for the diffraction artifacts can be calculated using the pixel length, distance from OAP surface to camera array, and the magnification factors contributed by the lenses. Applying the standard relationship $\theta_0 = 1.22\lambda/D$ between the photon wavelength, λ , and the angle formed between the diffraction

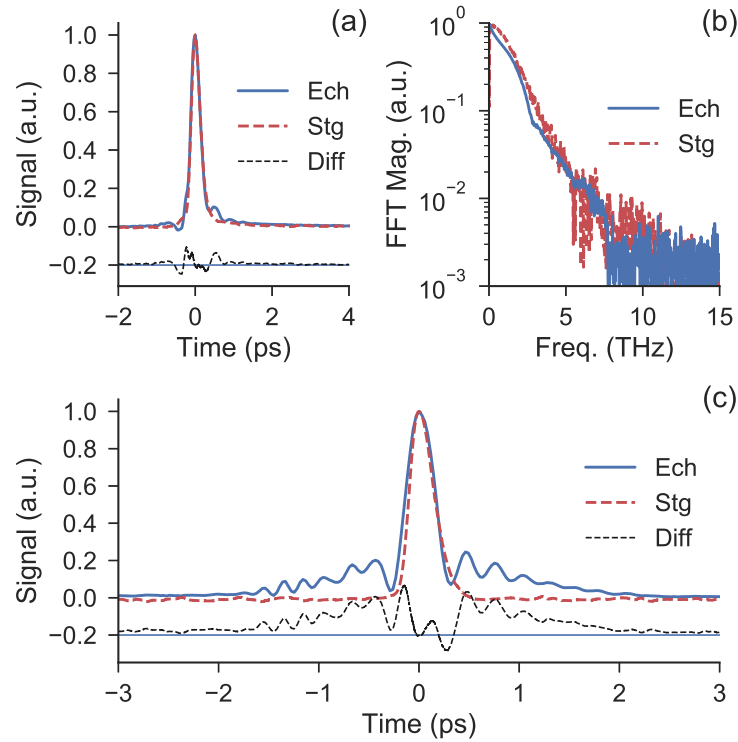


Figure 6.1: A) Comparison of the 1D-OKE responses of DMSO measured using the stage scan (Stg) and echelon (Ech) techniques. Diff is the subtraction of the stage scan data from the echelon data, on the same scale and offset -0.2. B) The FFT of the stage and echelon DMSO data demonstrate similar bandwidths and noise floors. C) Same as in A), but the 1D-OKE response of the Suprasil quartz cuvette. The diffraction features are clearly apparent around the main 1D-OKE response at $t=0$ ps.

maxima and first minima, θ_0 , returns an estimated aperture diameter of 7.2 mm. This is in reasonable agreement with the 3 mm diameter opening in the OAP, especially given errors that can be introduced from estimating the very small angle θ_0 (which is only on the order of ten thousandths of a radian).

While diffraction from the OAP aperture is always present in every image acquired by the camera, probe photons rotated by the nonlinear perturbation in the sample allows an excess number of diffracted photons to accumulate in the pump-on image subset, which subsequently cannot be removed during data processing. Fortunately, these artifacts have a known functional form, and so are amenable to removal by deconvolution techniques. Minimization of the probe beam diameter prior to passage through the OAP aperture would further mitigate these diffraction effects.

Diffraction from passage of the probe beam through the nonlinear aperture created by the pump field in the sample was also considered. However, the pump electric field cross-section is Gaussian, and thus should produce a non-linearly perturbed region in the sample that also follows a Gaussian distribution. This Gaussian aperture would subsequently yield a Gaussian diffraction pattern which would not produce the oscillatory side-lobes observed in the data. This qualitative observation, coupled with the good agreement between actual and calculated aperture diameters, supports the OAP hole as the source of the weak diffraction artifacts.

Next, the single-shot apparatus was used to measure the 1D-OKE and 1D-TKE responses of carbon disulfide (CS_2). For the single-shot experiments, 10,000 images spanning 30 ps of delay were acquired in 10 seconds, while the stage scan required ~ 18 seconds (18,000 shots) at $250 \mu\text{m/s}$ to acquire the same 30 ps of data. The third order nonlinear constant of CS_2 is much larger than DMSO ($\text{CS}_2 \text{Re}\chi^{(3)} = 93.17 \times 10^{-24} \text{ m}^2/\text{V}^2$ cf. $\text{DMSO Re}\chi^{(3)} = 14.22 \times 10^{-24} \text{ m}^2/\text{V}^2$), and the Kerr effect signals are characterized by a slowly decaying molecular orientational response that extends for many picoseconds after the instantaneous electronic response maximum [23, 24]. As seen in Fig. 6.2 A and B, the 1D-OKE and 1D-TKE responses of CS_2 are captured with good fidelity using both techniques. Differences in the optical and terahertz Kerr effect responses arise from different contributions from the polarizability and dipole moment operators in the third order response function [6]. The good agreement between techniques is especially promising when the difference in instantaneous probe photon flux between the two methods is considered. While the entire photon flux is contained within the probe pulse duration using the stage scan method, the echelon disperses the same total number of photons over a 30 ps window, reducing the instantaneous photon flux interacting with the sample by roughly two orders of magnitude.

To examine the quality of the single-shot signal as a function of the number of averages, we extracted from the CS_2 $N=10,000$ shot data subsets ranging from $N=5,000$ to $N=10$ shots. In Fig. 6.2 C and D the Kerr effect responses of CS_2 across 4 orders of magnitude of sampling are shown. After 10 shots are acquired the decaying 1D-OKE and 1D-TKE responses out to several ps are already clearly present. Further sampling extends the decaying response in time and reduces noise. In contrast to the 30 ps of data acquired by the echelon, a stage scan measurement at an equivalent Nyquist-limited bandwidth of 17 THz could only collect around a quarter picosecond of data in 10 milliseconds (optimistically assuming no limitations

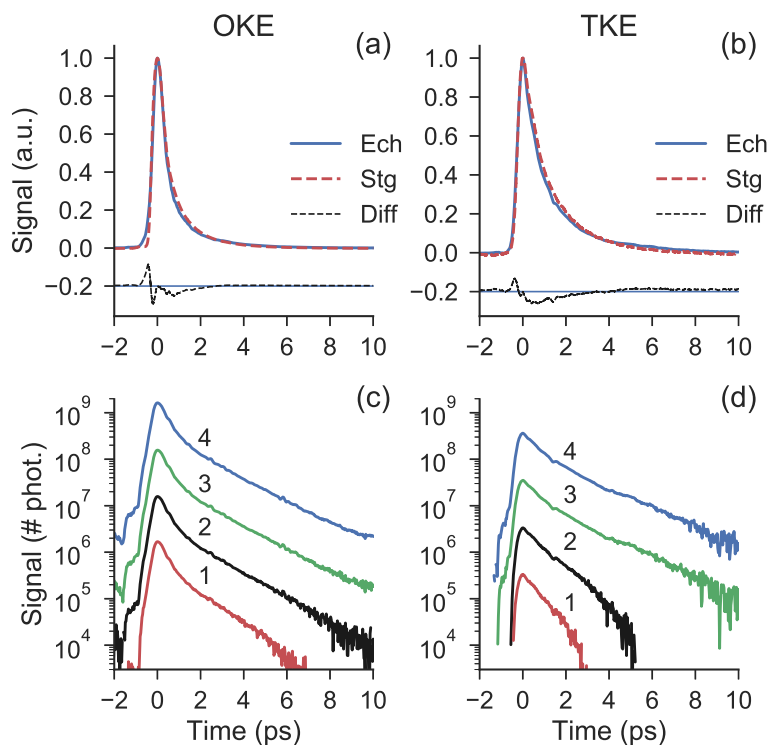


Figure 6.2: A) Linear plots of the CS₂ 1D-OKE signal recorded with the echelon (Ech) and stage scan (Stg) techniques as well as the difference between the two (Diff, -0.2). Good agreement between the two techniques is apparent out to $t=10$ ps. B) Similar to A), but demonstrating the 1D-TKE response of CS₂. C) Evolution of the noise in the single-shot CS₂ 1D-OKE data across 4 orders of magnitude of sampling ($N=10^x$ shots, $x = 1, 2, 3, 4$). D) The same analysis as in C), but for the 1D-TKE response of CS₂.

are imposed by the mechanics of the delay stage).

Finally, we measured the 1D-OKE response of bromoform (CHBr₃) with the single-shot apparatus. Bromoform is a halogenated methane with two low frequency vibrational modes. The full 1D-OKE response of bromoform is seen in Fig. 6.3 A, with the inset highlighting the oscillatory molecular coherences in the data. After detrending a double exponential decay from the data (Fig 6.3 A inset, dashed red line), the residual was Fourier transformed, with two strong features confirming the presence of the molecular modes at 4.66 THz (ν_6 , lit. 4.64 THz) and 6.73 THz (ν_3 , lit 6.68 THz), the later of which is at the upper bounds of the practical experimental bandwidth [25]. With the optical pump non-resonant with these two modes, only a nonlinear two-photon Raman process can be responsible for the detection of these

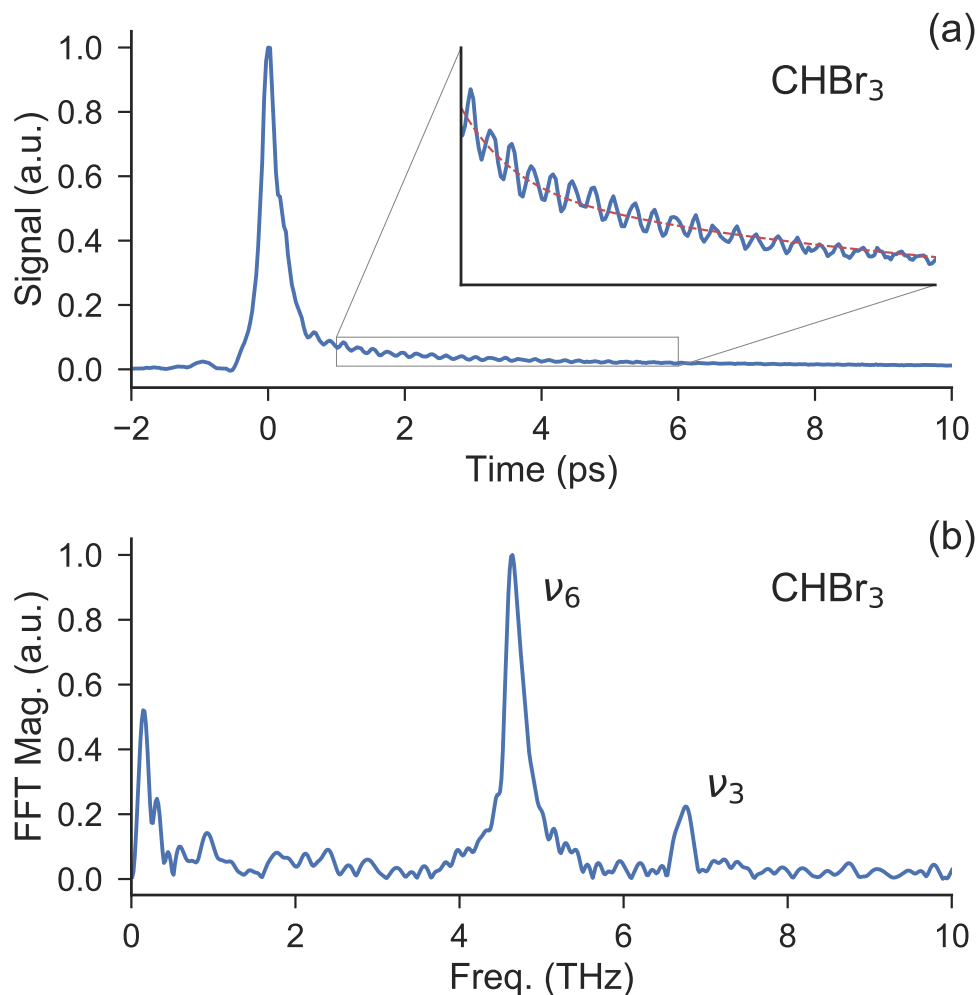


Figure 6.3: A) Bromoform 1D-OKE response measured using the echelon approach ($N=10,000$ shots). The oscillatory molecular coherences are shown in the inset, along with the orientational response fit. B) The Fourier transform of the fit residual reveals the ν_6 and ν_3 Raman-active modes of bromoform.

features. Similar molecular coherences were observed in diiodomethane (CH₂I₂), with the 3.65 THz (ν_4 , lit. 3.65 THz) mode clearly visible [26]. Dichloromethane, which has a Raman active mode at 8.5 THz was also measured but no coherences were observed, a finding consistent with the bandwidth limitations imposed by the probe beam duration.

6.4 Results: Sensitivity and noise performance

The signal-to-noise characteristics of the echelon technique were quantified by calculating the root-mean-square (RMS) noise in the 1D-OKE response of a series

Molecule	$\Re(\chi^{(3)})$ [pm ² /V ²]
acetonitrile (ACN)	6.61
acetone	10.46
dimethylsulfoxide	14.22
nitrobenzene	21.02
benzene	34.34
carbon disulfide (CS ₂)	93.17

Table 6.1: Liquids with varying $\chi^{(3)}$ magnitudes screened with 1D Kerr effect spectrometer

of solvents, and comparing these values to that of stage scan data. The solvents are listed in Table 6.1 and were chosen to span a broad range of $\chi^{(3)}$ values, which is directly proportional to the magnitude of the Kerr response of the liquid [23].

For each liquid, the mean-corrected percent RMS ($\% \sigma$) of a 3 ps region of the data before the molecular signal was calculated and normalized to the peak of the molecular signal. Comparison data were also acquired using the stage scan method. To keep the information content of the two techniques consistent, the sampling rate of the data acquisition card used for stage scan measurements was adjusted such that the Nyquist-limited bandwidth was 17 THz. All stage scans collected 30 ps of data, while the stage scan velocity was adjusted to change the number of laser shots acquired in the data sets.

Across the range of weakly to strongly 1D-OKE-active liquids, the echelon data had a linear, $1/\sqrt{N}$ relationship between $\log(N)$ and $\log(\% \sigma)$. The RMS performance for 1D-OKE measurements of acetonitrile and carbon disulfide are shown in Fig. 6.4 A. The $1/\sqrt{N}$ scaling was constant across 4 orders of sampling magnitude, as demonstrated by the line of best fit. Thus, random Gaussian noise appears to be the predominant noise source in the echelon data. A weaker relationship between the number of shots and the stage scan $\% \sigma$ was found, indicating the data were limited by correlated noise in the measurement and were approaching the noise floor of the stage scan technique for the given experimental parameters.

Next, the RMS performance of the CS₂ 1D-TKE response was measured using both the echelon and stage scan techniques. The RMS behaviors of the two techniques were equivalent in the 1D-OKE and 1D-TKE experiments, although the 1D-TKE response was overall weaker, requiring more measurements to achieve the same RMS noise (Fig. 6.4 B). A major cause of the weaker 1D-TKE response was the lower terahertz pump energy. For example, at $N=10,000$ shots, the measured

difference in $\log(\% \sigma)$ between 1D-TKE and 1D-OKE echelon measurements was 0.88. Given that the Kerr effect signal scales linearly with the pump power ($\text{Watts} \propto I = |E^2|$), a difference in $\log(\% \sigma)$ of 1.7 was calculated based upon the ratio of the optical and terahertz pump energies ($1.7 = \log(31 / 0.6 [\text{W}/\text{cm}^2])$), which agrees well with experiment considering the difficulty in measuring the THz pump power with the same precision as the 1D-OKE pump power.

A clear trend was observed in the performance of the two techniques across the range of solvents measured with 1D-OKE. In Fig 6.4 C, the $\log(\% \sigma)$ after accumulating 10,000 shots was plotted against the logarithm of the third order nonlinear susceptibility $\chi^{(3)}$ of each solvent. While solvents with weaker 1D-OKE responses tend to reach similar noise floors after 10,000 shots, irrespective of the measurement technique used, the echelon measurements consistently reach lower RMS values for even moderately 1D-OKE active liquids.

Finally, the sensitivity of the echelon technique was also investigated. For each solvent measured, the total number of signal photons (given by the difference between pump on and pump off data sets) was normalized by the total number of photons in the pump off data set. An identical analysis was performed using a data set with the pump beam blocked, which measures the random error in background photon subtraction for a given probe intensity, and provides a measure of the absolute noise floor of the experiment. As shown in Fig 6.4 D, even the weakest 1D-OKE response corresponding to a modulation on the order of 0.1% was orders of magnitude larger than the absolute experimental noise floor, which was around 0.001%.

6.5 Results: Stage-scan vs. echelon 1D-OKE responses

The six solvents measured using the single-shot echelon and stage scan techniques are shown below in Fig 6.5, with the difference (same scale, offset -0.2) between the two data sets shown to demonstrate the degree of agreement between the two techniques. Some small diffraction artifacts and irregularities are present in the electronic response regime, which is defined as the few hundred femtosecond region around the signal maximum. The longer picosecond scale molecular orientational responses were found to agree well between the two techniques.

6.6 Results: Heterodyne and homodyne components of the Kerr effect signal

The single-shot 1D-OKE responses of the six solvents measured in this study were decomposed into heterodyne and homodyne components using an algebraic solver written in Python. First, the difference signal Y and background signal E_{LO}^2 were

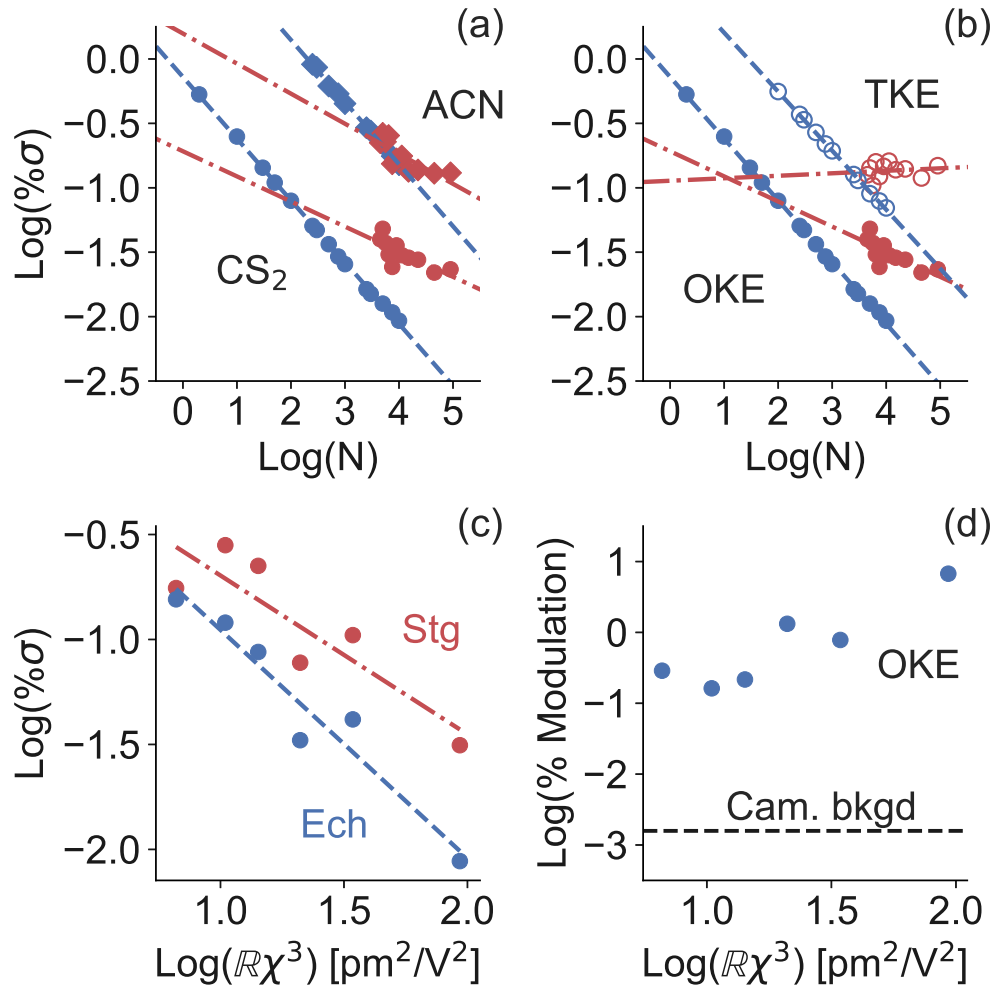


Figure 6.4: A) The RMS scaling of 1D-OKE signals from two solvents, acetonitrile (ACN, diamonds) and carbon disulfide (CS_2 , circles), recorded using the echelon (blue) and stage scan (red) techniques. B) Comparison between the RMS noise performance of the two techniques in the 1D-OKE (filled markers) and 1D-TKE responses (empty markers) of CS_2 . While substantially weaker than 1D-OKE, 1D-TKE measurements obey similar trends in RMS. C) The 1D-OKE RMS achieved after $N=10,000$ shots for a series of solvents, ranging from weakly to strongly Kerr active (plotted here as small to large $\chi^{(3)}$ constants). D) The ratio of 1D-OKE signal photons to background photons (% modulation) observed in the same range of solvents as in C). The noise floor from random photon fluctuations with no pump present is shown as the dashed horizontal line.

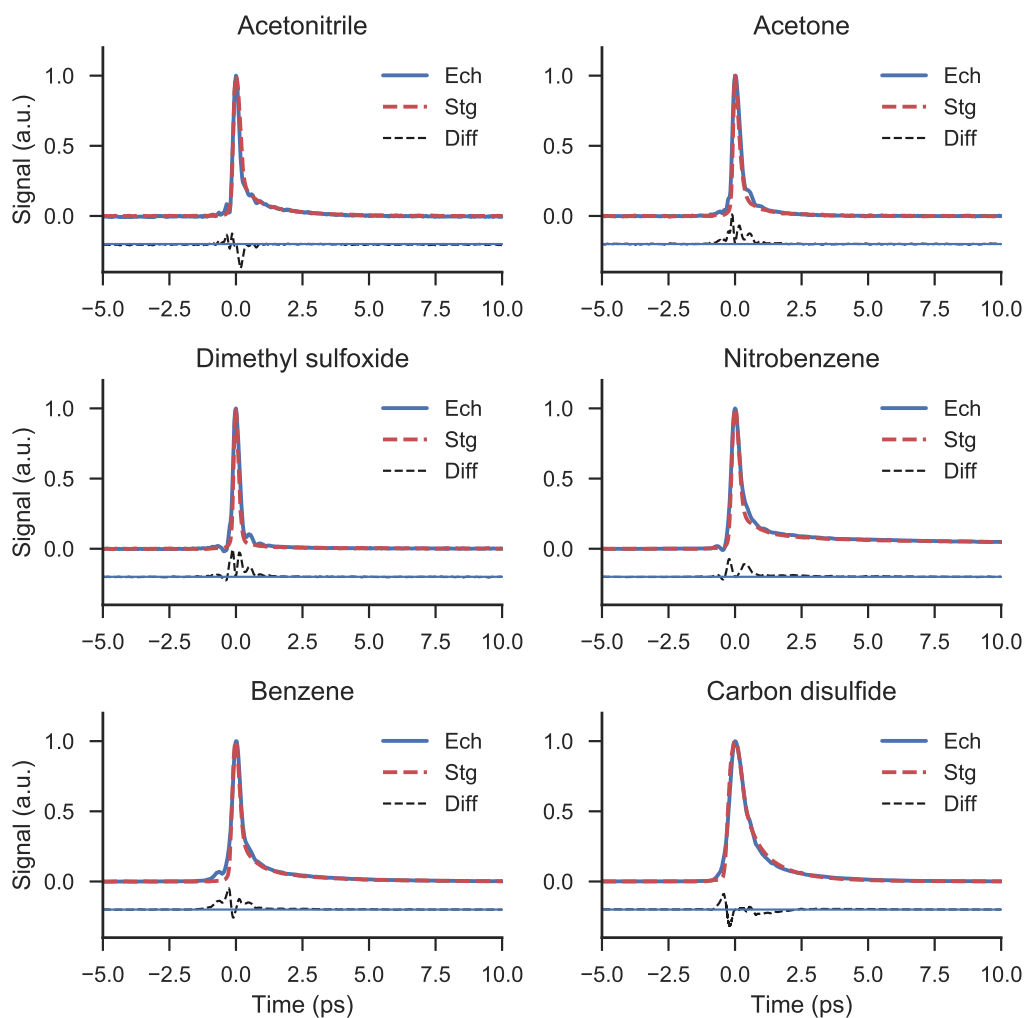


Figure 6.5: Comparison plots of the six solvents investigated by 1D-OKE, demonstrating the good agreement between the two techniques across a range of response profiles. The echelon data consist of 10,000 laser shots (10 seconds), the stage scan data 45,000 laser shots (45 seconds).

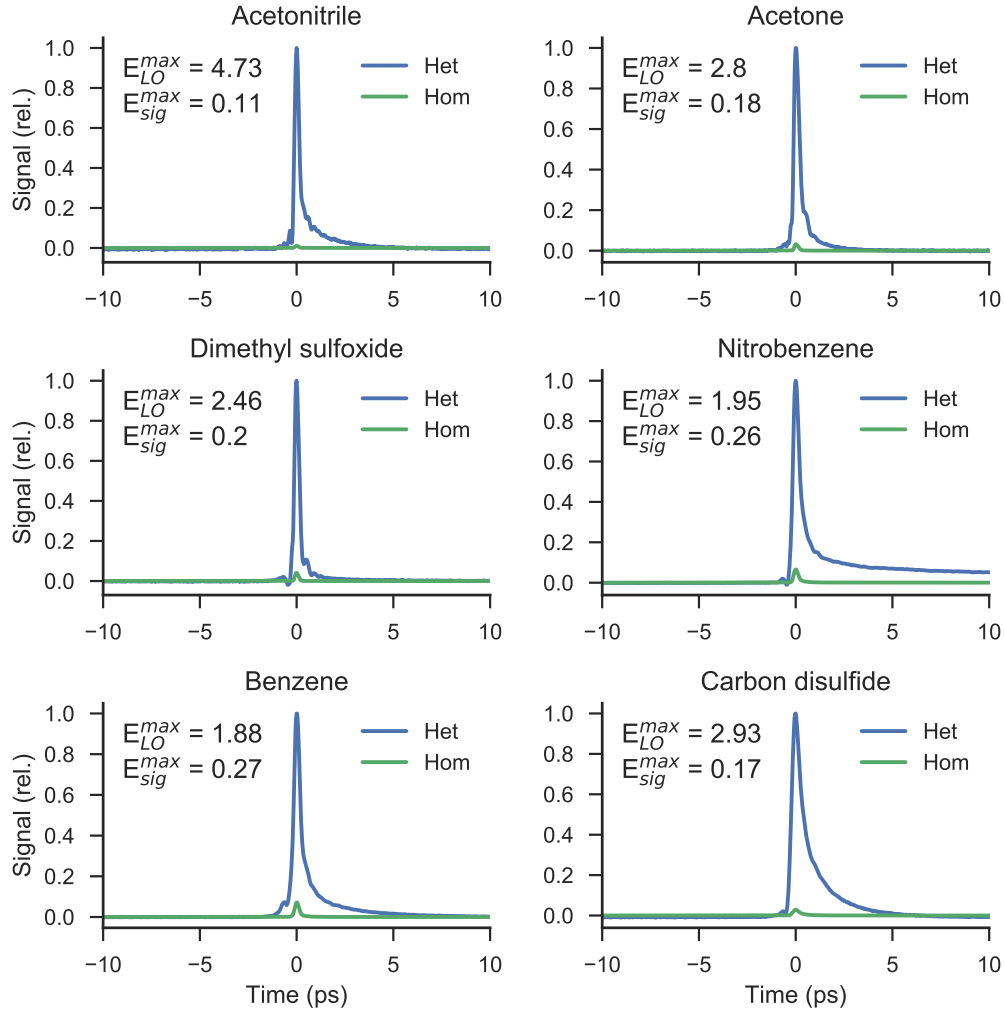


Figure 6.6: The heterodyne and homodyne components of the single-shot 1D-OKE responses of six solvents investigated in this study. The values in the upper left-hand corners specify the maximum relative magnitudes of the calculated E_{LO} and E_{sig} fields, demonstrating the $E_{LO} \gg E_{sig}$ condition for linear heterodyne detection.

extracted from the $N=10,000$ shot data set. These two 1280×1 vectors were then used as inputs to a Python symbolic solver which found the roots X to Eq. 4, where $X = E_{sig}$. In Fig 6.6, the heterodyne and homodyne components are shown for each solvent.

$$Y - X^2 + 2XE_{LO} = 0 \quad (6.2)$$

6.7 Conclusions

A single-shot, reflective echelon spectrometer design has been shown to acquire accurate 1D-OKE and 1D-TKE data of simple liquids, and has sufficient sensitivity to record tens of picoseconds of molecular signal in as few as 10 laser shots (10 ms). Furthermore, the detection of Raman-active molecular coherences in simple halogenated methanes is especially promising for future applications of the echelon technique to multi-dimensional nonlinear spectroscopies. Finally, the noise performance of the echelon approach is found to be very competitive to the standard stage scan technique. In sum, these results highlight the feasibility of stage-free nonlinear spectroscopic measurements with orders-of-magnitude faster acquisition times.

As the technique is developed further, a series of questions remain to be explored. In particular, how strongly does the data quality depend upon the camera frame rate and pixel linearity? Do nonlinear measurements require a more quantitative camera than is required for linear THz absorption spectroscopy? Depending upon which data are found to be relatively robust to these parameters, then the methodology outlined above could perform well with a broader set of commercially available cameras, providing a reasonable alternative to motorized stages for performing high resolution nonlinear spectroscopy.

BIBLIOGRAPHY

1. G. J. Mead, I. Katayama, J. Takeda, G. A. Blake, An echelon-based single shot optical and terahertz Kerr effect spectrometer. *Review of Scientific Instruments* **90**, 053107, DOI 10.1063/1.5088377 (May 2019),
2. P. Bartolini, A. Taschin, R. Eramo, R. Torre, in *Time-resolved spectroscopy in complex liquids: An experimental perspective*, pp. 73–127, DOI 10.1007/978-0-387-25558-3.
3. M. C. Hoffmann, N. C. Brandt, H. Y. Hwang, K. L. Yeh, K. A. Nelson, Terahertz kerr effect. *Applied Physics Letters* **95**, ISBN: 0003-6951, 231105, DOI 10.1063/1.3271520 (2009).
4. M. A. Allodi, I. A. Finneran, G. A. Blake, Nonlinear terahertz coherent excitation of vibrational modes of liquids. *Journal of Chemical Physics* **143**, ISBN: 0831040831, 234204, DOI 10.1063/1.4938165 (2015).
5. P. Hamm, J. Savolainen, Two-dimensional-Raman-terahertz spectroscopy of water: Theory. *Journal of Chemical Physics* **136**, 20402, DOI 10.1063/1.3691601 (2012).
6. I. A. Finneran, R. Welsch, M. A. Allodi, T. F. Miller III, G. A. Blake, Coherent two-dimensional terahertz-terahertz-Raman spectroscopy. *Proceedings of the National Academy of Sciences* **113**, 6857–6861 (2016).
7. P. R. Poulin, K. A. Nelson, Irreversible organic crystalline chemistry monitored in real time. *Science* **313**, 1756–1760, DOI 10.1126/science.1127826 (2006).
8. H. Sakaibara, Y. Ikegaya, I. Katayama, J. Takeda, Single-shot time-frequency imaging spectroscopy using an echelon mirror. *Optics Letters* **37**, 1118, DOI 10.1364/ol.37.001118 (2012).
9. Y. Minami, H. Yamaki, I. Katayama, J. Takeda, Broadband pump-probe imaging spectroscopy applicable to ultrafast single-shot events. *Applied Physics Express* **7**, 022402, DOI 10.7567/APEX.7.022402 (2014).
10. J. Takeda, W. Oba, Y. Minami, T. Saiki, I. Katayama, Ultrafast crystalline-to-amorphous phase transition in Ge₂Sb₂Te₅ chalcogenide alloy thin film using single-shot imaging spectroscopy. *Applied Physics Letters* **104**, 261903, DOI 10.1063/1.4886969 (2014).
11. M. Kobayashi *et al.*, High-acquisition-rate single-shot pump-probe measurements using time-stretching method. *Scientific Reports* **6**, Publisher: Nature Publishing Group, 37614, DOI 10.1038/srep37614 (2016).

12. T. Kuribayashi, T. Motoyama, Y. Arashida, I. Katayama, J. Takeda, Anharmonic phonon-polariton dynamics in ferroelectric LiNbO₃ studied with single-shot pump-probe imaging spectroscopy. *Journal of Applied Physics* **123**, 174103, DOI 10.1063/1.5021379 (2018).
13. Y. Minami, Y. Hayashi, J. Takeda, I. Katayama, Single-shot measurement of a terahertz electric-field waveform using a reflective echelon mirror. *Applied Physics Letters* **103**, 51103, DOI 10.1063/1.4817011 (2013).
14. S. M. Teo, B. K. Ofori-Okai, C. A. Werley, K. A. Nelson, Invited Article: Single-shot THz detection techniques optimized for multidimensional THz spectroscopy. *Review of Scientific Instruments* **86**, 051301, DOI 10.1063/1.4921389 (2015).
15. P. Georges, A. Brun, G. Roger, G. Le Saux, F. Salin, Single shot measurement of the optical Kerr effect kinetics. *Applied Optics* **27**, ISBN: doi:10.1364/AO.27.000777, 777, DOI 10.1364/ao.27.000777 (2009).
16. J. Zhang *et al.*, Ultrafast single-shot measurement of optical Kerr effect based on supercontinuum pulse. *Review of Scientific Instruments* **87**, ISBN: 9780494467343, 43114, DOI 10.1063/1.4947257 (2016).
17. P. Hello, C. N. Man, Design of a low-loss off-axis beam expander. *Applied Optics* **35**, ISBN: 9781479934386 Publisher: OSA, 2534, DOI 10.1364/ao.35.002534 (May 2008).
18. L. Yan *et al.*, Multi-frame observation of a single femtosecond laser pulse propagation using an echelon and optical polarigraphy technique. *IEEE Photonics Technology Letters* **25**, ISBN: 1041-1135, 1879–1881, DOI 10.1109/LPT.2013.2278883 (2013).
19. G. T. Noe *et al.*, Single-shot terahertz time-domain spectroscopy in pulsed high magnetic fields. *Optics Express* **24**, 30328, DOI 10.1364/oe.24.030328 (2016).
20. M. Khalil, O. Golonzka, N. Demirdöven, C. J. Fecko, A. Tokmakoff, Polarization-selective femtosecond Raman spectroscopy of isotropic and anisotropic vibrational dynamics in liquids. *Chemical Physics Letters* **321**, ISBN: 0009-2614, 231–237, DOI 10.1016/S0009-2614(00)00314-6 (2000).
21. Q. Zhong, J. T. Fourkas, Optical kerr effect spectroscopy of simple liquids. *Journal of Physical Chemistry B* **112**, ISBN: 1520-6106, 15529–15539, DOI 10.1021/jp807730u (2008).
22. J. Degert, M. Cornet, E. Abraham, E. Freysz, Simple and distortion-free optical sampling of terahertz pulses via heterodyne detection schemes. *Journal of the Optical Society of America B* **33**, 2045, DOI 10.1364/josab.33.002045 (2016).

23. K. Iliopoulos *et al.*, Ultrafast third order nonlinearities of organic solvents. *Optics Express* **23**, ISBN: 1094-4087, 24171, DOI 10.1364/oe.23.024171 (2015).
24. I. A. Heisler, R. R. B. Correia, T. Buckup, S. L. S. Cunha, N. P. da Silveira, Time-resolved optical Kerr-effect investigation on CS₂ / polystyrene mixtures. *Journal of Chemical Physics* **123**, 054509, DOI 10.1063/1.1994850 (2005).
25. M. Fernández *et al.*, The force field of bromoform: A theoretical and experimental investigation. *The Journal of Physical Chemistry* **100**, 16058–16065, DOI 10.1021/jp960750o (2002).
26. T. J. Johnson, T. Masiello, S. W. Sharpe, The quantitative infrared and NIR spectrum of CH₂I₂ vapor: vibrational assignments and potential for atmospheric monitoring. *Atmospheric Chemistry and Physics* **6**, 2581–2591 (2006).

Chapter 7

SUM-FREQUENCY SIGNALS IN 2D-TERAHERTZ-TERAHERTZ-RAMAN SPECTROSCOPY OF HALOGENATED METHANE LIQUIDS

We demonstrate that halogenated methane 2D-Terahertz Terahertz Raman (2D-TTR) spectra are determined by the complicated structure of the instrument response function (IRF) along ω_1 and by the molecular coherences along ω_2 . Experimental improvements have helped increase the resolution and dynamic range of the measurements, including accurate THz pulse shape characterization. Sum-frequency excitations convolved with the IRF are found to quantitatively reproduce the 2D-TTR signal. A new Reduced Density Matrix model which incorporates sum-frequency pathways, with linear and harmonic operators fully supports this (re)interpretation of the 2D-TTR spectra.

Adapted with permissions from:

G. J. Mead *et al.*, Sum-Frequency Signals in 2D-Terahertz-Terahertz-Raman Spectroscopy. en, *J. Phys. Chem. B*, acs.jpcc.0c07935, DOI 10.1021/acs.jpcc.0c07935 (Sept. 2020),

7.1 Introduction

Observing interactions within the low-frequency, thermally populated continuum of bath states is critical to developing a molecular understanding of liquid dynamics at room temperature. This energy regime is predominantly characterized by broad inter-molecular modes with short coherence times (~ 100 fs) which complicate the measurement and interpretation of potential energy, dipole and polarizability surfaces. One exception to this general observation are the intra-molecular vibrational modes of the halogenated methane (HM) family of liquids, whose well-defined coherent vibrational signals have long been observed in optical Kerr effect (OKE) experiments [2, 3].

Multidimensional time-resolved spectroscopy methods seek to disentangle the molecular processes underlying the low-frequency spectral features by introducing an additional time delay which separates dynamics along a second axis. The 5th order Raman technique [4] extends OKE to two dimensions and provides information on electrical and mechanical anharmonicities of the liquid, but practical implementation of this method is quite challenging [5, 6]. A trio of 3rd order terahertz-Raman hybrid spectroscopies have been proposed as alternatives to 5th order Raman spectroscopy that avoid some technical challenges inherent to 5th order spectroscopy [7, 8, 9, 10, 11, 12]. However, new challenges emerge in the hybrid techniques, especially compared to the more common 2D-infrared (2D-IR) spectroscopy, in which molecular coherences and population states are manipulated through electric dipole-allowed transitions. First, there are no commercially available dispersive THz spectrometers with adequate sensitivity to directly detect the emitted THz signal in THz-Raman-THz (2D-TRT) and Raman-THz-THz (2D-RTT) measurements. Instead, the 2D-TRT/RTT techniques have used time-domain electro-optic sampling to capture the faint THz emission [13]. 2D-TTR avoids this step by using a Raman probe pulse which generates an easily detected near-IR signal photon.

The Raman probe does mean, however, that the resonant excitation of coherences with the THz pulses in TTR experiments is driven by nonlinearities in the transition dipole surface, as we outline below. Further, in all the cases of hybrid THz-Raman spectroscopies, the poorly defined wave vector resulting from sub-cycle THz pulses precludes a phase-matching box-CARS style geometry that could be used to discriminate between signals originating from different quantum mechanical coherence pathways.

With 2D-TTR spectroscopy, complex spectra have been observed in several halo-

generated methane (HM) liquids, and were interpreted as signatures of coherent energy transfer pathways between intra-molecular vibrational modes [14, 15, 16, 17]. In this work, we present a thorough re-investigation of two HM liquids – bromoform (CHBr_3) and chloroform (CHCl_3) – which casts doubt on this original interpretation. Our new investigation is enabled by the development of a single-shot 2D-TTR spectrometer[18] which records tens of picoseconds of molecular dynamics in a single acquisition. From the order of magnitude speed-up, the new technique provides substantially higher signal-to-noise data which has allowed a much larger region of the molecular response to be measured, and at finer resolution.

We demonstrate through experiment, models, and theoretical simulations that the features observed in the HM 2D-TTR spectra arise from convolutions between the instrument response function (IRF) and linear interactions with the molecular polarizability operator \hat{I} . This interaction requires a scattering with two instantaneous THz photons, and is therefore referred to throughout the text as a sum-frequency (SF) excitation process. (Recent theoretical and experimental works have also observed efficient phonon excitation through the same linear- \hat{I} interaction with two THz field interactions [19, 20, 21].) Resonant nonlinear interactions with the transition dipole operator \hat{M} , while also in principal weakly allowed, are not seen.

7.2 Experimental approach

Data were collected as described in Section 5.6. Bromoform was purchased from Sigma Aldrich. As received the liquid had a orange hue, indicating some degradation and contamination from water. A simple distillation under nitrogen at 150 degree Celsius was performed to purify the bromoform liquid. NMR analysis indicated complete removal of water. The purified sampled was stored in a round-bottom flask with dry sodium sulfate, under argon in a dark refrigerator. Chloroform was purchased from Sigma Aldrich and used as received.

Terahertz Kerr effect measurements were taken of bromoform and chloroform, and the 2D-TTR response of diamond was measured to gauge the bandwidth of the THz pump fields [16]. As shown in Fig. 7.1, the THz electric field bandwidth is centered at 4 THz. Bromoform’s two Raman-active vibrational modes are observed at 4.7 and 6.6 THz, while the Raman-active vibrational mode in chloroform was observed at 7.8 THz. Note that the orientational (low-frequency) response of both liquids was removed prior to taking the FFT, and only the higher frequency spectral content arising from intra-molecular vibrations are seen in Fig. 7.1.

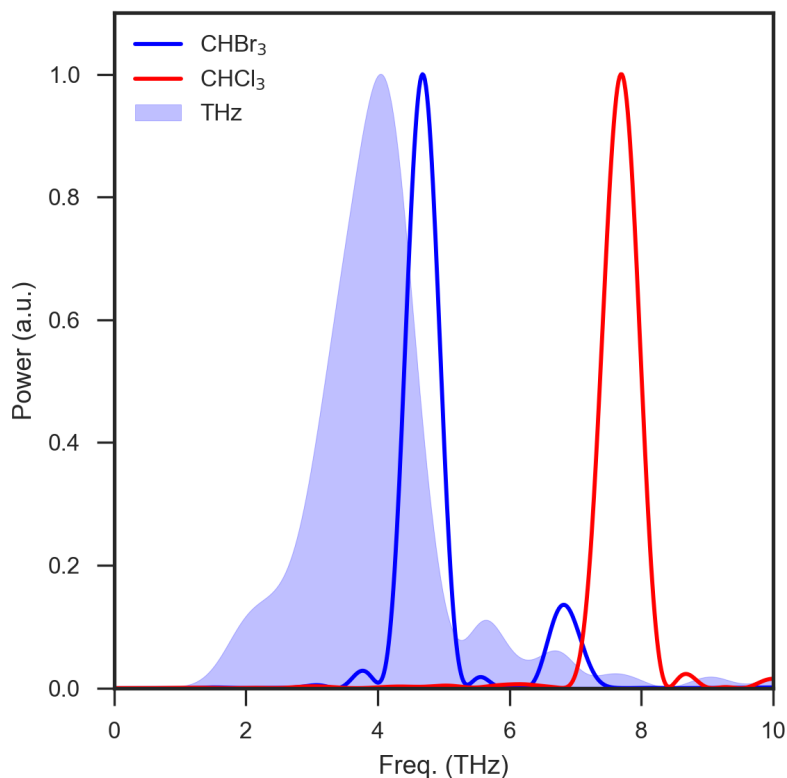


Figure 7.1: Bromoform and chloroform intramolecular vibrational responses are detected in 1D-TKE measurements. The THz bandwidth of the DAST emission as measured in diamond is shown in blue shading.

We begin by re-examining the relative importance of the M (resonant) and Π (sum-frequency) excitation pathways in HM vibrational modes. Ladder diagrams in Fig. 7.2 illustrate the two competing pathways as well as the OKE process. While analogous to SF-TKE, OKE measurements involve virtual states that are typically far removed from either electronic or fundamental vibrational states. SF-TKE processes, in contrast, involve photons that can directly excite intermolecular degrees of freedom in the liquid.

In order to observe the desired nonlinear THz signal, the resonant pathway must have a larger or (at least) comparable magnitude with the sum-frequency pathway. This is a difficult condition to satisfy in HMs since the resonant process is nonlinear with respect to M while the sum-frequency pathway is linear in Π .

Sum-frequency and resonant excitation pathways have distinct t_1 responses. A clear sign of resonant M interactions is a prolonged vibrational response along t_1 which arises from the generation of a vibrational coherence during the first THz

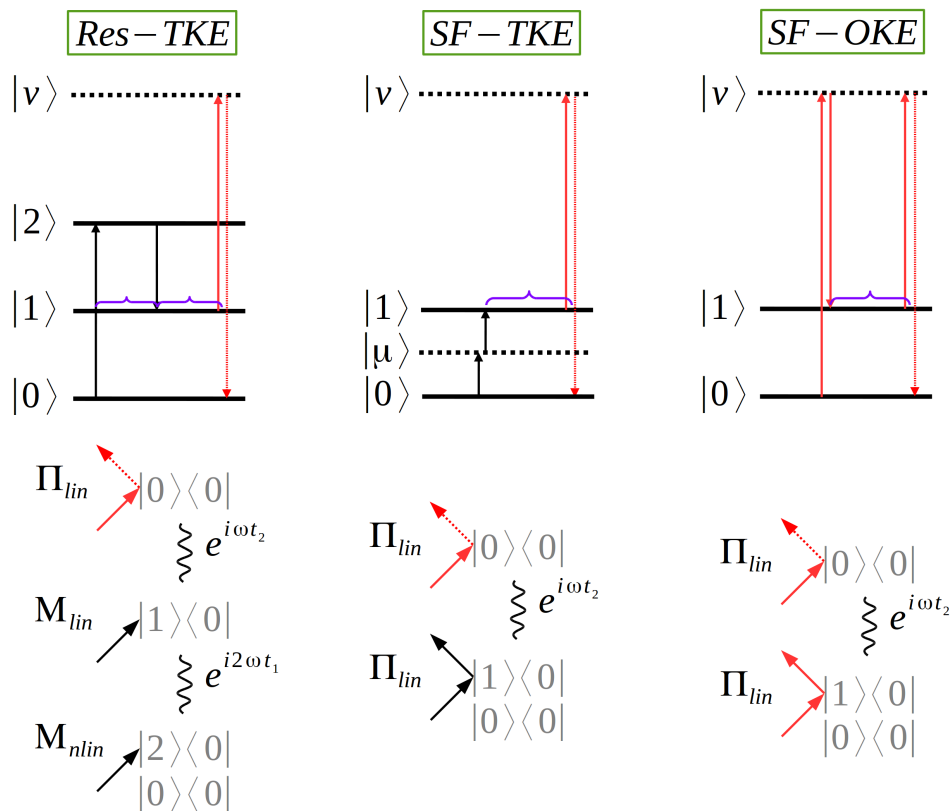


Figure 7.2: A resonant TTR signal requires dipole nonlinearities to excite a vibrational coherence – a representative process is depicted in the Res-TKE (resonant THz Kerr Effect) ladder and Feynman diagrams. In contrast, a sum-frequency excited molecular coherence is produced via interactions linear in the polarizability operator. The virtual state in SF-TKE is short-lived, thus the signal is highly dependent upon overlap between the two pump pulses. The familiar optical Kerr effect (SF-OKE) illustrates the similarities with SF-TKE.

field interaction. From 2D-TTR measurements, molecular coherences extending in excess of 5 ps along t_2 have been observed in HMs [15], suggesting a resonant signal should have a commensurate lifetime along t_1 . In contrast, sum-frequency excitation cannot directly generate coherent states through a single field interaction, but requires two instantaneous interactions. In this case, the extent of a molecular response along t_1 will be determined by the duration of temporal overlap of the two THz electric field waveforms.

In Fig. 7.3 time-domain bromoform and chloroform measurements recorded under identical experimental conditions are shown. The key observation is that while the t_2 response is long-lived, that along t_1 never extends past the region of THz field overlap. Both bromoform's and chloroform's vibrational coherent responses

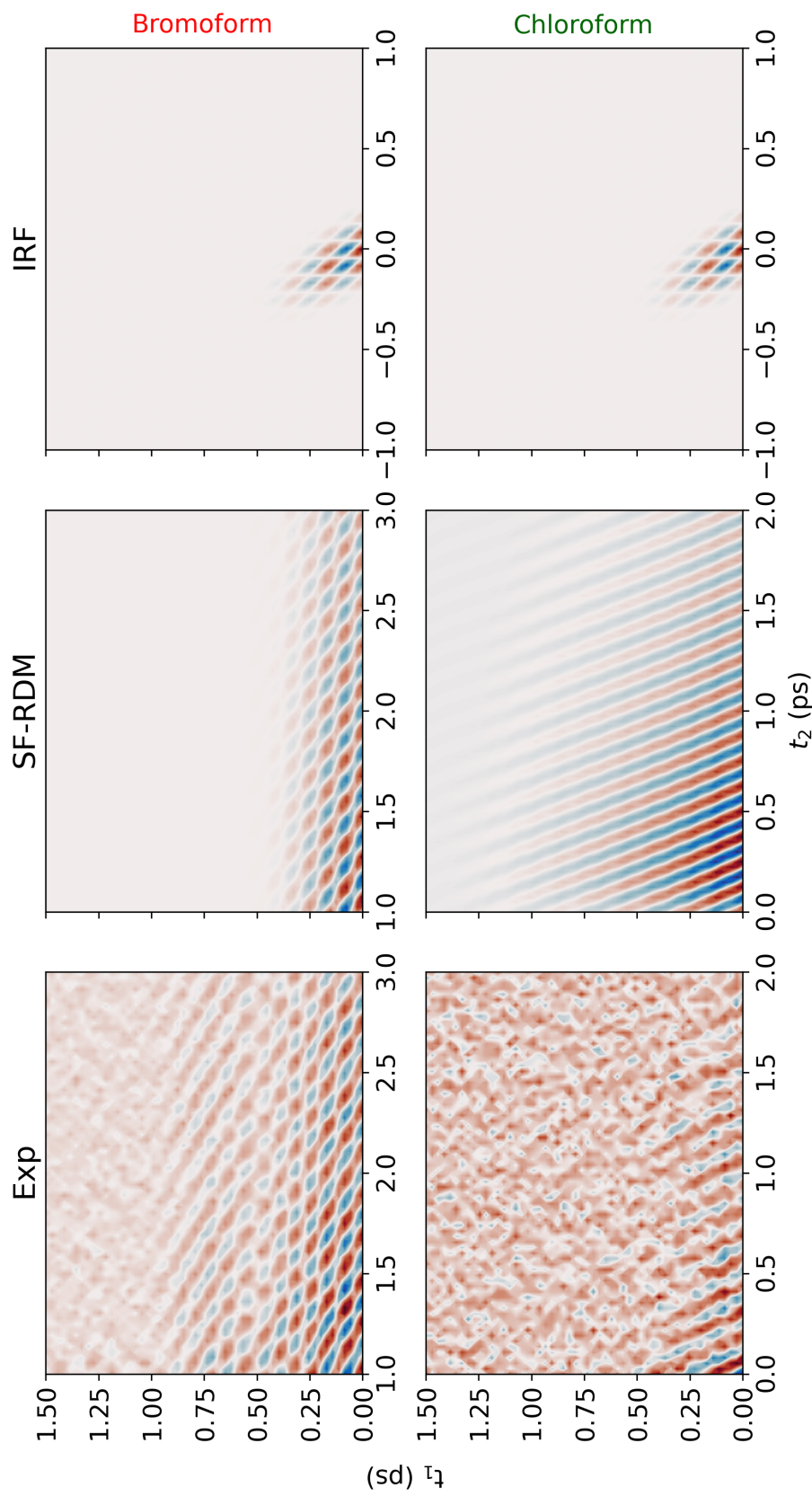


Figure 7.3: Top and bottom rows compare the experimental (Exp) bromoform and chloroform time-domain data to the SF-RDM models. The calculated IRF, whose THz electric fields are used as inputs to the SF-RDM model, is shown for reference (right column). Identical pulse shapes and IRFs are used for both SF-RDM models of bromoform and chloroform.

are therefore far more consistent with a SF excitation mechanism than a resonant process.

The different bandwidth requirements of the two processes provides a second argument supporting SF excitation as the dominant pathway. In both SF and resonant 2D-TTR pathways, a vibrational mode must begin and end the measurement in a population state. In addition, the Raman probe interaction only changes the vibrational quanta by ± 1 . If a M non-linearity is present, one of the THz field interactions must produce either a zero-quanta or two-quanta excitation, or bandwidths spanning $\geq 2\omega$ in the latter case [22]. (No evidence for zero-quanta transitions have been observed.) Again, this is quite different from 2D-IR spectroscopies. SF excitation, on the other hand, progresses with a bandwidth $\approx \omega/2$. The experimental THz field bandwidth spans 1-5 THz, and therefore the 2D-TTR experiment lacks the necessary frequency content to produce vibrational coherences arising from M non-linearities in the molecular Hamiltonian.

Given that sum-frequency excitation is the predominant source of the signals observed in 2D-TTR spectroscopy of HMs, a key mystery becomes how this mechanism, whose instantaneous nature precludes separating the two THz field interactions in time, can nonetheless produce a signal which varies along t_1 ? We interrogate the origins of this complex t_1 response by considering how the observed signal $S(t_1, t_2)$ depends upon the IRF $I(t_1, t_2)$ (Eq. 7.1). In a 2D-TTR experiment, two orthogonally polarized THz fields (\vec{X}, \vec{Y} in the lab frame) create a birefringent response within the room-temperature HM liquid sample. A \vec{X} polarized Raman probe scatters off this birefringence, producing a \vec{Y} polarized signal field that is selectively isolated through an analyzing polarizer and differential chopping. The 2D-TTR signal is proportional to the anisotropic third-order molecular response function $R_{XYXY}^{(3)}(t_1, t_2)$, and contains information on the molecular orientational and vibrational correlation functions of the system. During the measurement process, this response is inevitably convolved with the experimental IRF, which in 2D-TTR is determined by the product of the two THz electric fields.

$$S(t_1, t_2) = I(t_1, t_2) \circledast R_{xyxy}^{(3)}(t_1, t_2) \quad (7.1)$$

Through the convolution theorem, the time-domain convolution becomes a multiplication between the IRF spectral power and the HM molecular response function upon transformation to the frequency domain.

$$\tilde{S}(\omega_1, \omega_2) = \tilde{I}(\omega_1, \omega_2) \cdot \tilde{R}_{xyxy}^{(3)}(\omega_1, \omega_2) \quad (7.2)$$

7.3 Results: Instrument response function modelling

We study the impact of IRF convolution in two ways. First, we generate a time-domain model IRF (Fig. 7.3) using model THz field profiles (Fig. 7.6) that closely resemble experimental pulse shapes. The model THz pulse shapes were obtained with the following process. First, the bandwidths of the two THz pulses were optimized to fit both experimental HM TTR slices at eigenmode frequencies of bromoform and chloroform. To avoid overfitting, a simple asymmetric Gaussian functional form was assumed for the bandwidth of the THz pulses to minimize the number of parameters. The time domain IRF is calculated as the product of the THz pulse shapes

$$I(t_1, t_2) = E_1(t_1 + t_2)E_2(t_2)$$

and the Fourier transform of the IRF $\tilde{I}(f_1, f_2)$ is

$$\tilde{I}(f_1, f_2) = \tilde{E}_1(f_1)\tilde{E}_2(f_2 - f_1)$$

where \tilde{E}_1 and \tilde{E}_2 are the bandwidths of the THz pulses. The frequency domain optimization yields only the amplitude spectra, and a phase spectra is still required to uniquely determine the time-domain representation. The hybrid input-output phase retrieval algorithm was used with the experimentally measured THz pulse shapes as targets. Convergence was generally obtained within 100 iterations. The resulting model THz pulses accurately reproduce the observed time and frequency domain results for both HMs, as shown in the main text. THz pulse shape measurements in general underestimate the available power at higher THz frequencies due to velocity mismatch between the probe (800 nm) and THz pulses, which further supports the increased power above 4 THz for the model pulse shapes.

An instantaneous SF process gives a molecular response which is a delta function in the time-domain (t_1) and a flat response in the corresponding frequency domain (ω_1). In 2D-TTR, this amounts to a flat response along the ω_1 axis, and a delta functions along the ω_2 axis centered at the eigenmode frequencies of the molecular sample. Multiplication of this molecular response with the IRF yields the final measured signal. This results in simply selecting a slice of the IRF along ω_1 at the eigenmode frequency. Using this simple model we find excellent agreement with the experimental spectra.

7.4 Results: Sum-frequency reduced density matrix modeling

Second, we use the same THz field profiles that produce the IRF model as inputs to RDM simulations that consider sum-frequency excitation processes (SF-RDM). Sum-frequency pathways were not considered in our previous RDM model Hamiltonian [15, 16, 17]:

$$H(t; t_1) = H_0 - M \cdot [E_2(t - t_1) + E_1(t)] \quad (7.3)$$

A new Hamiltonian was constructed here, which accounts for the SF process:

$$H(t; t_1) = H_0 - \Pi \cdot [E_2(t - t_1) + E_1(t)]^2 \quad (7.4)$$

Experimentally, differential chopping of the two THz fields automatically removes the single pulse contributions $\Pi \cdot E_2^2(t - t_1)$ and $\Pi \cdot E_1^2(t)$, so we are left with an effective Hamiltonian of the form:

$$H(t; t_1) = H_0 - \Pi \cdot E_2(t - t_1)E_1(t) \quad (7.5)$$

The time response is computed as described in our previous work[17], but now it corresponds to an SF signal:

$$S(t_2; t_1) = S_{SF}(t_2; t_1) = Tr(\Pi \cdot \rho(t_2; t_1)) \quad (7.6)$$

The complete signal S is obtained when E_1 and E_2 are replaced with the fitted pulse shapes, while the molecular response R when E_1 and E_2 are simple δ -functions. All operators are kept linear and harmonic.

Again, we find near-quantitative agreement between the experimental data and theoretical simulations. Critically, no electrical or mechanical non-linearities are required to reach excellent agreement between the data and the IRF model/RDM simulations. The SF-RDM results precisely reproduce the experimental time-domain (Fig. 7.3) and frequency-domain (Fig. 7.4) responses, substantiating the claim that SF processes dominate the 2D-TTR response of HMs.

The agreement between experiment, SF-RDM, and model IRF are shown in Fig. 7.5. While bromoform and chloroform have different intra-molecular vibrational

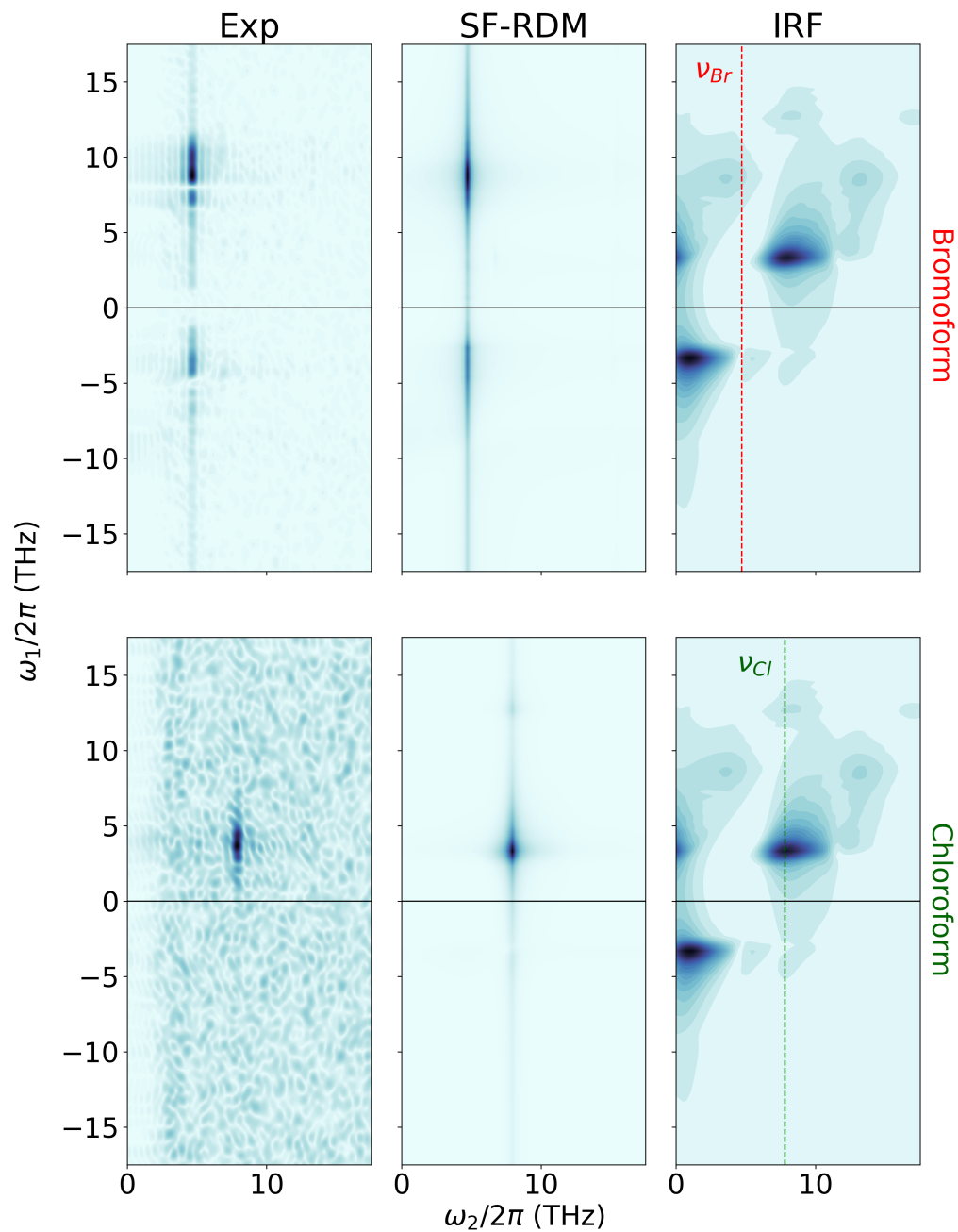


Figure 7.4: Top and bottom rows compare the experimental (Exp) bromoform and chloroform frequency-domain data to the SF-RDM model. The calculated IRF is shown for reference with vertical lines indicating where each HMs intramolecular vibrational mode samples the IRF. Note that the experimental and SF-RDM spectra are well matched, and arise from sampling the same IRF at different ω_2 frequencies.

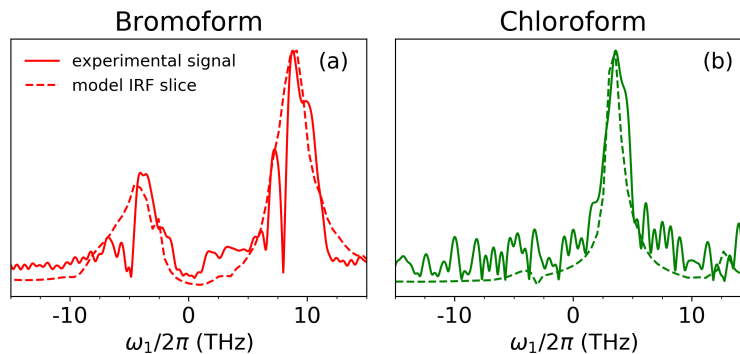


Figure 7.5: A) Slices along ω_1 at ω_2 =eigenmode of the IRF/RDM model and experimental response demonstrate the quality of fit for the bromoform data. B) Chloroform is reproduced by slicing along the same IRF/SF-RDM model as shown in A) at $\omega_2/2\pi=7.8$ THz, instead of at bromoform's $\omega_2/2\pi=4.7$ THz.

energies, we reproduce both spectra by slicing the same model IRF at their respective eigenmode frequencies along ω_2 . Crucially, this model mimics the non-specific sum-frequency excitation of vibrational coherences by the THz electric field. Unlike previous interpretations, here we do not invoke Feynman diagram pathways involving multi-quanta transitions between several vibrational modes; instead, the experimental IRF filtered through a single SF excitation pathway explains the data.

7.5 Conclusion

That a two-quanta sum-frequency excitation pathway is predominantly responsible for vibrational coherences observed in 2D-TTR is also supported by estimations of chloroform and bromoform's transition dipole moments. From THz-TDS measurements and FT-IR literature, the bromoform and chloroform *E* mode's molar extinction coefficients were $\epsilon \approx 1 \text{ M}^{-1} \text{ cm}^{-1}$, suggestive of a vanishingly small transition dipole moment [23]. As a result, it would be very difficult to observe resonant excitation of these HM modes, even in the absence of interfering SF pathways. For comparison, 2D-IR spectroscopy on proteins is often performed by resonantly pumping the amide I stretch at ~ 50 THz, which have $\epsilon \sim 200\text{-}400 \text{ M}^{-1} \text{ cm}^{-1}$. Not only are these oscillators intrinsically orders of magnitude stronger than HM vibrational modes, but the IR excitation field's $\delta\omega/\omega$ is also substantially narrower, which helps to selectively and resonantly generate the desired coherences while suppressing any SF contribution. Common sources of high intensity, sub-ps THz pulses (organic emitters, LiNbO₃, etc) all have $\delta\omega \approx \omega$ and thus both Res and SF pathways must be considered when analyzing responses in the overlapping pump

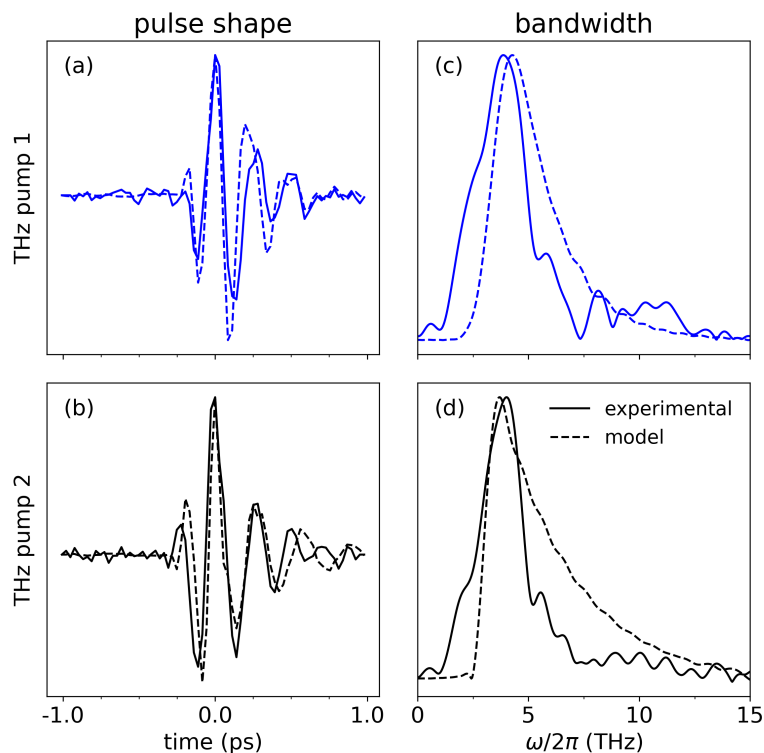


Figure 7.6: Comparison of the experimental and model THz pulse shapes (A,B) and corresponding bandwidths (C,D).

field region.

Finally, we would like to note that our conclusions regarding the excitation mechanism of intra-molecular vibrational modes of HMs in 2D-TTR spectroscopy likely do not alter analyses performed on similar systems in the complementary 2D-TRT and 2D-RTT experiments [13]. Those measurements attributed spectral features that remained post-deconvolution to couplings between a Raman-excited vibrational coherence and a resonant one-quanta interaction with bath modes of the liquid. Our conclusions are consistent with their observation that the IRF strongly determines the observed multi-dimensional experimental response.

In this work we provide extensive new experimental data and theoretical modeling that leads to a simple reinterpretation of previous 2D-TTR measurements of HMs. With this new analysis, we explain the complex 2D data sets for both bromoform and chloroform through a convolution of the experiment's THz fields with the molecules' intra-molecular vibrational modes. No coherence pathways outside of the SF-TKE process in Fig. 7.2 are required. The new analysis is also fully consistent with the

observed magnitudes of transition dipole moments and molecular polarizabilities.

Moving forward, there are two key lessons. First, large transition dipoles are crucial for performing truly resonant 2D-TTR experiments. Halogenated methanes unfortunately do not satisfy this requirement, and the bright, complex signals observed can easily be mis-attributed to resonant processes. Second, nearly transform-limited half-cycle THz fields would maximize the field strengths achievable, greatly simplify the experimental IRF structure, and reduce ambiguities in the analysis of dynamics in molecular systems.

BIBLIOGRAPHY

1. G. J. Mead, H.-W. Lin, I.-B. Magdau, T. F. Miller, G. A. Blake, Sum-Frequency Signals in 2D-Terahertz-Terahertz-Raman Spectroscopy. en, *J. Phys. Chem. B*, [acs.jpcc.0c07935](#), DOI [10.1021/acs.jpcc.0c07935](#) (Sept. 2020),
2. D. Mcmorrow, W. T. Lotshaw, G. A. Kenney-Wallace, Femtosecond Optical Kerr Studies on the Origin of the Nonlinear Responses in Simple Liquids. *IEEE Journal of Quantum Electronics* **24**, 443–454, DOI [10.1109/3.144](#) (1988).
3. M. Cho, M. Du, N. F. Scherer, G. R. Fleming, S. Mukamel, Off-resonant transient birefringence in liquids. *Journal of Chemical Physics* **99**, 2410, DOI [10.1063/1.465256](#) (1993).
4. A. Tokmakoff *et al.*, Two-Dimensional Raman Spectroscopy of Vibrational Interactions in Liquids. *Phys. Rev. Lett.* **79**, 2702–2705, DOI [10.1103/PhysRevLett.79.2702](#) (1997).
5. D. A. Blank, L. J. Kaufman, G. R. Fleming, Fifth-order two-dimensional Raman spectra of CS₂ are dominated by third-order cascades. *Journal of Chemical Physics* **111**, 3105–3114, DOI [10.1063/1.479591](#) (1999).
6. K. J. Kubarych, C. J. Milne, S. Lin, V. Astinov, R. J. D. Miller, Diffractive optics-based six-wave mixing: Heterodyne detection of the full $\chi^{(5)}$ tensor of liquid CS₂. *Journal of Chemical Physics* **116**, 2016–2042 (2002).
7. Y. Tanimura, S. Mukamel, Two-dimensional femtosecond vibrational spectroscopy of liquids. en, *The Journal of Chemical Physics* **99**, 9496–9511, DOI [10.1063/1.465484](#) (Dec. 1993).
8. T. Hattori, Classical theory of two-dimensional time-domain terahertz spectroscopy. *Journal of Chemical Physics* **133**, DOI [10.1063/1.3507256](#) (2010).
9. T. Ikeda, H. Ito, Y. Tanimura, Analysis of 2D THz-Raman spectroscopy using a non-Markovian Brownian oscillator model with nonlinear system-bath interactions Analysis of 2D THz-Raman spectroscopy using a non-Markovian Brownian oscillator model with nonlinear system-bath interactions. **212421**, 0–15, DOI [10.1063/1.4917033](#) (2015).
10. J. Savolainen, S. Ahmed, P. Hamm, Two-dimensional Raman-terahertz spectroscopy of water. *Proc. Natl. Acad. Sci. U. S. A.* **110**, 20402–20407 (2013).
11. A. Shalit, S. Ahmed, J. Savolainen, P. Hamm, Terahertz echoes reveal the inhomogeneity of aqueous salt solutions. *Nat. Chem.* **9**, 273 (2017).
12. P. Hamm, A. Shalit, Perspective: Echoes in 2D-Raman-THz spectroscopy. *J. Chem. Phys.* **146**, 130901 (2017).

13. G. Ciardi, A. Berger, P. Hamm, A. Shalit, Signatures of Intra- And Inter-molecular Vibrational Coupling in Halogenated Liquids Revealed by Two-Dimensional Raman-Terahertz Spectroscopy. *Journal of Physical Chemistry Letters* **10**, 4463–4468, DOI 10.1021/acs.jpcllett.9b01528 (2019).
14. M. A. Allodi, I. A. Finneran, G. A. Blake, Nonlinear terahertz coherent excitation of vibrational modes of liquids. *Journal of Chemical Physics* **143**, ISBN: 0831040831, 234204, DOI 10.1063/1.4938165 (2015).
15. I. A. Finneran, R. Welsch, M. A. Allodi, T. F. Miller III, G. A. Blake, Coherent two-dimensional terahertz-terahertz-Raman spectroscopy. *Proceedings of the National Academy of Sciences* **113**, 6857–6861 (2016).
16. I. A. Finneran, R. Welsch, M. A. Allodi, T. F. Miller, G. A. Blake, 2D THz-THz-Raman Photon-Echo Spectroscopy of Molecular Vibrations in Liquid Bromoform. *Journal of Physical Chemistry Letters* **8**, 4640–4644 (2017).
17. I. B. Magdău, G. J. Mead, G. A. Blake, T. F. Miller, Interpretation of the THz-THz-Raman Spectrum of Bromoform. *The Journal of Physical Chemistry A*, acs.jpca.9b05165, DOI 10.1021/acs.jpca.9b05165 (2019).
18. G. Mead, I. Katayama, J. Takeda, G. A. Blake, An echelon-based single shot optical and terahertz Kerr effect spectrometer. *Review of Scientific Instruments* **90**, 053107, DOI 10.1063/1.5088377 (2019).
19. S. Maehrlein, A. Paarmann, M. Wolf, T. Kampfrath, Terahertz Sum-Frequency Excitation of a Raman-Active Phonon. *Physical Review Letters* **119**, 1–6, DOI 10.1103/PhysRevLett.119.127402, arXiv: 1703.02869 (2017).
20. D. M. Juraschek, S. F. Maehrlein, Sum-frequency ionic Raman scattering. *Physical Review B* **97**, 1–8, DOI 10.1103/PhysRevB.97.174302, arXiv: 1801.05987 (2018).
21. V. Y. Shishkov, E. S. Andrianov, A. A. Pukhov, A. P. Vinogradov, A. A. Lisyansky, Enhancement of the Raman Effect by Infrared Pumping. *Physical Review Letters* **122**, 153905, DOI 10.1103/PhysRevLett.122.153905 (2019).
22. D. Sidler, P. Hamm, Feynman diagram description of 2D-Raman-THz spectroscopy applied to water. *Journal of Chemical Physics* **150**, DOI 10.1063/1.5079497 (2019).
23. d. NIST Mass Spectrometry Data Center William E. Wallace, en, in *NIST Chemistry WebBook, NIST Standard Reference Database 69*, type: dataset (National Institute of Standards and Technology, 1997), DOI 10.18434/T4D303.

Chapter 8

GAS-PHASE NONLINEAR TERAHERTZ PHENOMENA

In this chapter, we review two interesting nonlinear responses arising from the interaction THz photons with gases in the experimental enclosure. Intense field strengths at the focal region of the experiment are observed to generate third-order rotational coherences in the nitrogen purge gas. Second, water vapor along the THz beam transport path re-emits THz radiation with sufficient intensity to trigger secondary nonlinear Kerr effect signals in carbon disulfide are easily detectable for many tens of picoseconds along t_1 .

8.1 Terahertz excitation of coherent rotational wavepackets in N₂

Compared to the $\chi^{(3)}$ susceptibility of CS₂ ($\sim 10^{-21}$ m²/V²), air has an exceptionally small $\chi^{(3)}$ susceptibility of around 5×10^{-25} m²/V² [1, 2]. As a result, electric field strengths in excess of 10 MV/cm are required to generate a detectable non-linear birefringence in air [1]. While these field strengths are easily attainable at optical frequencies, [3, 4, 5], only recently have THz induced signals been reported [1]. We have successfully recorded the TKE response of the main molecular component in air, nitrogen gas, using the single-shot apparatus. This signal displays several remarkable characteristics which are interesting to analyze in some detail (Fig. 8.1).

As described in [3], this nonlinear response can be understood as a non-adiabatic molecular alignment of nitrogen molecules by the intense THz electric field. With sufficient electric field strength, an induced dipole is created in the electron shell of N₂. A torque exerted on this transient dipole by the THz field results in a coherent wave packet of rotational states, where each rotational state of N₂ ($B = 1.9896$ cm⁻¹) has the eigenenergy $E_J = hBcJ(J + 1)$.

In the time domain, wave-packet revivals alter the birefringence of the perturbed region; the magnitude of this birefringence is given by the alignment parameter $\langle \langle \cos^2 \theta \rangle \rangle$, which describes the time dependent weighted sum of all rotational states alignment relative to the THz field polarization. Defining τ in terms of T_{rev} , the alignment is given by:

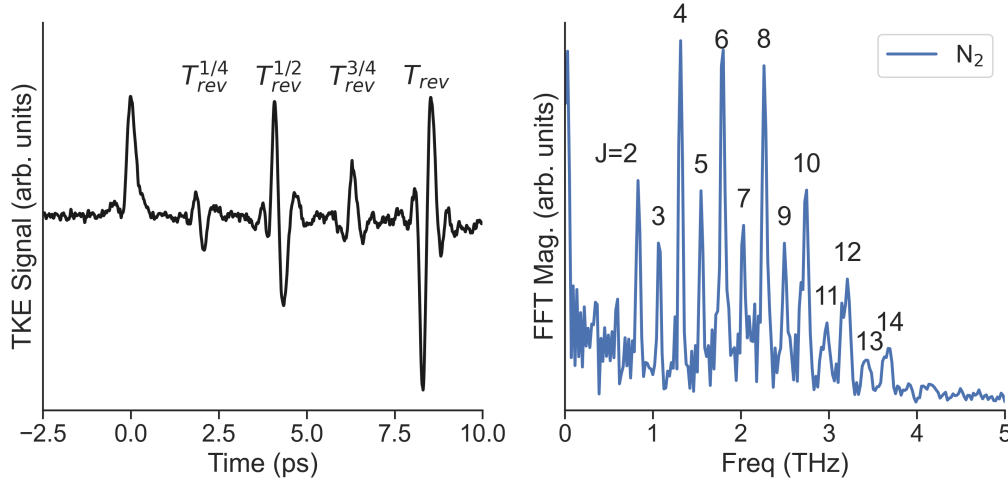


Figure 8.1: The time and frequency domain response of dinitrogen (N_2) at the focus of the nonlinear single shot THz experiment, with the cuvette removed from the sample position. Molecular revivals last for tens of picoseconds. In the frequency domain, nuclear spin statistics are observed in the alternating intensity of rotational transitions.

$$\langle \cos^2 \theta \rangle_{J_0 M_0}(\tau) = \sum_{J', M'} \sum_{J, M} \delta_{\{J, J' \atop J, J' \pm 2\}} \delta_{M, M'} \phi_{J, J'} \quad (8.1)$$

The initial response at 0 ps is a uni-polar non-resonant feature of comparable width to the main response in 1D-TKE measurements of SiN. Subsequent periodic revivals of the rotational wave packet are separated by 2.1 ps ($1/4 T_{rev}$, where $T_{rev} = 1/(2Bc)$) increments and persist for tens of picoseconds.

A key to understanding the alternating sign and magnitude of the nitrogen revivals is the time dependent phase term $\phi_{J, J'} = \exp(-i\pi\tau[J'(J' + 1) - J(J + 1)])$. For $\Delta J = 0$, this term is constant. However, $\Delta J = \pm 2$ transitions result in phase terms which oscillate over time proportional to $\exp(-i\pi\tau[4J + 6])$. At times $\tau = \eta T_{rev}$ where η is an integer value, all J states are in alignment and contribute a +1 phase term [4]. Anti-alignment at half-integer values of η result in a π phase difference between the $J_{even} = 0, 4, 8, \dots$ and $J_{odd} = 3, 7, 11, \dots$ states and the $J_{even} = 2, 6, 10, \dots$ and $J_{odd} = 5, 9, 13, \dots$. This phase shift results in the flipped sign of the revival signal at $T_{rev}^{1/2}$ compared to T_{rev} in Fig. 8.1.

For quarter intervals, the phase term from J_{even} states contributes either $\pm i$, while all J_{odd} states contribute either $\mp i$. These $\pi/2$ phase shifts are similarly observed

in the shape of the $T_{rev}^{X/4}$ revival signals. A reduction in signal intensity is due to the imperfect cancellation the J_{even} and J_{odd} contributions due to their 2:1 statistical weighting. In cases such as CO where $J_{even}:J_{odd}=1:1$, full cancellation of quarter revivals is seen, while in O_2 $J_{even}:J_{odd}=0:1$ and the quarter revivals have equivalent intensity to the half and integer revivals [3]. Fourier transformation of the N_2 response reveals the range of J states coherently excited by the THz field. Even and odd J states exhibit a clear 2:1 weighting from the total nuclear spin of ortho- and para-dinitrogen.

8.2 Water vapor emission as a secondary source of intense THz radiation

High THz field strengths suitable for nonlinear spectroscopy generally are only achieved in a well-purged experimental environment. Commonly, the Plexiglass enclosure in which THz light is generated and focused onto a sample is purged with the blow-off from a high-pressure Dewar of liquid nitrogen. Moisture content in this nitrogen gas source is on the order of a few ppm. While this atmosphere is adequate for nonlinear THz spectroscopy, unexpected consequences of the residual water content have been observed in 2D-TTR measurements of liquids.

To introduce the inadvertent role water vapor can play in 2D-TTR spectroscopy, it is first useful to reflect on a consequence of the 2D-TTR pulse sequence. A response along the t_1 axis around $t_2 = 0$ ps samples the electric field waveform of the scanned THz pump. The scanned THz field is referred to as the “idler” field in our current experimental setup, while the fixed THz field is called the “signal”. As so defined, a slice along t_1 of the 2D-TTR response of, e.g. CS_2 , at $t_2 = 0$ ps reveals a large oscillatory THz waveform in a small temporal region around $t_1 = 0$ ps. This effect has been usefully employed in diamond to perform a broad-band measurement of the THz field wave-forms in the nonlinear experiments [6].

Single-shot measurements, however, also detected lower intensity oscillations extending much further along t_1 than would be expected given the DAST THz emission waveform measured with EO sampling. Give that the central region around $t_1 = 0$ ps reflected the main THz electric field, by analogy these oscillations likely arise from a long-lasting (10s of ps) THz emission with sufficient electric field strength to induce a $\chi^{(3)}$ response in the liquid sample.

Higher-resolution data along t_1 assisted in identifying the THz emission source. A stage-scan 2D-TTR experiment was performed on CS_2 , wherein the probe delay stage was fixed at $t_2 = 0$ ps, and the THz-THz delay stage was scanned along t_1 .

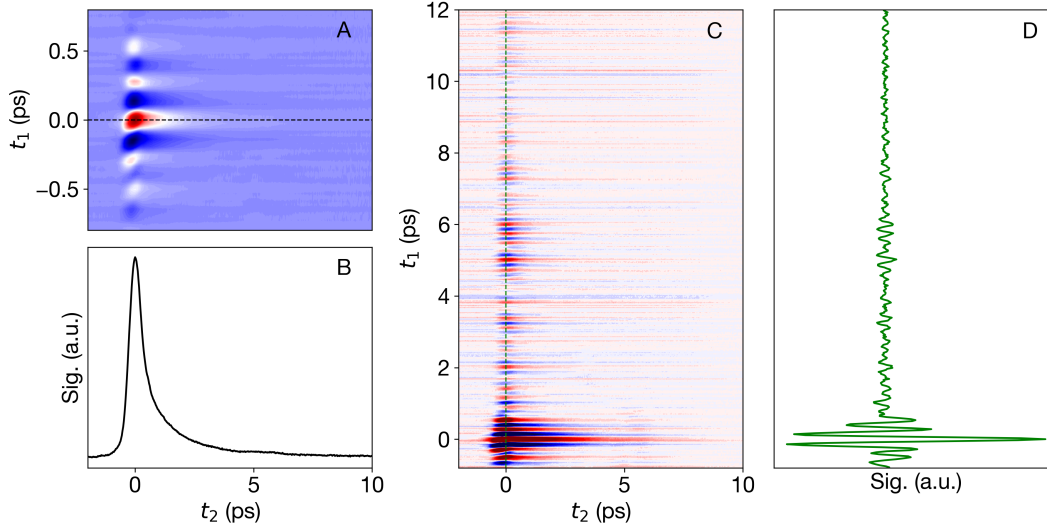


Figure 8.2: A) Inset of the main 2D-TTR response of CS₂. B) A long-lived decaying orientational molecular response is observed along t_2 at $t_1 = 0$. C) A view of the full 2D-TTR data set with intensity threshold set to $\pm 10\%$ maximum signal. Small random fluctuations in data baseline are seen along the t_2 axis. Larger oscillations are also observed around $t_2 = 0$. D) long-lived oscillations along t_1 at $t_2 = 0$ arise from coherent water vapor emission along the THz beam transport path.

Similar to the single-shot data, we observed a clear central response around $t_1 = 0$ ps (Fig. 8.3 A) with low intensity oscillations even at large t_1 delays (Fig. 8.4 A).

When Fourier transformed (Fig. 8.3 B), the central signal region displays a characteristic envelope of spectral power arising from the broadband DAST emission. Sharp, negative-going water absorption features are interspersed on the envelope, indicating where regions of power have been absorbed by the residual water vapor in the Plexiglass enclosure.

Surprisingly, the Fourier transform of regions at large t_1 (Fig. 8.4 B) instead show positive-going water *emission* features. These results clearly indicate that the water vapor has absorbed a substantial amount of the energy from the THz pulse. These water molecules are driven into a series of coherent, highly excited rotational states which emit THz photons over tens of picoseconds during the water's free-induction decay. Using water transitions line strengths and energies from the HITRAN database [7], the magnitude of water absorption was modelled, allowing the source of water vapor emission to be identified. Excellent agreement between the data and model was found assuming an absorbing volume with a uniform cross-sectional area of 5 cm and a path length of 100 cm at a water molecule number

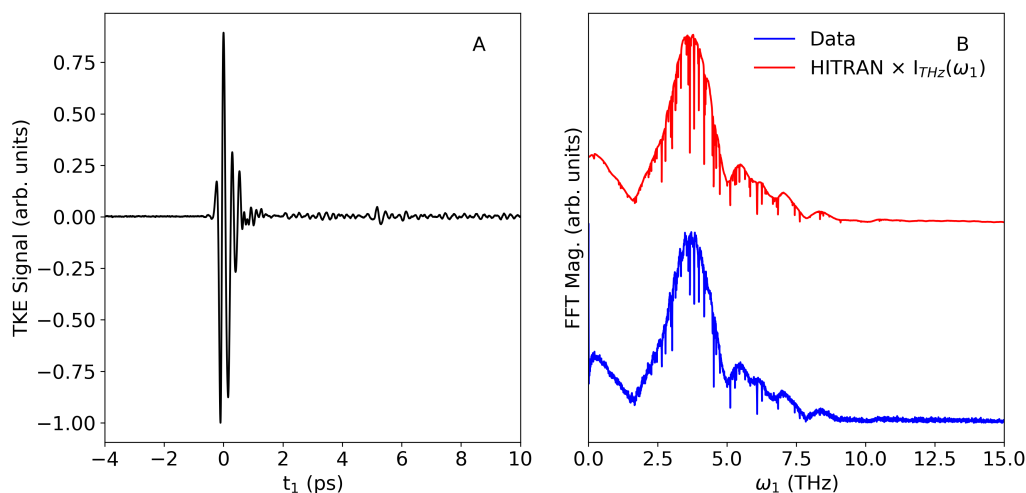


Figure 8.3: A) The t_1 response of CS_2 at $t_2 = 0$ in a 2D-TTR experiment. B) Fourier-transform of A), demonstrating the bandwidth of the experiment and sharp absorption features from water vapor in the THz beam path. A HITRAN water model weighted by the THz power envelope reproduces the spectra, confirming the identification of water as the THz source inducing a nonlinear response in CS_2 .

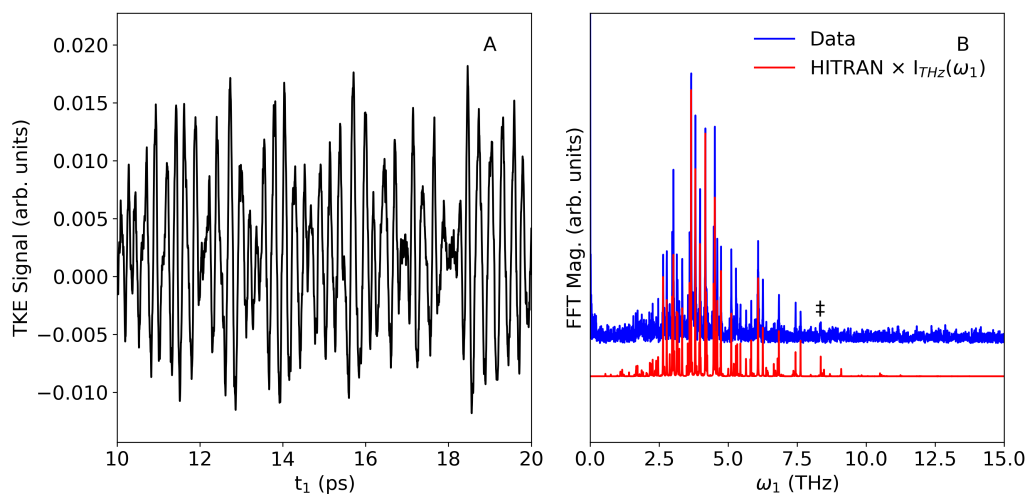


Figure 8.4: A) A zoomed-in section of the small oscillations present for a hundred picoseconds along t_1 . B) The FFT of A) reveals positive-going water vapor emission features. A HITRAN water model weighted by the THz power envelope reproduces the spectra, confirming the identification of water as the THz source inducing a nonlinear response in CS_2 .

density of 80 ppm. These parameters indicate that water molecules along the full THz beam transport pathway absorb a substantial portion of energy from the THz pump field which is then coherently emitted and re-absorbed at the liquid sample. The slightly elevated calculated water concentration relative to typical liquid nitrogen blow-off concentrations cited by manufacturers (2 ppm cf. 80 ppm) is reasonable given the many small openings in the purge box and off-gassing from the many anodized aluminum components within the box.

In analogy to the importance of characterizing the IRF when interpreting intra-molecular vibrational spectra, a primary consequence of this water emission finding is that similar care must be taken to properly characterize the bulk orientational response of the sample. Halogenated methanes represented a unique case where the orientational response of the system — which is widely studied in the theoretical literature on hybrid THz-Raman spectroscopies [8, 9, 10, 11, 12] — is not required for analysis. Detrending this orientational response helps isolate the intra-molecular vibrational modes. In contrast, many molecules do not have the intra-molecular modes in HMs and the only observable for analysis by 2D-TTR is the orientational response of the system. However, generating sub-cycle THz waveforms from the organic emitter crystal will not fully simplify the IRF of the system. Contributions from water vapor emission must be considered in order to isolate the molecular response arising from the t_1 dependent interaction of the main THz pulses, vs secondary emission from the water vapor, which extends along t_1 and may obscure signals arising from the main THz interactions.

Finally, it is worth commenting on the high THz bandwidths detectable along t_1/ω_1 . A clear transition at 8.36 THz (\ddagger) is visible in Fig. 8.4 B. With shorter THz pulses, a less featured and broader spectral bandwidth along ω_1 should be readily achievable. Raman probe bandwidth limitations will not affect this axis, and the Nyquist frequency can be freely tuned by varying the t_1 step size (subject to mechanical precision).

BIBLIOGRAPHY

1. M. Shalaby, C. P. Hauri, Air nonlinear dynamics initiated by ultra-intense lambda-cubic terahertz pulses. en, *Appl. Phys. Lett.* **106**, 181108, DOI 10.1063/1.4919876 (May 2015).
2. K. Iliopoulos *et al.*, Ultrafast third order nonlinearities of organic solvents. *Optics Express* **23**, ISBN: 1094-4087, 24171, DOI 10.1364/oe.23.024171 (2015).
3. G. Kaya *et al.*, Nonadiabatic molecular alignment of linear molecules probed by strong-field ionization yields of photoelectrons. en, *Appl. Phys. B* **122**, 288, DOI 10.1007/s00340-016-6562-1 (Dec. 2016).
4. P. W. Dooley *et al.*, Direct imaging of rotational wave-packet dynamics of diatomic molecules. en, *Phys. Rev. A* **68**, 023406, DOI 10.1103/PhysRevA.68.023406 (Aug. 2003).
5. E. M. L. English *et al.*, “Revival of a rotational wavepacket initiated by ultrafast impulsive alignment”, en, tech. rep. (Central Laser Facility, United Kingdom Research and Innovation, 2005), p. 3.
6. I. A. Finneran, R. Welsch, M. A. Allodi, T. F. Miller, G. A. Blake, 2D THz-THz-Raman Photon-Echo Spectroscopy of Molecular Vibrations in Liquid Bromoform. *Journal of Physical Chemistry Letters* **8**, 4640–4644 (2017).
7. I. Gordon *et al.*, The HITRAN2016 molecular spectroscopic database. en, *J. Quant. Spectrosc. Radiat. Transf.* **203**, 3–69, DOI 10.1016/j.jqsrt.2017.06.038 (Dec. 2017).
8. Y. Tanimura, S. Mukamel, Two-dimensional femtosecond vibrational spectroscopy of liquids. en, *The Journal of Chemical Physics* **99**, 9496–9511, DOI 10.1063/1.465484 (Dec. 1993).
9. P. Hamm, A. Shalit, Perspective: Echoes in 2D-Raman-THz spectroscopy. *J. Chem. Phys.* **146**, 130901 (2017).
10. T. Ikeda, H. Ito, Y. Tanimura, Analysis of 2D THz-Raman spectroscopy using a non-Markovian Brownian oscillator model with nonlinear system-bath interactions Analysis of 2D THz-Raman spectroscopy using a non-Markovian Brownian oscillator model with nonlinear system-bath interactions. **212421**, 0–15, DOI 10.1063/1.4917033 (2015).
11. H. Ito, T. Hasegawa, Y. Tanimura, Calculating two-dimensional THz-Raman-THz and Raman-THz-THz signals for various molecular liquids: The samplers. en, *The Journal of Chemical Physics* **141**, 124503, DOI 10.1063/1.4895908 (Sept. 2014).

12. P. Hamm, J. Savolainen, Two-dimensional-Raman-terahertz spectroscopy of water: Theory. en, *The Journal of Chemical Physics* **136**, 094516, DOI 10.1063/1.3691601 (Mar. 2012).

Chapter 9

2D-TTR SPECTROSCOPY OF MATERIALS

Solid-state materials represent a sharp departure from other samples studied by nonlinear THz spectroscopy in previous chapters. While there is great promise in creatively applying multi-dimensional methods to examine electron-phonon and phonon-phonon couplings in solid-state materials [1, 2, 3], applications of 2D-TTR to these questions are in early stages [4]. In this chapter, we review results from a series of materials that illustrate various responses that may be observed in 2D-TTR experiments. Some, such as diamond, have quite weak 1D and 2D THz Kerr effect signals due to an inherently small $\chi^{(3)}$ response. Others, such as gallium phosphide (GaP), are $\chi^{(2)}$ active crystals commonly used for electro-optic sampling in linear THz time-domain spectroscopy, but a small $\chi^{(3)}$ response allows a response to be observed in 2D-TTR measurements. Finally, 1D-TKE and 2D-TTR measurements of lithium niobate, a ferroelectric material, displays strong oscillatory signals arising from an IR and Raman active phonon mode at 3.9 THz. These signals may be explicable as a cascaded $\chi^{(2)} \cdot \chi^{(2)}$ process, or as a $\chi^{(3)}$ process involving anharmonicities in the polarizability operator.

9.1 Diamond

Diamond is a colorless, non-birefringent material with a cubic crystal structure. Since its lowest phonon mode is at 40 THz [5], diamond provides a non-resonant Kerr response to the THz electric fields in our experiments (bandwidth ≤ 10 THz). Much of the useful analysis of diamond 2D-TTR measurements were developed by a former graduate student, Ian Finneran [6].

In the most recent data acquired with the single-shot spectrometer (Fig. 9.1 A), the response of diamond has been measured across a broader t_2 range. A remarkable property of 2D-TTR spectroscopy is that the complex experimental THz electric fields can be extracted by measuring a sample whose $\chi^{(3)}$ response is dominated by a non-resonant electronic component. Diamond and gallium phosphide (discussed in the next section) are two examples of materials suitable for such measurements. The two THz electric fields can be retrieved from the diamond data by slicing the data along the axes $(t_1, t_2 = 0)$ and $(t_1, t_2 = -t_1)$. Fig. 9.1 B shows the THz electric field measured along the $(t_1, t_2 = 0)$ direction, while the Fourier transform of the

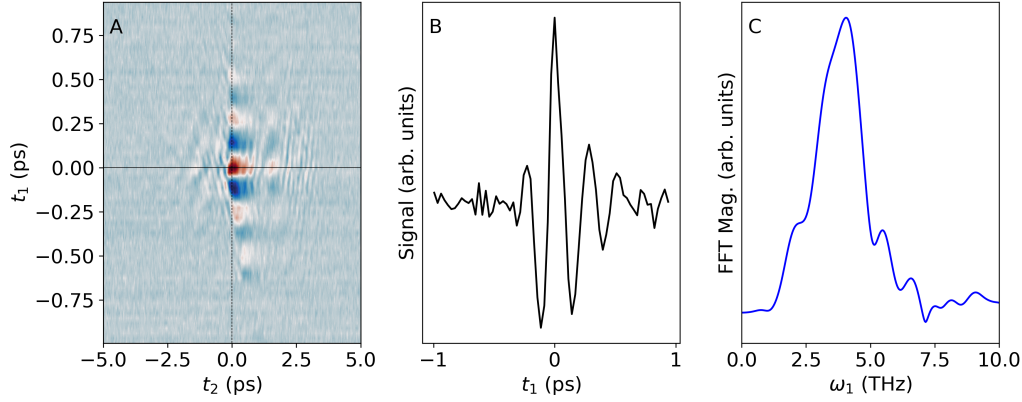


Figure 9.1: A) 2D-TTR response of diamond. B) The THz electric field traced by the vertical black line in A). C) The Fourier transform of the THz electric field.

electric field is shown in Fig 9.1 C. We observe a broad pulse bandwidth common to organic crystalline emitters, with a central frequency at 4 THz.

There are significant analogies between THz Kerr effect measurements and more well-known field-retrieval techniques such as polarization-gated frequency resolved optical gating (PG-FROG) measurements [7]. The family of FROG techniques were developed to measure the intensity, frequency, and phase of ultra-fast optical laser pulses. The key insight was to use two copies of the same pulse to perform interferometric measurements, which then allowed retrieval algorithms to reconstruct the pulse profile [8]. In PG-FROG, a beam-splitter produces two copies of the same pulse, ω . One copy is focused in a thin material with a fast $\chi^{(3)}$ susceptibility (e.g. fused silica or diamond), inducing a birefringent response. This birefringence is sampled using polarimetry by the second ω pulse, whose spectrum is then recorded after passage through the sample. A series of measurements as a function of the time delay between the two pulses produces a $\{t, \omega\}$ spectrogram that can be analyzed to unambiguously reconstruct the ω field.

Both 1D-TKE and 2D-TTR measure THz fields in a manner similar to PG-FROG measurements of optical fields. Diamond's 1D-TKE response traces the intensity profile of the THz field along t_2 , providing precisely the same information as PG-FROG but without the need for spectrograms or retrieval algorithms. 2D-TTR, however, provides the full THz electric field by introducing a second adjustable time delay, t_1 . Differences between 1D-TKE and 2D-TTR, and PG-FROG, result from the different carrier frequencies of the characterized pulse. The spectrometer in

PG-FROG may be forgone since the much longer THz wavelengths can be directly recorded in the time-domain using a photo-diode or camera. The hybrid THz-optical measurement approach is suitable for recording the THz field since the optical pulse is shorter than the THz field. (Note this simplification cannot be used in PG-FROG, where the optical pulse being characterized is on the order of 10-50 fs FWHM.)

In the future, improved 2D-TTR measurements of diamond may be possible by acquiring a thinner sample with more pristine surfaces. The single crystal diamond used for these measurements was received from a de Beers Group subsidiary, element6. Unfortunately, other nominally single crystal diamond samples received from other companies were found to be poly-crystalline, which created an unacceptable level of probe light scatter in the single-shot spectrometer.

One remaining question in the 2D-TTR diamond data are the low-level oscillations before and after the main diamond response (Fig. 9.1 A). These may be the result of diffraction effects from the nonlinear aperture in the sample, scattering from the rough diamond surface, or another as-yet unidentified effect from passage through the thick (300 μm) sample. Since stage-scan measurements of the same diamond sample in 2017 did not detect these oscillations, scatter from accumulated debris on the diamond surface cannot be discounted as a source of these oscillations. An alternate possibility is that the diamond is accurately responding to the incident THz fields. Dispersion during optical rectification in DAST may lead to frequency-dependent stretching of the pulse that produces these low intensity precursor fields. Diamond's exceptionally flat index across the THz region may enhance the experimental sensitivity to these features.

9.2 Gallium phosphide

Gallium phosphide (GaP) has a zincblende crystal structure [9] with uni-axial symmetry along the optical c axis. With a linear electro-optic tensor coefficient of $r_{41} = 0.97 \text{ pm/V}$ (cf. $\text{ZnTe } r_{41} = 3.9 \text{ pm/V}$), GaP is an efficient emitter and detector of THz radiation and finds common use in linear THz time-domain spectroscopy measurements.

GaP also retains a small $\chi^{(3)}$ response [10] which allows it to be studied with 2D-TTR spectroscopy. Similar to diamond, the Kerr effect response of GaP follows the THz electric field intensity along t_2 , and so provides much of the same information as diamond. Also similar to diamond, the 2D-TTR GaP response along the $(t_1, t_2=0)$ and $(t_1, t_2 = -t_1)$ axes reflect the two THz electric fields of the experiment.

One benefit to GaP is the much stronger signal it produces compared to diamond. Apart from a small cost to higher-frequency sensitivity, GaP provides a fast and convenient method for characterizing 2D-TTR experiments.

In analogy to the contributions of water vapor emission to the 2D-TTR response of CS₂ discussed in Chapter 8, we see another example of a secondary THz field producing a Kerr effect response in the GaP data (Fig. 9.2 A and B). In GaP, a second THz field arises from an etalon reflection off the exit face of the crystal. The secondary THz field source is confirmed by the arrival time of the second THz pulse at time $t_1 \approx 2.3\text{ps}$, which matches the round-trip time for a THz pulse to reflect off the exit face of the 100 μm thick GaP crystal and return to the entrance face. In addition, we can observe how the second THz signal is an inverted copy of the main feature, indicating a reflection has occurred. Finally, the Fresnel equation for reflected power at normal incidence may be used to estimate the amount of THz power reflected backwards from the crystal exit face. Using the Fresnel equation:

$$R = \left| \frac{n_1 - n_2}{n_1 + n_2} \right|^2 \quad (9.1)$$

and the indices of refraction of air ($n_1=1$) and GaP ($n_2 \approx 3.3$), a predicted 28% of the THz power is reflected backwards. Because the slice along t_1 traces the electric field, and not the power (E_{THz}^2), the secondary peak should be around 53% of the main peak's magnitude. The slightly smaller observed magnitude of the second peak may be attributable to a slightly off-normal incidence, scattering losses, and other imperfections in the experimental measurement. A thicker, optically contacted crystal would also reduce the intensity of secondary peaks.

9.3 Lithium niobate

In this section, we analyze single-shot 2D-TTR data of lithium niobate. Lithium niobate (LiNbO₃) is a crystalline ferroelectric material that is anisotropic and highly birefringent. Raman scattering and infrared absorption spectroscopies have identified three *E*-symmetry transverse optical (TO) phonons within the 0-7.5 THz bandwidth accessible to the single-shot spectrometer. One of these modes, at a nominal frequency $\omega_i=4.55\text{ THz}$, is intensely Raman and IR ($\mu_{21} \approx 3\text{ Debye}$) active, with an order of magnitude larger oscillator strengths than the other two modes within the experimental bandwidth [11, 12].

Like GaP, LiNbO₃ has a non-zero $\chi^{(3)}$ nonlinear susceptibility which allows inves-

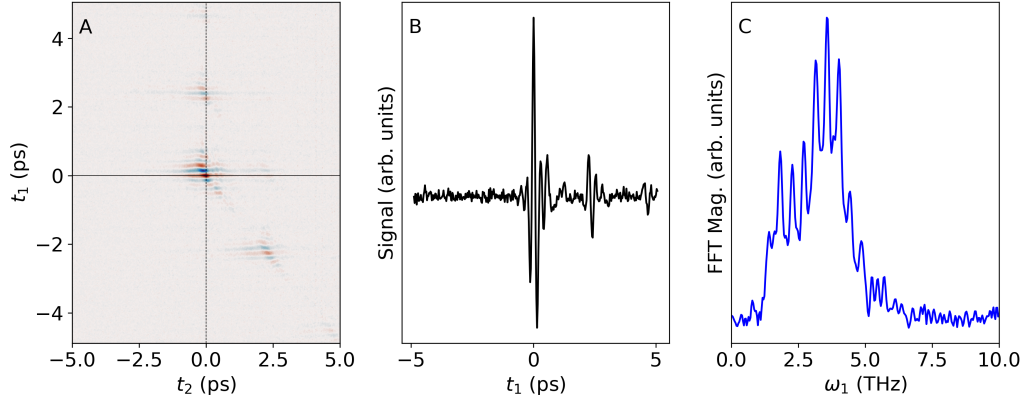


Figure 9.2: A) 2D-TTR response of gallium phosphide. The vertical black line traces the electric field shown in B). The Fourier transform of the field is seen in C). Modulation of the spectral power arises from the two reflections in B) at $t_1 \approx 2.5$ and 5.0 ps.

tigation by third-order spectroscopies. Several studies investigate the third-order nonlinear optical properties of LiNbO_3 and isomorphic ferroelectric oxides, but there have been no published works to date that examine the 2D nonlinear response of LiNbO_3 [12, 13, 14, 15, 16].

Experimental approach and results

We performed 2D-TTR experiments on an X cut lithium niobate sample ($0.05 \times 4 \times 4 \text{ mm}^3$, NuAssembly). The crystal's strong optical activity presents some constraints on the crystallographic axes accessible to the experiment. Only probe polarizations parallel or perpendicular to the $\{Y, Z\}$ crystallographic axes could be measured without rotating an unacceptably large number of probe photons. Two orthogonally polarized THz fields were generated in organic crystalline emitters and combined using a wire grid polarizer. Separate 2D TTR measurements were performed with the THz fields polarized parallel and at 45 degrees to the $\{Y, Z\}$ crystallographic axes. No differences in 2D-TTR response were observed in these two configurations.

Initial reference 1D-TKE measurements of lithium niobate verified the presence of a Ω_+ phonon mode at 3.9 THz. These data are characterized by a very strong oscillatory signal along t_2 (Fig. 9.3 A) which gradually grows in intensity over 2 picoseconds, indicating a non-impulsive excitation mechanism [17]. These results are consistent with other terahertz Kerr effect measurements which suggest the Ω_+

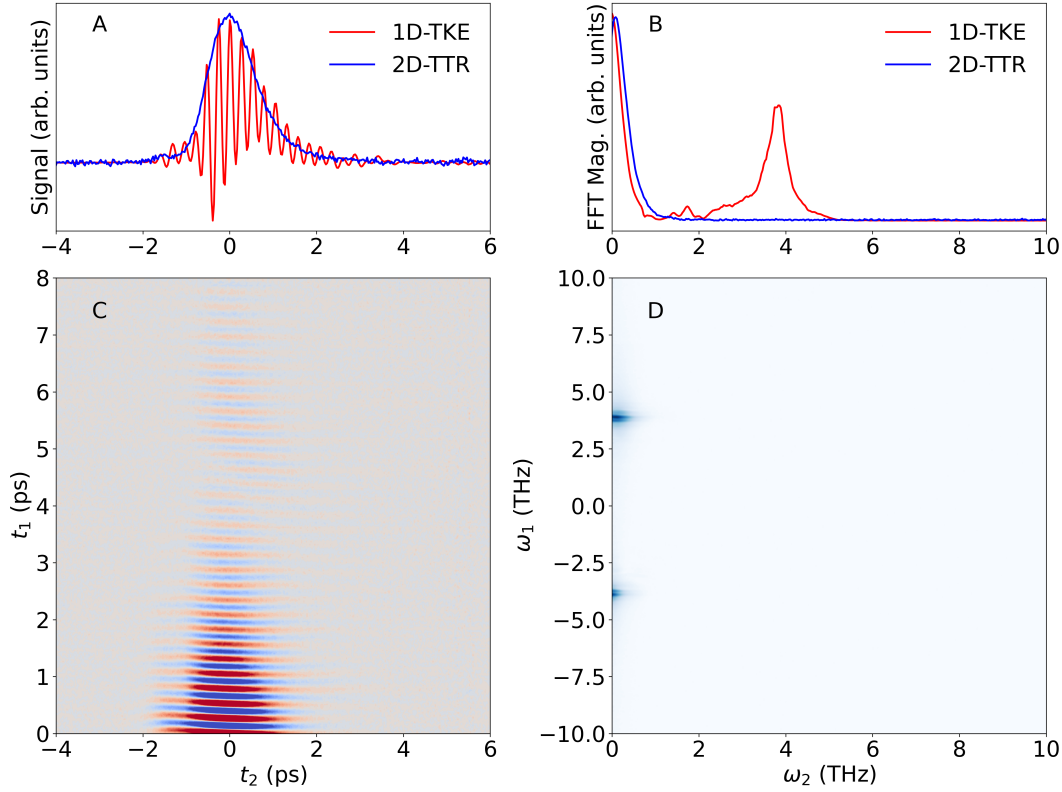


Figure 9.3: Comparison of 1D-TKE and 2D-TTR t_2 signals in lithium niobate. Time (A) and frequency domain (B) 1D-TKE data display a strong phonon mode along t_2 that is lacking in the 2D-TTR data (C, D). Instead, the phonon signal is clearly observed along t_1/ω_1 in the 2D-TTR data.

mode is excited through a sum-frequency pathway [18, 17]. In contrast, impulsive stimulated Raman scattering studies of lithium niobate have observed excited E -symmetry TO phonons which travel through the material with corresponding wave-vectors $\Omega_- = 2.9$ THz and $\Omega_+ = 3.9$ THz [19]. THz pump selectivity of the Ω_+ mode can be explained through considering wave-vector matching of the optical and THz pump fields in the sample (cf. Reference [19] and Fig. 9.4).

In contrast to the 1D-TKE results, the same sample measured with 2D-TTR reveals no oscillatory component along t_2 , although the uni-polar signal shares an intensity envelope with the 1D-TKE response (Fig. 9.3 A). Instead, a clear contribution from the phonon mode is oriented along the t_1 axis (Fig. 9.3 C). Fourier transformation of the 2D-TTR t_1 response confirms the presence of the 3.9 THz phonon mode along the ω_1 axis (Fig. 9.3 D). In the next two sections, we will present two interpretations of these data. The first applies the theories and analysis of third-order $\chi^{(3)}$ THz spectroscopy. A second approach accounts for the strong optical activity of the

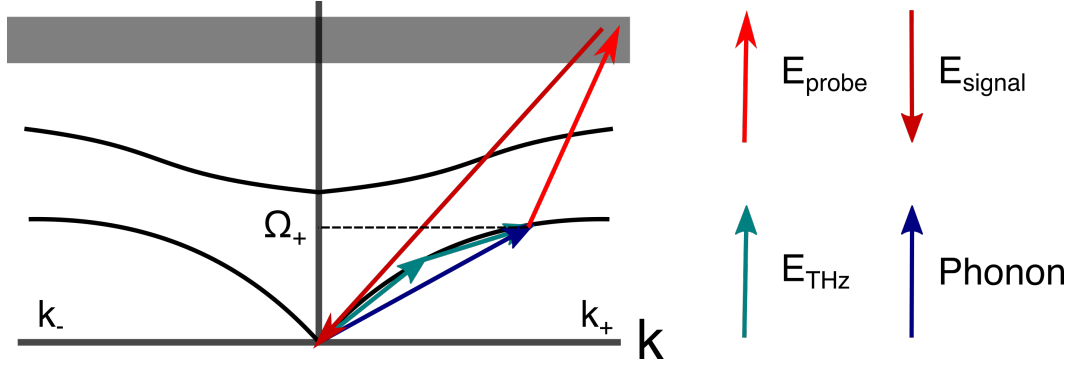


Figure 9.4: Model of sum-frequency THz excitation of E -symmetry TO phonon mode in LiNbO_3 . Two THz photons combine to directly excite the Ω_+ wave-vector phonon. The Ω_- phonon oriented along the k_- direction is inaccessible without an impulsive Raman pump. Probe and signal fields are at 800 nm.

sample, proposing a cascaded $\chi^{(2)} \cdot \chi^{(2)}$ process as a viable alternative explanation.

Interpretation #1: A $\chi^{(3)}$ response

To interpret these 2D-TTR data in a $\chi^{(3)}$ framework, we must consider the various phonon excitation pathways, and the instrument response function of the 1D and 2D experiments. First, we can compare the 2D spectra to the instrument response function used to analyze halogenated methane data (Fig. 9.5 A vs. B). While the lithium niobate data displays features that fall within regions of IRF power, slices through the lithium niobate data confirm that these features are much narrower than the IRF power envelope (Fig. 9.5 D and F). This is in contrast the previous investigations of halogenated methane 2D-TTR spectra, whose intramolecular vibrational eigenmode frequency on ω_2 precisely traced out the envelope of the IRF power along ω_1 . There is no evidence for this effect in the lithium niobate data (Fig. 9.5 E).

Other aspects of the data are more puzzling. Foremost is the absence of a convolution between the intramolecular mode excited via a sum-frequency process and the IRF [20]. This is especially odd since the Ω_+ feature observed in 1D-TKE is generated through an identical sum-frequency process. In HM 2D-TTR, this linear process appeared as a convolution in the 2D time-domain data despite 2D-TTR's presumed selectivity for nonlinear coherence pathways. Given the similar excitation pathway, why does a convolution response not appear at $\omega_2 = \Omega_+$ in the lithium niobate data? One possibility is that the halogenated methane IRF shown in Fig. 9.5B does not fully model the IRF in the lithium niobate experiment. In this case, then the magnitude of the sum-frequency response at $\omega_2 = \Omega_+$ may be inaccurately

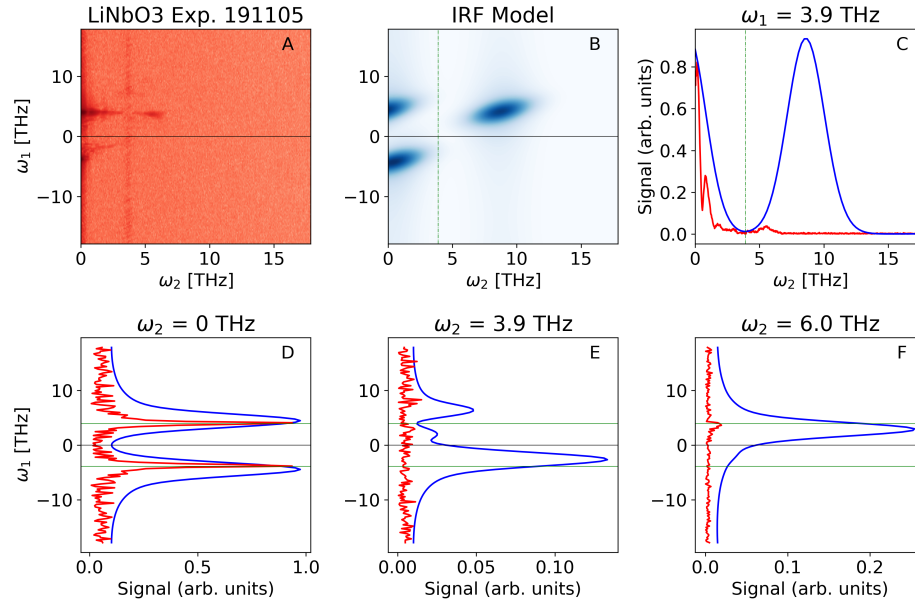


Figure 9.5: A) Lithium niobate 2D-TTR spectrum. B) Model IRF from [20]. C) Comparison of experimental data and IRF model at $\omega_1=3.9$ THz. A small feature is observed at $\omega_2=6.0$ THz. D) A sharp feature at $\omega_1=3.9$ THz at $\omega_2=0$ THz resides in a region of strong IRF power but does not follow the IRF power. E) No experimental features are observed at $\omega_2=3.9$ THz along ω_1 . F) A small feature at $\omega_1=3.9$ THz is observed at $\omega_2=6.0$ THz. Similar to D), the feature is narrow and does not reflect the IRF spectral power distribution.

estimated. While two broadband THz fields were used to construct the IRF in Fig. 9.5B, these fields need not be the only contributions to the 2D-TTR experiment in LiNbO₃.

We develop this argument by re-examining the oscillatory response along t_1 . While in 1D-TKE an oscillatory response along t_2 was only consistent with a sum-frequency interaction between the THz fields and the phonon mode, the 2D-TTR response along t_1 is consistent with a linear one-quanta THz absorption process. Upon excitation, the excited phonon mode will emit an oscillating electric field for a time t_1 before the second THz field reaches the sample. Thus, the IRF is described not just by the product of the two THz fields, but also by the very pronounced phonon electric field. (This secondary phonon field is somewhat similar to the water vapor emission seen along t_1 in 2D-TTR measurements of CS₂. In that case, THz emission from water vapor's free induction decay produced an additional field for the second THz pump to interact with. These two fields — one from the organic crystalline emitter and the other from the water vapor — produced a familiar Kerr effect orientational

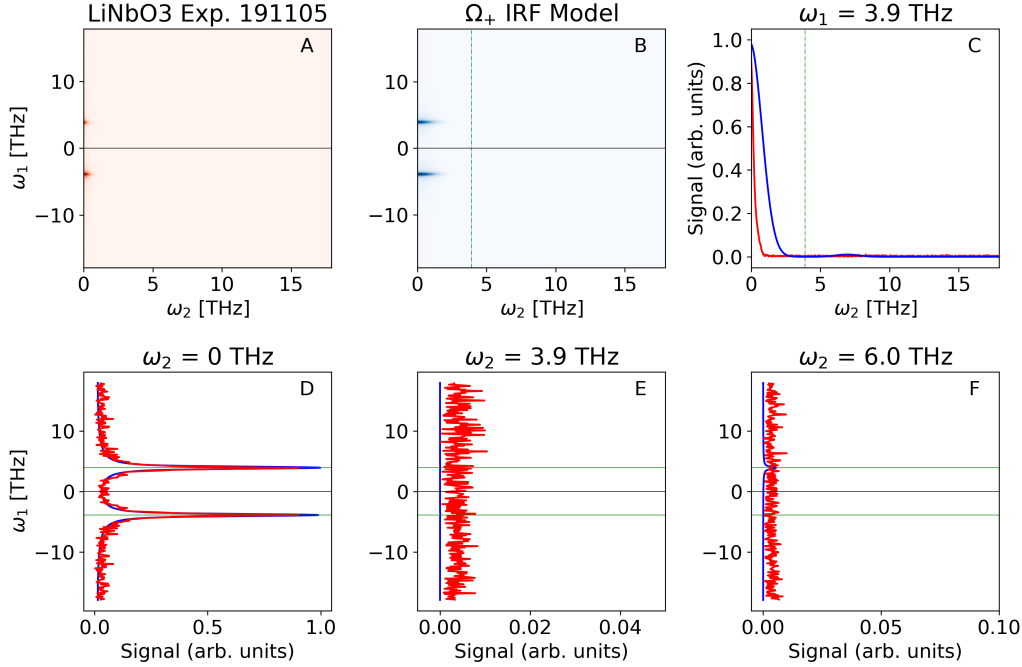


Figure 9.6: Comparison of the 2D-TTR lithium niobate data to the modelled Ω_+ -THz IRF.

decay in CS_2 for several picoseconds along t_1 .)

To test whether a phonon field contribution to the IRF is consistent with the data, an IRF model was created using a long-lived oscillatory phonon field and a shorter THz pump field. This simple two field model was combined with a Gaussian window along ω_2 to simulate the frequency-dependent sensitivity of the Raman probe pulse (Fig. 9.6). Comparison between the experimental spectra and the new IRF reveal excellent agreement. Two sharp features appear at $\omega_2 = 0$ THz at the phonon mode frequency. The lack of any convolution signal at $\omega_2 = \Omega_+$ results from the new IRF's obvious power minima at this frequency.

Feynman diagram analyses

Next, the possible coherences pathways producing features attributed to a $\chi^{(3)}$ process in LiNbO_3 must be analyzed using Feynman diagrams for a generic oscillator [21]. A 2D-TTR response requires one of the field interactions to proceed through a nonlinear pathway; the non-linearity may reside in the dipole (M) or the polarizability (Π) operator. Fig. 9.7 illustrates the predicted spectra produced from each kind of non-linearity.

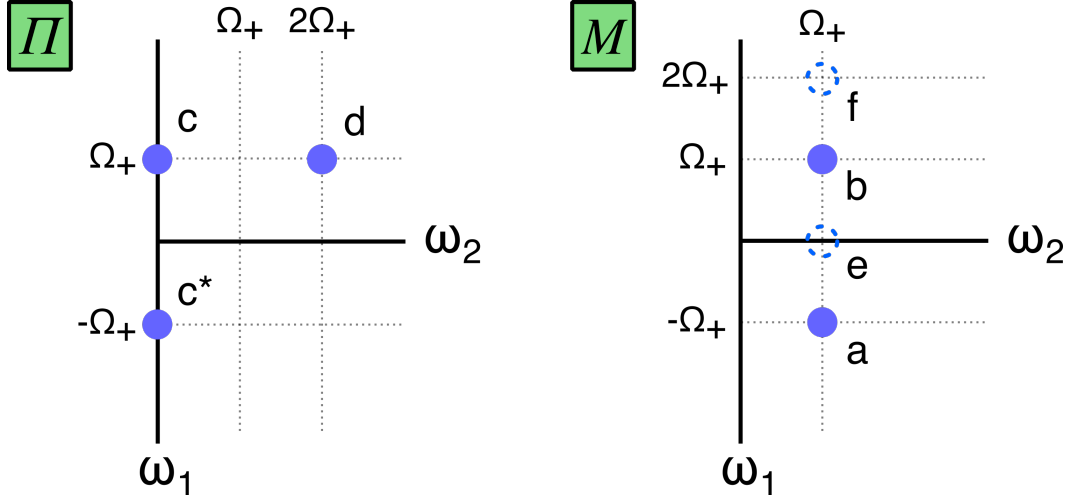


Figure 9.7: Lithium niobate 2D-TTR spectral features are consistent with predictions for an oscillator with anharmonicity in the polarizability operator Π . Spectral power distribution in the Ω_+ -THz 2D IRF precludes observing any features apart from c and c^* . Labels and results derived from [21].

The LiNbO_3 data are most consistent with the theoretical Π spectra, which predicts the two symmetric features at $\omega_2 = 0$ THz and $\omega_1 = \pm 3.9$ THz present in the experimental data. In contrast, feature d , and all features predicted for a M pathway, are either not present, or their absence is difficult to verify due to the modified IRF power predicted by the Ω_+ -THz IRF.

Symmetry analysis

Predicted coherence pathways contributing to features c and c^* must satisfy symmetry constraints imposed by the experimental electric field polarizations, the crystal orientation, and the phonon mode symmetry. With an X -cut crystal orientation, the THz and Raman fields are polarized along the Z and Y crystallographic axes. The Ω_+ phonon mode has E symmetry, and the $3m(C3_v)$ point group of LiNbO_3 removes the requirement of only considering even-ordered combinations of field polarization in the third-order response function $R^{(3)}$ [22]. As shown in Boyd, there are 73 non-zero $\chi^{(3)}$ tensor elements, 27 of which are unique. Tensor elements consistent with the $\{Z, Y\}$ polarizations of the experimental pump and probe fields are all non-zero. We assume that the LiNbO_3 optical axis (Z axis) is parallel to the probe polarization, and that the THz fields are polarized parallel to the crystallographic axes. Any slight ellipticity of the THz beams is ignored.

Next, we can analyze the symmetry constraints on pathways c and c^* . Both of these

C_{3v}	E	$2C_3(z)$	$3\sigma_v$	Linear	Quadratic
A_1	1	1	1	z	x^2+y^2, z^2
A_2	1	1	-1	R_z	
E	2	-1	0	$(x,y), (R_x, R_y)$	$(x^2-y^2, xy), (xz, yz)$

Table 9.1: C_{3v} character table

C_{3v}	A_1	A_2	E
A_1	A_1	A_2	E
A_2	A_2	A_1	E
E	E	E	A_1+A_2+E

Table 9.2: C_{3v} direct product table

features involve single quanta THz absorption processes which generate a coherent state. Beginning in the ground population state $|0\rangle \langle 0|$ (A_1 symmetry), a first THz field interaction at time $t=0$ can produce a fully symmetric product if it is polarized along Y :

$$\langle 1| M_Y |0\rangle \propto \langle E| E |A_1\rangle \subset A_1 \quad (9.2)$$

In this scenario, experimental constraints require the second THz interaction at time t_1 to be Z polarized, which does not result in a fully symmetric product.

$$\langle 0| M_Z |1\rangle \propto \langle A_1| A_1 |E\rangle \not\subset A_1 \quad (9.3)$$

Indeed, due to the orthogonal polarizations of the two THz fields, 2D-TTR pathways for c and c^* beginning in the ground population state are not symmetry allowed. Instead, we find that beginning in a thermally populated initial state $|1\rangle \langle 1|$ (E symmetry) does allow for a fully symmetric series of field interactions consistent with Π anharmonicity:

$$\begin{aligned}
\langle 2 | M_Y | 1 \rangle &\propto \langle A_1 + A_2 + E | E | E \rangle \subset A_1 \\
&\vdots \\
&t_1 \\
&\vdots \\
\langle 1 | M_Z | 2 \rangle &\propto \langle E | A_1 | A_1 + A_2 + E \rangle \subset A_1 \\
&\vdots \\
&t_2 \\
&\vdots \\
\langle 1 | \Pi_{YZ} | 1 \rangle &\propto \langle E | E | E \rangle \subset A_1
\end{aligned} \tag{9.4}$$

A similar analysis verifies that the oscillatory sum-frequency response along t_2 observed in 1D-TKE measurements is also fully symmetry allowed and linear in the Π operator:

$$\begin{aligned}
\langle 1 | \Pi_{YZ} | 0 \rangle &\propto \langle E | E | A_1 \rangle \subset A_1 \\
&\vdots \\
&t_2 \\
&\vdots \\
\langle 0 | \Pi_{YZ} | 1 \rangle &\propto \langle A_1 | E | E \rangle \subset A_1
\end{aligned} \tag{9.5}$$

In summary, it is reasonable to interpret the experimental LiNbO₃ 2D-TTR data in a $\chi^{(3)}$ framework. The phonon mode Ω_+ is strongly Raman and IR active with a large transition dipole element. All features observed in the 2D data are consistent with a polarizability anharmonicity. Lack of a sum-frequency convolution observed in halogenated methane 2D-TTR experiments is rationalized as a result of the different IRFs of the two experiments. Since the 1D-TKE data taken simultaneously are not governed by the same IRF as the 2D data, the oscillatory mode along t_2 is readily observed.

Interpretation #2: a cascaded $\chi^{(2)} \cdot \chi^{(2)}$ response

An alternative explanation for the LiNbO₃ 2D-TTR data is a cascaded $\chi^{(2)} \cdot \chi^{(2)}$ process, for which there is substantial precedent in the literature [23, 24, 25, 26]. A

cascading mechanism would involve excitation of a phonon mode via IR absorption, followed by optical rectification with the second THz field via a $\chi^{(2)}$ interaction. This interaction could generate a \sim DC polarization within the lithium niobate crystal which is then detected via the electro-optic effect by the Raman probe pulse. Crucially, a cascaded $\chi^{(2)} \cdot \chi^{(2)}$ process is indistinguishable in power scaling, and in many cases symmetry, to a $\chi^{(3)}$ response.

We will consider an optical rectification process involving one phonon field and one THz pump field. Adapting a standard frequency-domain description of optical rectification [27] with a representative dispersion model [11], the interaction between phonon and THz fields within the $z=50 \mu\text{m}$ thick LiNbO_3 crystal is given by:

$$\begin{aligned}
 E_{\text{O.R.}}(z, t_1, \omega_2) = & \frac{\sqrt{2}\pi\chi^{(2)}(\omega_2)}{n_{\text{THz}}^2 - n_{\Omega_+}^2} \tau \exp\left[\frac{-\omega_2^2 \tau^2}{4}\right] \\
 & \times \int_{-\infty}^{\infty} E_{\text{THz}}(t_2) E_{\Omega_+}(t_2 + t_1) \exp[-2\pi i \omega_2 t_2] dt_2 \\
 & \times \left[\frac{1}{2} \left(1 + \frac{n_{\Omega_+}}{n_{\text{THz}}} \right) \exp[i\omega_2 n_{\text{THz}} z / c] \right. \\
 & + \frac{1}{2} \left(1 - \frac{n_{\Omega_+}}{n_{\text{THz}}} \right) \exp[-i\omega_2 n_{\text{THz}} z / c] \\
 & \left. - \exp[i\omega_2 n_{\text{THz}} z / c] \right]
 \end{aligned} \tag{9.6}$$

There are several differences between Eq. 9.6 and the model given in [27]. First, the changing magnitude and phase of the input fields as a function of t_1 must be accounted for. A simple 2D-TTR IRF model can be constructed using an exponentially decaying phonon field and a THz field with a Gaussian envelope. A full $\{t_1, t_2\}$ IRF is then calculated which captures how the two input fields change in magnitude and phase during the 2D-TTR experiment. By the same logic, Eq. 9.6 uses the complex valued input spectrum $\int_{-\infty}^{\infty} E_{\text{THz}}(t_2) E_{\Omega_+}(t_2 + t_1) \exp[-2\pi i \omega_2 t_2] dt_2$ in the place of the pump intensity $|I_g|^2$.

A second alteration is the use of the complex-valued index n_{THz} in all of the exponential terms. This is in contrast to [27] where the input pump field was at 800 nm. The large difference between n_{THz} and $n_g^{800\text{nm}}$ allowed for the simplifying assumption that n_g is a constant real value. This assumption is not valid here, where the phonon and THz input fields are effectively equal in frequency and within an order of magnitude in spectral breadth.

Finally, as appears commonly done in the literature, the backward propagating field is ignored during calculation of Eq. 9.6. Dielectric parameters are used directly from [11], and $n_{THz}(\omega)$ is calculated as $\sqrt{\epsilon} = n + i\kappa$.

$$\epsilon(\omega) = \epsilon_{el} + \frac{\epsilon_{st}\omega_{TO}^2}{\omega_{TO}^2 - \omega^2 + 2i\gamma\omega} \quad (9.7)$$

Inputs to Eq. 9.6 were physically motivated: for example, the THz field had a 3.85 THz carrier frequency and FWHM lifetime of 250 fs. The input phonon field was modelled with a carrier frequency of 3.85 THz and a decay constant of 1.1 ps which was derived from fits to the data along t_1 . We fixed the spectral filter function variable τ equal to the phonon decay constant, reflecting the spectral windowing effect of the long-lived phonon field.

Using this model, we can reproduce the main features of the 2D signal observed in LiNbO₃. As shown in Fig. 9.8A, there are strong similarities with the experimental 2D-TTR data. Along t_2 , a broad slowly varying response reflects the \sim DC field produced through optical rectification of the phonon and THz electric fields. As the t_1 delay is varied, the relative phase of the two electric fields changes, resulting in the oscillatory response along t_1 . Similarly good agreement between the model (Fig. 9.8 B) and experimental spectra are clear. Fig. 9.9A compares the model and data at $t_1 = 0$ along t_2 ; good agreement is reached using the model input parameters. Similarly, we see a very close match in the sample response along t_1 (Fig. 9.9B).

Absence of a convolved sum-frequency response may be attributed to two different factors. First, and most important, the phonon-THz IRF naturally reduces spectral power at $\omega_2 = \Omega_+$. Another contributing factor may be the relative magnitudes of the $\chi^{(2)}$ and $\chi^{(3)}$ responses (with the caveat that the bright phonon state may further increase the efficiency of either a $\chi^{(2)}$ or $\chi^{(3)}$ process in non-trivial ways). Some rough numbers from a very thorough review [28] are helpful to begin estimating magnitudes of the competing processes. Table 9.3 compares three parameters for DAST, LiNbO₃, and GaP which are important for a cascaded $\chi^{(2)}$ process - the electro-optic coefficient r and two different measures of the optical rectification efficiency, d_{THz} and FM_{THz} . Two orders of magnitude separate the optical rectification efficiency figure of merit of GaP versus LiNbO₃ and DAST. Similarly, LiNbO₃ and DAST possess much larger electro-optic coefficients. While this comparison is highly inexact due to varying definitions of these material parameters and the differing phase-matching conditions under optical versus THz excitation, it suggests

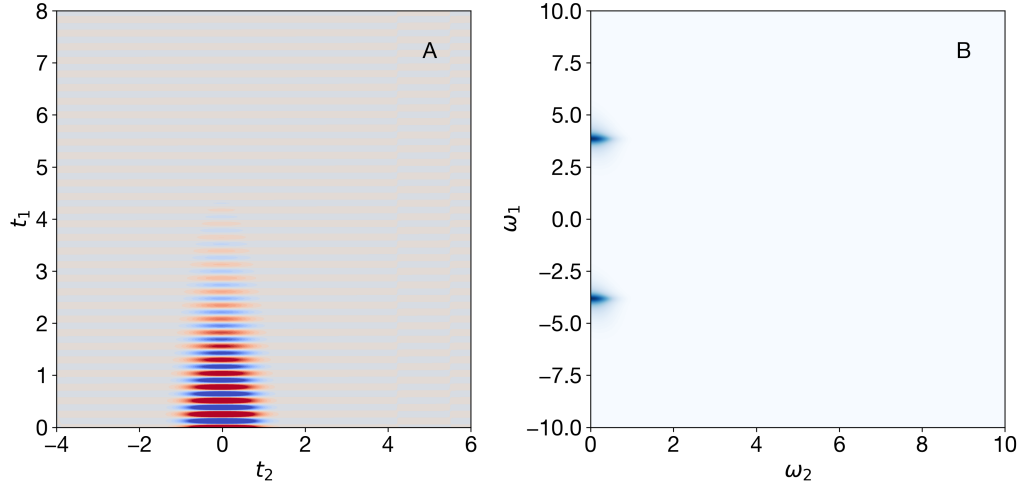


Figure 9.8: Optical rectification model of 2D-TTR LiNbO₃ response in the time (A) and frequency (B) domains. Good agreement is reached with experiment using physically motivated inputs to Eq. 9.6.

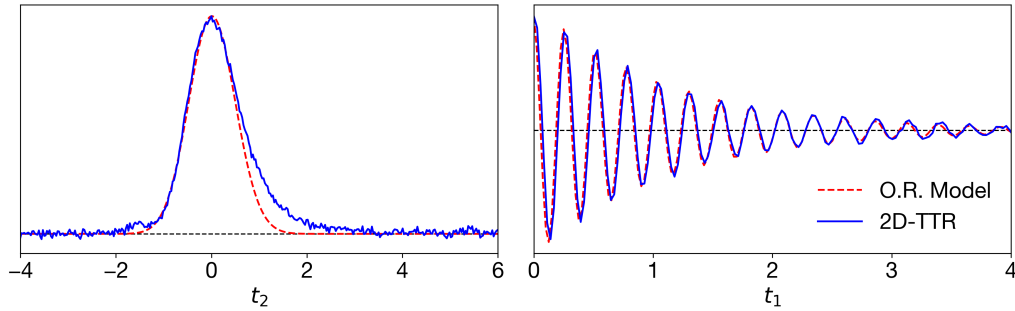


Figure 9.9: A) Comparison of the model and data response along t_2 at $t_1 = 0$. B) Comparison of the model and data response along t_1 at $t_2 = 0$.

cascaded $\chi^{(2)}$ processes may be several orders of magnitude stronger in LiNbO₃ than in GaP.

Polarization sensitive z-scan studies of potassium niobate have determined that the nonlinear refractive index from optical rectification can exceed the Kerr contribution by a factor of 2-4 depending upon the orientation of the pump electric field polarization to the crystal's c axis [25]. It is quite reasonable, therefore, to anticipate that cascaded signals in lithium niobate easily reach, and may exceed, a third-order response. The strongly t_1 -varying net pump polarization produced by the two orthogonal THz electric field components only exacerbates the mixing of the Kerr and optical rectification components.

Material	r (pm/V)	d_{THz} (pm/V)	FM_{THz} (pm/V) ²
DAST	47	240	5600
GaP	1	24	17
LiNbO ₃	30	160	1100

Table 9.3: Comparison of the electro-optic coefficient r , and THz generation parameters d_{THz} , the nonlinear optical coefficient and FM_{THz} , the figure of merit for DAST, LiNbO₃, and GaP [30].

An additional set of experiments could use the angular dependence of the optical rectification and Kerr contributions to selectively isolate each response [29]. For example, using parallel polarized pump and probe fields would measure the fully isotropic response function (e.g. $R_{ZZZZ}^{(3)}$), for which the optical rectification contribution is strictly zero [25]. We currently measure the anisotropic component $\propto R_{YZYZ}^{(3)}$ since this component 1) allows for easy THz-THz beam combining with the wire grid polarizer and 2) is detectable with the polarimetry style probe scheme used in the single-shot experiment. With careful experimental design, the two THz field could be combined instead using a D-mirror, and a carefully balanced dual photo-diode could measure the isotropic response.

Conclusions

A few final observations favor the cascaded χ^2 interpretation of these data. Looking back at the 1D-TKE measurements shown in Fig. 9.3 B provides a final test of the two interpretations. Data collected in 1D-TKE will contain both sum-frequency signals and the projection of the 2D-TTR data along ω_2 . Two prominent features at $\omega_2 \approx 0$ and $\omega_2 = \Omega_+$ are observed. No $2\Omega_+$ feature is observed in the data, despite these data presumably not being impacted by the more restrictive 2D IRF. Terahertz bandwidth is not a limitation for observing the $2\Omega_+$ mode, and the experimental Raman bandwidth has observed a very slightly lower frequency vibrational mode in chloroform at $\omega_2=7.8$ THz. Therefore, it is counter-intuitive that we do not observe a $2\Omega_+$ feature if a Π anharmonicity is truly present in the sample. In contrast, optical rectification is consistent with the $\omega_2 \approx 0$ THz feature in the 1D-TKE spectra, and there is every reason to expect that a cascaded process may reach, if not exceed, the magnitude of any third-order signal.

BIBLIOGRAPHY

1. M. A. Sentef, Light-enhanced electron-phonon coupling from nonlinear electron-phonon coupling. en, *Phys. Rev. B* **95**, 205111, DOI 10.1103/PhysRevB.95.205111 (May 2017).
2. I. Gierz, A. Cavalleri, Electronic-structural dynamics in graphene. en, *Struct. Dyn.* **3**, 051301, DOI 10.1063/1.4964777 (Sept. 2016).
3. V. Esposito *et al.*, Nonlinear Electron-Phonon Coupling in Doped Manganites. en, *Phys. Rev. Lett.* **118**, 247601, DOI 10.1103/PhysRevLett.118.247601 (June 2017).
4. C. L. Johnson, B. E. Knighton, J. A. Johnson, Distinguishing Nonlinear Terahertz Excitation Pathways with Two-Dimensional Spectroscopy. en, *Phys. Rev. Lett.* **122**, 073901, DOI 10.1103/PhysRevLett.122.073901 (Feb. 2019).
5. S. Maehrlein, A. Paarmann, M. Wolf, T. Kampfrath, Terahertz Sum-Frequency Excitation of a Raman-Active Phonon. en, *Phys. Rev. Lett.* **119**, 127402, DOI 10.1103/PhysRevLett.119.127402 (Sept. 2017).
6. I. A. Finneran, R. Welsch, M. A. Allodi, T. F. Miller, G. A. Blake, 2D THz-THz-Raman Photon-Echo Spectroscopy of Molecular Vibrations in Liquid Bromoform. *Journal of Physical Chemistry Letters* **8**, 4640–4644 (2017).
7. R. Trebino *et al.*, Measuring ultrashort laser pulses in the time-frequency domain using frequency-resolved optical gating. en, *Review of Scientific Instruments* **68**, 3277–3295, DOI 10.1063/1.1148286 (Sept. 1997).
8. R. Trebino, D. J. Kane, Using phase retrieval to measure the intensity and phase of ultrashort pulses: frequency-resolved optical gating. en, *J. Opt. Soc. Am. A* **10**, 1101, DOI 10.1364/JOSAA.10.001101 (May 1993).
9. I. Wilke, S. Sengupta, en, in *Terahertz spectroscopy: principles and applications*, p. 32.
10. M. Cornet, J. Degert, E. Abraham, E. Freysz, Terahertz Kerr effect in gallium phosphide crystal. en, *J. Opt. Soc. Am. B* **31**, 1648, DOI 10.1364/JOSAB.31.001648 (July 2014).
11. A. S. Barker, R. Loudon, Dielectric Properties and Optical Phonons in LiNbO₃. en, *Phys. Rev.* **158**, 433–445, DOI 10.1103/PhysRev.158.433 (June 1967).
12. W. D. Johnston, Nonlinear Optical Coefficients and the Raman Scattering Efficiency of LO and TO Phonons in Acentric Insulating Crystals. en, *Phys. Rev. B* **1**, 3494–3503, DOI 10.1103/PhysRevB.1.3494 (Apr. 1970).

13. S. Sanna *et al.*, Raman scattering efficiency in LiTaO₃ and LiNbO₃ crystals. en, *Phys. Rev. B* **91**, 224302, DOI 10.1103/PhysRevB.91.224302 (June 2015).
14. C. A. Gautier, M. Mérian, J. Etchepare, Low frequency E-symmetry phonon modes in LiTaO₃ : a non-linear temporal domain approach. en, *J. Phys.: Condens. Matter* **12**, 7175–7182, DOI 10.1088/0953-8984/12/32/302 (Aug. 2000).
15. D. Kien, J. Loulergue, J. Etchepare, Nonlinear response to polariton waves driven in perovskites by femtosecond pulses. en, *Optics Communications* **101**, 53–59, DOI 10.1016/0030-4018(93)90322-V (Aug. 1993).
16. P. J. Delfyett, R. Dorsinville, R. R. Alfano, Spectral and temporal measurements of the third-order nonlinear susceptibility of LiNbO₃ using picosecond Raman-induced phase-conjugation spectroscopy. en, *Phys. Rev. B* **40**, 1885–1891, DOI 10.1103/PhysRevB.40.1885 (July 1989).
17. D. M. Juraschek, S. F. Maehrlein, Sum-frequency ionic Raman scattering. en, *Phys. Rev. B* **97**, 174302, DOI 10.1103/PhysRevB.97.174302 (May 2018).
18. B. S. Dastrup, J. R. Hall, J. A. Johnson, Experimental determination of the interatomic potential in LiNbO₃ via ultrafast lattice control. en, *Appl. Phys. Lett.* **110**, 162901, DOI 10.1063/1.4980112 (Apr. 2017).
19. Y. Ikegaya, H. Sakaibara, Y. Minami, I. Katayama, J. Takeda, Real-time observation of phonon-polariton dynamics in ferroelectric LiNbO₃ in time-frequency space. en, *Appl. Phys. Lett.* **107**, 062901, DOI 10.1063/1.4928480 (Aug. 2015).
20. G. J. Mead, H.-W. Lin, I.-B. Magdau, T. F. Miller, G. A. Blake, Sum-Frequency Signals in 2D-Terahertz-Terahertz-Raman Spectroscopy. en, *J. Phys. Chem. B*, acs.jpcc.0c07935, DOI 10.1021/acs.jpcc.0c07935 (Sept. 2020),
21. D. Sidler, P. Hamm, Feynman diagram description of 2D-Raman-THz spectroscopy applied to water. en, *J. Chem. Phys.* **150**, 044202, DOI 10.1063/1.5079497 (Jan. 2019).
22. R. W. Boyd, *Nonlinear optics* (Academic Press, Amsterdam ; Boston, 3rd ed, 2008).
23. C. Bosshard, I. Biaggio, S. Fischer, S. Follonier, P. Günter, Cascaded contributions to degenerate four-wave mixing in an acentric organic crystal. en, *Opt. Lett.* **24**, 196, DOI 10.1364/OL.24.000196 (Feb. 1999).
24. M. Zgonik, P. Günter, Cascading nonlinearities in optical four-wave mixing. en, *J. Opt. Soc. Am. B* **13**, 570, DOI 10.1364/JOSAB.13.000570 (Mar. 1996).
25. C. Bosshard, R. Spreiter, M. Zgonik, P. Günter, Kerr Nonlinearity via Cascaded Optical Rectification and the Linear Electro-optic Effect. en, *Phys. Rev. Lett.* **74**, 2816–2819, DOI 10.1103/PhysRevLett.74.2816 (Apr. 1995).

26. C. Bosshard, U. Gubler, P. Kaatz, W. Mazerant, U. Meier, Non-phase-matched optical third-harmonic generation in noncentrosymmetric media: Cascaded second-order contributions for the calibration of third-order nonlinearities. en, *Phys. Rev. B* **61**, 10688–10701, DOI 10.1103/PhysRevB.61.10688 (Apr. 2000).
27. J. Faure, J. Van Tilborg, R. A. Kaindl, W. P. Leemans, Modelling Laser-Based Table-Top THz Sources: Optical Rectification, Propagation and Electro-Optic Sampling. en, *Optical and Quantum Electronics* **36**, 681–697, DOI 10.1023/B:OQEL.0000039617.85129.c2 (June 2004).
28. M. Jazbinsek, U. Puc, A. Abina, A. Zidansek, Organic Crystals for THz Photonics. en, *Applied Sciences* **9**, 882, DOI 10.3390/app9050882 (Mar. 2019).
29. J.-P. Caumes, L. Videau, C. Rouyer, E. Freysz, Kerr-Like Nonlinearity Induced via Terahertz Generation and the Electro-Optical Effect in Zinc Blende Crystals. en, *Phys. Rev. Lett.* **89**, 047401, DOI 10.1103/PhysRevLett.89.047401 (July 2002).
30. M. Jazbinsek, U. Puc, A. Abina, A. Zidansek, Organic Crystals for THz Photonics. en, *Applied Sciences* **9**, 882, DOI 10.3390/app9050882 (Mar. 2019).

Part IV

Conclusion and Future Directions

CONCLUSIONS AND FUTURE DIRECTIONS

Conclusions distributed throughout this thesis point toward a range of future directions in both rotational microwave and vibrational terahertz spectroscopies. Some, such as combining the high spectral resolution of chirped pulse-Fourier transform microwave spectroscopy with linear THz absorption measurements of alcohol-water dimers, have been elaborated upon in previous group theses. The lab, thanks to the excellent work of Alex Froebel and Sadie Dutton, is fast approaching the point of performing these hybrid experiments. In addition to these exciting developments, pursuit of further single-shot system optimization and application development will benefit from Haw-Wei Lin and Kyle Virgil's deep knowledge of the system and of novel photovoltaic materials. The remainder of this final chapter will review a series of intriguing possibilities.

10.1 2D-TTR spectroscopy of water and aqueous solutions

We have recently observed the terahertz Kerr effect response in neat water (Fig. 10.1), as well as a mixture of aqueous solutions. These measurements are extremely challenging for a number of reasons. First, despite having an intense linear free induction decay, water has an anomalously weak Kerr response. Prolonged averaging is required to observe water's 1D-TKE signal. Second, water relaxes quickly back to equilibrium, which means that the entirety of the chemical physics is contained within several hundred femtoseconds. Accurately characterizing the 1D-TKE instrument response function, and identifying sources of temporal jitter and drift, are critical for extracting true molecular signals from water's brief signal.

A single-shot approach is useful for measuring water's Kerr response for a number of reasons. Overlap of the pump and probe focal regions is possible using the focal imaging technique described earlier in the thesis. The large t_2 window captured with each shot aids in detecting glimmers of signal which otherwise may have been lost when optimizing the signal intensity while sitting at a single point on a stage scan. The lack of moving parts further helps reduce signal drift. Finally, the level of scattered photons contributing to the noise floor is very easily gauged and optimized using the single-shot approach.

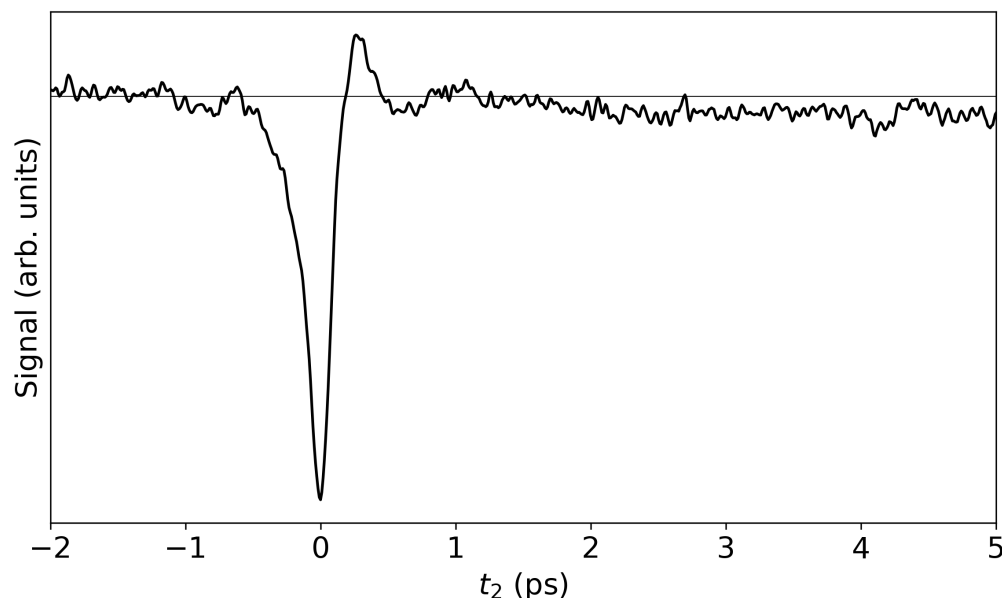


Figure 10.1: The 1D-TKE response of neat water. A bi-polar response with a large negative-going component is characteristic of water and aqueous solutions.

Drawbacks to the technique mainly center upon the currently large probe focal ellipse and the amount of glass in the probe optical path. The elliptical probe focus is, to some extent, intrinsic to the echelon. Reducing this focal point as much as possible would increase the Raman probe field strength and thus amplify the third-order signal. While a smaller t_2 time window naturally reduces the focal region, current optical design results in unacceptable levels of windowing and vignetting in the data. Since the current diagnosis of these effects implicates the non-linear aperture within the sample, it is possible that optimizing the probe imaging pathway may reduce these distortions. A second route for optimizing the probe pathway is by removing as much glass as possible. This reduces dispersion in the probe pulse which leads to an artificially broad convolved 1D-TKE water signal.

One route for performing higher precision, higher signal-to-noise measurements of water would be to synthesize benefits of the single-shot and stage scan techniques. For example, the probe pulse used in stage scan measurements passes through a minimal number of optical elements and easily reaches diffraction limited spot sizes, maximizing the available Raman probe power. At the same time, the overlap between the THz pump and Raman probe may still be optimized using the single-shot camera for beam imaging, as well as fully optimizing the power and circularity

of the THz pump beam.

Evolving the experiment further to perform 2D measurements will require commensurate improvements in all the above areas, and extra care to characterize the instrument response function. A less featured THz input field will be invaluable here. THz generation using a two-color plasma has recently been demonstrated in our lab by Kyle Virgil, and may find useful application for water if field strengths are increased high enough.

10.2 Time-resolved dynamics in hybrid perovskites

Research has demonstrated the utility of single shot approaches to study a number of irreversible physical and chemical processes [1, 2, 3, 4, 5, 6]. A currently under-explored application of linear THz time-domain spectroscopy in our lab is measuring changes in material properties during destructive processes. For example, hybrid organo-lead halide perovskites are exceptional photovoltaic compounds which remain quite fragile to lattice degradation via interactions with moisture in the ambient atmosphere. Observing degradation in a time-resolved manner, both to understand fundamental characteristics of the process and to test approaches to mitigating the undesired structural destruction, could easily be achieved with the single-shot spectrometer.

In these experiments, a perovskite sample with adequate environmental controls (temperature, humidity, irradiation) could be placed at the focal plane of a THz source. Absorption of THz photons by the sample may then be observed by focusing the transmitted THz light onto an electro-optic crystal and measuring the time-domain field with the single-shot spectrometer. The advantage this has over the stage-scan approach is that data may be acquired at close to the repetition rate of the laser (e.g. 100s of Hz). Observing degradation on the millisecond timescale would very thoroughly characterize degradation processes, which typically occur on the order of seconds to hours.

Another electro-optic based series of measurements that may be performed on materials would be a hybrid THz pump, THz probe experiment. At the first THz focus, an THz pulse perturbs the phonon modes within the sample. Phonon-mediated modulation of the material's complex refractive index could then be observed by measuring a modulation of the THz probe absorption using differential chopping. Again, this experiment could be performed quickly using the single-shot apparatus.

10.3 Single-shot applications to coherent control experiments

Coherent control describes the process of using electromagnetic radiation to precisely control a molecular degree of freedom. There have been a variety of demonstrations of coherent control in molecular systems [7, 8, 9, 10, 11]. A general challenge is determining the optimal pulse frequencies and phases that will most efficiently drive the dynamic of interest. One approach to addressing this question is to first map out the N dimensional potential energy surface along which the initial state may proceed to the final desired state, and then calculate the optimal spectral chirp and phase to connect the two states. As one can imagine, this would be a computationally expensive approach.

An alternative experimental approach borrows from the fields of optimal control and evolutionary algorithms. Using an arbitrarily shaped initial pump pulse, the degree to which the system responds in the desired manner is observed. Small iterative modifications to the pulse are then made in order to optimize the desired outcome. This genetic algorithm approach has been demonstrated in many systems [12].

Terahertz photons may provide an advantage over optical fields for performing coherent control of low-frequency torsional modes, since the system would remain in the electronic ground state as it transitions along the driven pathway coordinate. Control over the THz pump can be achieved rather simply by using a near IR (NIR) pulse shaper to tailor the NIR pulses which are optically rectified during THz generation. Single-shot electro-optic sampling of THz-induced changes in the linear absorption spectrum of a sample could provide fast feedback into a coherent control genetic algorithm that optimizes the THz pump waveform.

BIBLIOGRAPHY

1. Y.-H. Cheng, S. W. Teitelbaum, F. Y. Gao, K. A. Nelson, Femtosecond laser amorphization of tellurium. en, *Phys. Rev. B* **98**, 134112, DOI 10.1103/PhysRevB.98.134112 (Oct. 2018).
2. S. W. Teitelbaum *et al.*, Real-Time Observation of a Coherent Lattice Transformation into a High-Symmetry Phase. en, *Phys. Rev. X* **8**, 031081, DOI 10.1103/PhysRevX.8.031081 (Sept. 2018).
3. I. Katayama *et al.*, Ferroelectric Soft Mode in a SrTiO₃ Thin Film Impulsively Driven to the Anharmonic Regime Using Intense Picosecond Terahertz Pulses. en, *Phys. Rev. Lett.* **108**, 097401, DOI 10.1103/PhysRevLett.108.097401 (Feb. 2012).
4. Y. Minami, H. Yamaki, I. Katayama, J. Takeda, Broadband pump–probe imaging spectroscopy applicable to ultrafast single-shot events. en, *Appl. Phys. Express* **7**, 022402, DOI 10.7567/APEX.7.022402 (Feb. 2014).
5. J. Takeda, W. Oba, Y. Minami, T. Saiki, I. Katayama, Ultrafast crystalline-to-amorphous phase transition in Ge₂Sb₂Te₅ chalcogenide alloy thin film using single-shot imaging spectroscopy. en, *Appl. Phys. Lett.* **104**, 261903, DOI 10.1063/1.4886969 (June 2014).
6. G. T. Noe *et al.*, Single-shot terahertz time-domain spectroscopy in pulsed high magnetic fields. *Optics Express* **24**, 30328, DOI 10.1364/oe.24.030328 (2016).
7. T. Laarmann *et al.*, Coherent control of bond breaking in amino acid complexes with tailored femtosecond pulses. en, *The Journal of Chemical Physics* **127**, 201101, DOI 10.1063/1.2806029 (Nov. 2007).
8. B. J. Pearson, J. L. White, T. C. Weinacht, P. H. Bucksbaum, Coherent control using adaptive learning algorithms. en, *Phys. Rev. A* **63**, 063412, DOI 10.1103/PhysRevA.63.063412 (May 2001).
9. W. Salzmann *et al.*, Coherent control with shaped femtosecond laser pulses applied to ultracold molecules. en, *Phys. Rev. A* **73**, 023414, DOI 10.1103/PhysRevA.73.023414 (Feb. 2006).
10. M. Y. Shverdin, S. N. Goda, G. Y. Yin, S. E. Harris, Coherent control of laser-induced breakdown. en, *Opt. Lett.* **31**, 1331, DOI 10.1364/OL.31.001331 (May 2006).
11. T. C. Weinacht, P. H. Bucksbaum, Using feedback for coherent control of quantum systems. *J. Opt. B: Quantum Semiclass. Opt.* **4**, R35–R52, DOI 10.1088/1464-4266/4/3/201 (June 2002).

12. D. Zeidler, S. Frey, K.-L. Kompa, M. Motzkus, Evolutionary algorithms and their application to optimal control studies. en, *Phys. Rev. A* **64**, 023420, DOI 10.1103/PhysRevA.64.023420 (July 2001).

*Appendix A*PYTHON DATA PROCESSING SCRIPT FOR 1D KERR EFFECT
DATA

This simple script can process .dat formatted data collected using the Andor Solis program for a single-shot experiment with a 500 Hz THz pump modulation frequency.

```

### bin_reader.py
import numpy as np
import matplotlib.pyplot as plt
import time

file = 'DIM_10K_.dat' # file name
w = 1280 # array width in pixels, 2x bin
h = 10 # array height in pixels, 8x bin
num = 10000 # number of images acquired

# init. arrays for even and odd image data
odd = np.zeros(w)
even = np.zeros(w)

# start timer
t0 = time.time()

# read in file with appropriate encoding
b = np.fromfile(file, dtype = np.int32)

t1 = time.time()
c = np.reshape(b, (num, h, w))

# sum along the array height
d = np.sum(c, axis=1)

```

```

# coadd images
for i in range(num):
    if i % 2 == 0:
        even += d[i,:]
    else:
        odd += d[i,:]

# perform subtraction, normalization
if np.max(even) > np.max(odd):
    diff = (even-odd)/odd
else:
    diff = (odd-even)/even

t2 = time.time()
print 'Read:', np.round(t1-t0, 3)
print 'Process:', np.round(t2-t1, 3)

# save processed data to txt file
np.savetxt('%s_diff.txt' % file, diff)

# plot results
plt.subplot(2,1,1)
plt.plot(even, label='Even')
plt.plot(odd, label='Odd')
plt.xlabel('Pixels (2x bin)')
plt.ylabel('# photons (counts)')
plt.legend(frameon=False)
plt.subplot(2,1,2)
plt.semilogy(diff, label='Diff')
plt.xlabel('Pixels (2x bin)')
plt.ylabel('Signal (a.u.)')
plt.legend(frameon=False)
plt.show()
plt.close()

```

Appendix B

2D-TTR BROMOFORM DATA UNDER TWO OPA CONDITIONS

We provide an additional example of the sensitivity of bromoform's 2D-TTR spectrum to the instrument response function, which was first noticed as a result of changing the infrared wavelengths that pump the two THz emitters. Initial 2D-TTR experiments used the two orthogonally polarized signal ($1.4\ \mu\text{m}$) and idler ($1.8\ \mu\text{m}$) outputs of the TOPAS-C OPA were each used to pump one of the DAST crystals. However, we observed that the majority of the idler line's IR power was concentrated in a small $\sim 1\ \text{mm}$ diameter point within the larger $8\ \text{mm}$ diameter beam. As a result, this concentrated point of power was burning the DAST crystal face. To prevent damage to the emitter crystal, we split the signal beam into two halves, rotated one half's polarization to match the idler polarization, and recorded new 2D-TTR data of bromoform. Dramatic differences in bromoform's time (Fig. B.1) and frequency (Fig. B.2) domain response were observed, drawing our attention to the importance of the IRF in 2D-TTR. SF-RDM analysis of the original $1.4/1.8\ \mu\text{m}$ bromoform data yielded similarly excellent agreement between experiment and simulation.

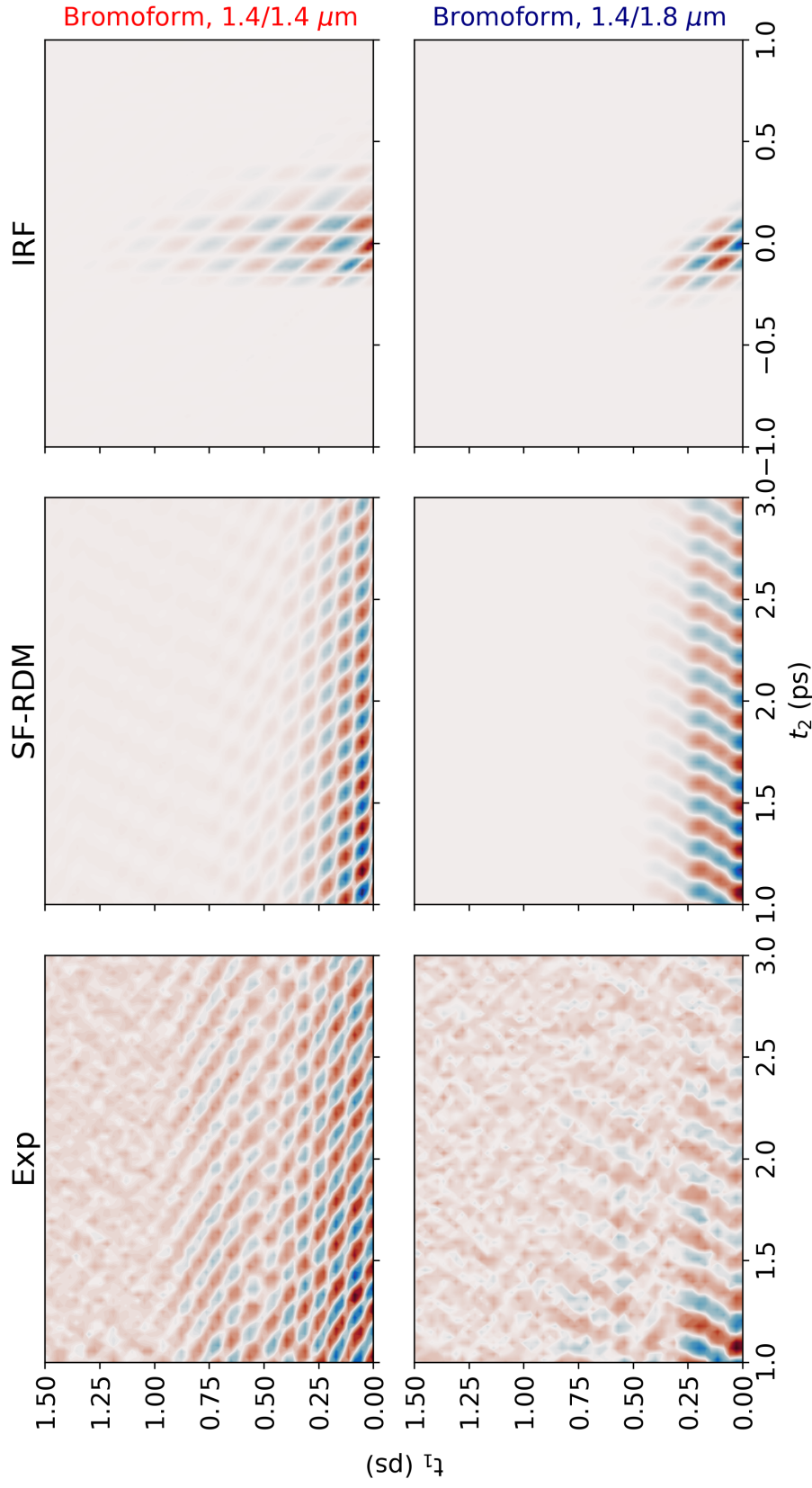


Figure B.1: Top and bottom rows compare the experimental (Exp) bromoform time-domain data under two different THz pumping regimes. Slight changes to the emitted THz fields result in different time-domain IRFs. SF-RDM models using the THz electric fields that produce each IRF fully reproduce the experimental data.

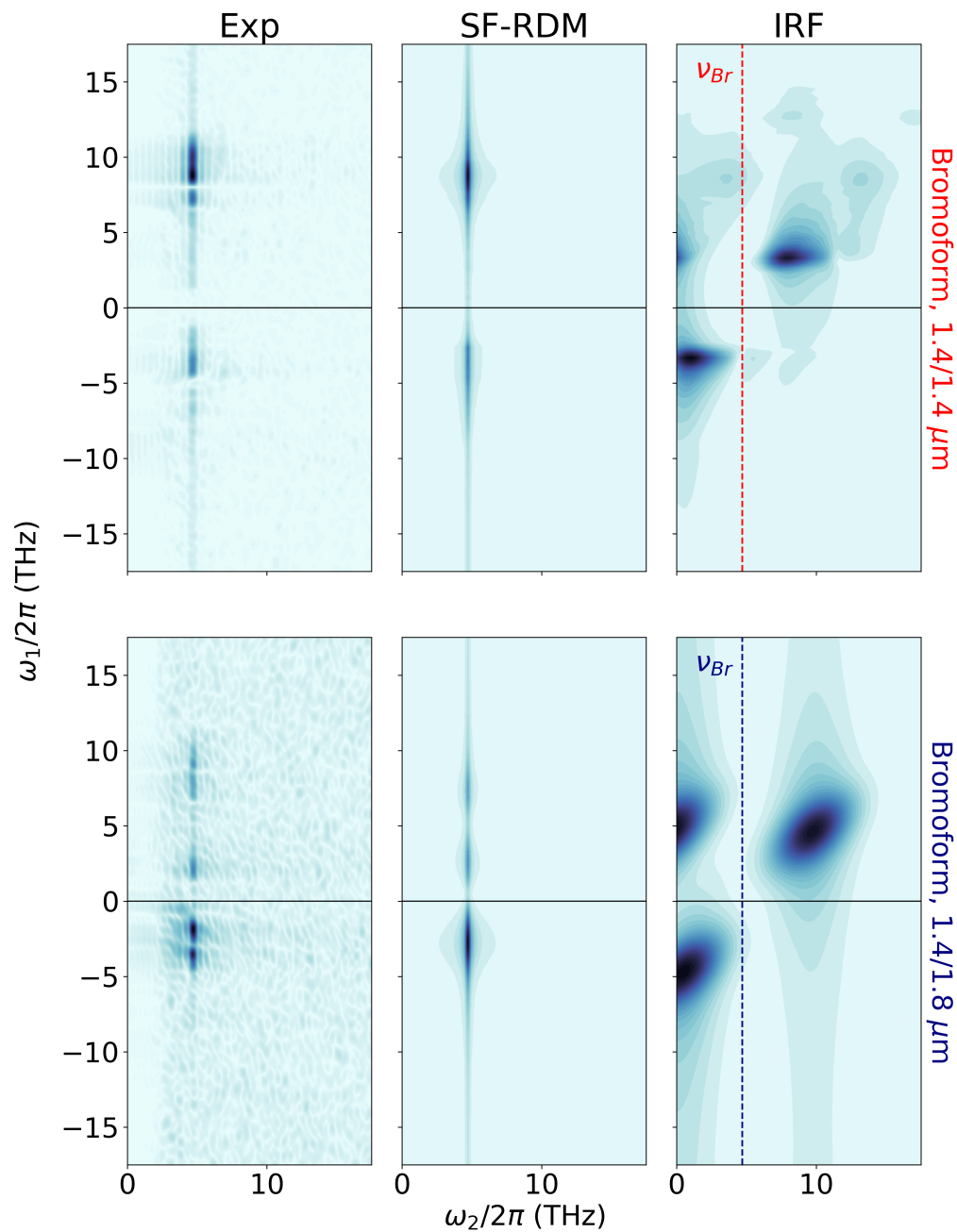


Figure B.2: Top and bottom rows compare the experimental (Exp) bromoform frequency-domain data under two different THz pumping regimes. Slight changes to the emitted THz fields result in different frequency-domain IRFs. SF-RDM models with the THz electric fields that produce each IRF reproduce the experimental spectra.